SIMULATION OF HYDRAULIC FRACTURES AND THEIR INTERACTIONS WITH NATURAL FRACTURES

A Thesis

by

VARAHANARESH KUMAR SESETTY

Submitted to the Office of Graduate Studies of
Texas A&M University
in partial fulfillment of the requirements for the degree of

MASTER OF SCIENCE

August 2012

Major Subject: Petroleum Engineering

Simulation of Hydraulic Fractures and Their Interactions with Natural Fractures

Copyright 2012 Varahanaresh Kumar Sesetty

SIMULATION OF HYDRAULIC FRACTURES AND THEIR INTERACTIONS WITH NATURAL FRACTURES

A Thesis

by

VARAHANARESH KUMAR SESETTY

Submitted to the Office of Graduate Studies of
Texas A&M University
in partial fulfillment of the requirements for the degree of

MASTER OF SCIENCE

Approved by:

Chair of Committee,	Ahmad Ghassemi
Committee Members,	Peter Valko
	Vikram Kinra
Head of Department,	A. D. Hill

August 2012

Major Subject: Petroleum Engineering

ABSTRACT

Simulation of Hydraulic Fractures and Their Interactions with Natural Fractures.

(August 2012)

Varahanaresh Kumar Sesetty, B.Tech., Jawaharlal Nehru Technological University;

Chair of Advisory Committee: Dr. Ahmad Ghassemi

Modeling the stimulated reservoir volume during hydraulic fracturing is important to geothermal and petroleum reservoir stimulation. The interaction between a hydraulic fracture and pre-existing natural fractures exerts significant control on stimulated volume and fracture network complexity. This thesis presents a boundary element and finite difference based method for modeling this interaction during hydraulic fracturing process. In addition, an improved boundary element model is developed to more accurately calculate the total stimulated reservoir volume.

The improved boundary element model incorporates a patch to calculate the tangential stresses on fracture walls accurately, and includes a special crack tip element at the fracture end to capture the correct stress singularity the tips The fracture propagation model couples fluid flow to fracture deformation, and accounts for fracture propagation including the transition of a mechanically-closed natural fractures to a hydraulic fracture.

The numerical model is used to analyze a number of stimulation scenarios and to study the resulting hydraulic fracture trajectory, fracture aperture, and pressures as a function of injection time. The injection pressure, fracture aperture profiles shows the complexity of the propagation process and its impact on stimulation design and proppant placement. The injection pressure is observed to decrease initially as hydraulic fracture propagates and then it either increases or decreases depending on the factors such as distance between hydraulic fracture and natural fracture, viscosity of the injected fluid, injection rates.

Also, the influence of flaws on natural fracture in its opening is modeled. Results shows flaws that are very small in length will not propagate but are influencing the opening of natural fracture. If the flaw is located near to one end tip the other end tip will likely propagate first and vice versa. This behavior is observed due to the stress shadowing effect of flaw on the natural fracture.

In addition, sequential and simultaneous injection and propagation of multiple fractures is modeled. Results show that for sequential injection, the pressure needed to initiate the later fractures increases but the geometry of the fractures is less complicated than that obtained from simultaneous injection under the same fracture spacing and injection. It is also observed that when mechanical interaction is present, the fractures in sequential fracturing have a higher width reduction as the later fractures are formed.

DEDICATION

To my parents

ACKNOWLEDGEMENTS

First I would like to thank my committee chair Dr. Ahmad Ghassemi for his immense support and trust in me for completion of this work. The valuable lessons I learned from him made my work much simpler and effective. His guidance is deeply appreciated.

I would like to extend my thanks to my committee members Dr. Peter Valko and Vikram Kinra for helping me to finish this work in all the ways they could.

I would also like to thank my fellow Aggie members for their gratitude and friendly nature, especially Mohammadreza for helping me whenever I am in need. Thanks also to the department faculty and computer support staff for their immediate attention to my needs.

Finally, thanks to my mother and father for their love and support.

TABLE OF CONTENTS

Page

LIST OF FIGURES

FIGURE Page

FIGURE Page

FIGURE Page

FIGURE Page

LIST OF TABLES

TABLE Page

1. INTRODUCTION

1.1 Calculation of Stimulated Volume Using the Displacement Discontinuity Method

Hydraulic fracturing by water injection is extensively used to stimulate unconventional gas reservoirs. The water is pumped at a high pressure into a selected section of the wellbore to create and extend a fracture(s) into the formation. The applied pressure in the fracture(s) re-distributes the pore pressure and stresses around the main fracture causing rock deformation and failure by fracture initiation, and/or activation of discontinuities such as joints and bedding planes. The net result is often enhancement of the formation permeability. The rock failure process is often accompanied by micro-seismicity that can provide useful information regarding the stimulated volume. The formation response to injection has been the subject of many studies; however, the literature pertaining to the subject of rock failure around a hydraulic fracture is not extensive. Warpinski and Wolhart 2004 presented a semi-analytical method to calculate the stress and pore pressure variations induced by a hydraulic fracture, and evaluated the likelihood and potential causes of micro-seismic activity in the vicinity of a major fracture. The semi-analytical method was based on simple crack geometry and approximation of the pore pressure in the reservoir without flow considerations in the fracture. Palmer et al. adopted a 2D model to study the impact of stimulation of Barnett shale permeability enhancement. Ge and Ghassemi 2007 also used a 2D approach and studied the impact of

---

This thesis follows the style of *SPE Journal*.

the in-situ stress, pore pressure, as well as poroelastic and thermoelastic phenomena on the rock failure around a hydraulic fracture. The resulting stresses were also used to calculate the stimulated volume and the permeability enhancement. In this work, we present numerical models for analysis of stress distribution around fractures and also simulate hydraulic fracture propagation near natural fractures. The models are applied to study the potential for rock failure in the vicinity of hydraulic fractures and to model HF coalescence with natural fracture. The modeling work consists of 2D displacement discontinuity method.

2. DISPLACEMENT DISCONTINUITY METHOD

2.1 2D Displacement Discontinuity Method for Fracture Modeling

Displacement discontinuity method is a boundary element method which is based on the analytical solution to the problem of a constant discontinuity in displacement over a finite line segment in x-y plane of an infinity elastic solid. A line crack can be imagined as two opposite surfaces that have been displaced relative to one another. In the present case the crack surfaces are assumed to have been displaced by a constant amount along the elements that are used to simulate crack (i.e., DD element). Then the crack is divided in to a series of N elements. Knowing the analytical solution for a single constant element displacement discontinuity, the numerical solution to the problem for a crack system is found by summing the effects of all the N elements on all fracture segments present in the network.

2.2 Formulation and Implementation of the DD Method

Consider a fracture parallel to the x-axis (Fig 1). The two surfaces of the crack can be distinguished as $y=0^+$ (positive surface), $y=0^-$ (negative surface). The displacement discontinuity D_i is defined as the difference in displacements between the two sides of the segment as follows (Crouch and Starfield, 1983):

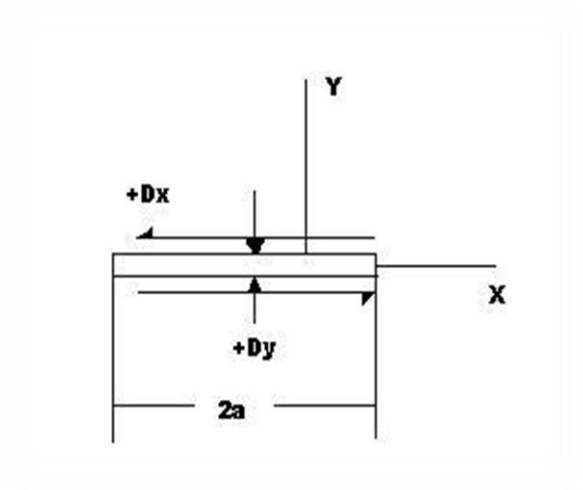

Fig 1. Constant displacement discontinuity components D_x and D_y

$$\begin{aligned} D_x &= u_x(x,0-) - u_x(x,0+) \\ D_y &= u_y(x,0-) - u_y(x,0+) \end{aligned} \tag{1}$$

where u_x and u_y are the positive in the positive *x*- and *y*-coordinate direction and the normal component of displacement discontinuity D_y is positive if the two surfaces of the crack displace toward one another. The shear component D_x is positive if the positive surface of the crack moves to the left with respect to the negative surface. The solution for the displacement and stress components caused by unit DD on an element of length 2a are given by (Crouch and Starfield, 1983):

$$\begin{aligned} u_x &= D_x\left[2(1-\nu) f_{,y} - y f_{,xx}\right] + D_y\left[-(1-2\nu) f_{,x} - y f_{,xy}\right] \\ u_y &= D_x\left[2(1-\nu) f_{,x} - y f_{,xy}\right] + D_y\left[-(1-2\nu) f_{,y} - y f_{,yy}\right] \end{aligned} \tag{2}$$

$$\begin{aligned}
\sigma_{xx} &= 2GD_x\left[+2f_{,xy}+yf_{,xyy}\right]+2GD_y\left[f_{,yy}+yf_{,yyy}\right]\\
\sigma_{yy} &= 2GD_x\left[-yf_{,xyy}\right]+2GD_y\left[f_{,yy}-yf_{,yyy}\right]\\
\sigma_{xy} &= 2GD_x\left[f_{,yy}+yf_{,yyy}\right]+2GD_y\left[-yf_{,yyy}\right]
\end{aligned} \tag{3}$$

The function f (x, y) in above equations is given as f (x, y)

$$f(x,y)=\frac{-1}{4\pi(1-\nu)}\left|\begin{array}{l} y(\arctan\frac{y}{x-a}-\arctan\frac{y}{x+a})-(x-a)\ln\sqrt{\left[(x-a)^2+y^2\right]}+\\ (x+a)\ln\sqrt{\left[(x+a)^2+y^2\right]}\end{array}\right| \tag{4}$$

The derivatives of the above function are:

$$\begin{aligned}
f_{,x} &= \frac{1}{4\pi(1-\nu)}\left[\ln\sqrt{\left[(x-a)^2+y^2\right]}-\ln\sqrt{\left[(x+a)^2+y^2\right]}\right]\\
f_{,y} &= \frac{-1}{4\pi(1-\nu)}\left[\arctan\frac{y}{x-a}-\arctan\frac{y}{x+a}\right]\\
f_{,xy} &= \frac{1}{4\pi(1-\nu)}\left[\frac{y}{(x-a)^2+y^2}-\frac{y}{(x+a)^2+y^2}\right]\\
f_{,xx} &= -f_{,yy}=\frac{1}{4\pi(1-\nu)}\left[\frac{x-a}{(x-a)^2+y^2}-\frac{x+a}{(x+a)^2+y^2}\right]\\
f_{,xyy} &= -f_{,xxx}=\frac{1}{4\pi(1-\nu)}\left[\frac{(x-a)^2-y^2}{\{(x-a)^2+y^2\}^2}-\frac{(x+a)^2-y^2}{\{(x+a)^2+y^2\}^2}\right]\\
f_{,yyy} &= -f_{,xxy}=\frac{2y}{4\pi(1-\nu)}\left[\frac{(x-a)}{\{(x-a)^2+y^2\}^2}-\frac{(x+a)}{\{(x+a)^2+y^2\}^2}\right]
\end{aligned} \tag{5}$$

In this method the fracture is divided into N small segments. The resultant normal and shear stresses on the fracture segments is given as

$$\begin{aligned}
\sigma_s^i &= \sum_{j=1}^{N} A_{ss}^{ij} D_s^j+\sum_{j=1}^{N} A_{sn}^{ij} D_n^j\\
\sigma_n^i &= \sum_{j=1}^{N} A_{ns}^{ij} D_s^j+\sum_{j=1}^{N} A_{nn}^{ij} D_n^j \quad \text{for i = 1 to N}
\end{aligned} \tag{6}$$

where $\overset{ij}{A}_{ss}, \overset{ij}{A}_{sn}, \overset{ij}{A}_{ns}$ *and* $\overset{ij}{A}_{nn}$ are the boundary influence coefficients for the stresses which can be calculated from the derivatives given above in Eq. 5. The above system of linear equations is solved for elemental displacement discontinuities of fracture segments by specifying the boundary stresses on the segments. In this work, the conventional two-dimensional DD method is improved by adding special tip elements to accurately find the stresses at the field points near the fracture tips. Also, the prediction of the tangential stresses is improved by using a patch to remedy the shortcoming of the constant element DD as proposed by Crouch and Starfield (1983). Then, a sensitivity analysis is carried out for the multiple transverse fracture case by changing the reservoir properties and studying their effect on the stress distribution and potential rock failure.

3. STIMULATED RESERVOIR VOLUME

3.1 Stress Distribution for a Single Crack with Constant DD

Before studying the stress distribution around multiple transverse fractures, a single constant DD element (Fig 2) in an infinite and stress- free space is considered. The far-field stresses are considered zero so as to focus on the induced values. The crack element is 1 ft in length having 0.2 ft of displacement discontinuity.

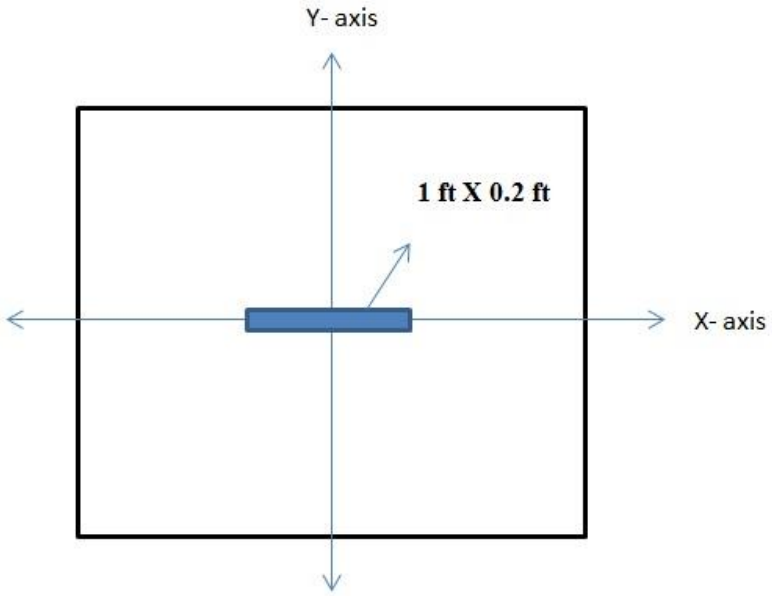

Fig 2. 2D model for single constant DD element.

For a single element having a displacement discontinuity D_y, the stresses along the line y = 0 and are given as following (Crouch and Starfield, 1983):

$$\sigma_{xx}(x,0) = \frac{-aG}{\pi(1-\nu)} D_y \frac{1}{x^2 - a^2}$$
$$\sigma_{yy}(x,0) = \frac{-aG}{\pi(1-\nu)} D_y \frac{1}{x^2 - a^2} \quad (7)$$
$$\sigma_{xy}(x,0) = \frac{-aG}{\pi(1-\nu)} D_x \frac{1}{x^2 - a^2}$$

The normal stresses along the line y = 0 depend only on the normal component of the displacement discontinuity whereas the shear stress depends only on the transverse component D_x. We can see from the above equations that the stresses are singular and discontinuous for x= +a and x=–a, but they are finite and continuous elsewhere along y=0. For the crack element considered here, the normal stress plots of σ_{yy} on y= 0 is shown in Fig. 3. We can see that the area very near to left end of the tip experience high compressive stress whereas right end of the tip experience tensile stresses.

The boundary conditions and the rock properties used in the simulation are given in the **Table 1**. Fig. 4 shows the induced horizontal stresses in the x-direction around the crack when the single constant DD is specified in Fig.2. It can be seen that tensile stress of around 40000 psi is created near the crack tips. If the tensile stress at the tip exceeds the tensile strength of the rock there will be a failure of the crack in the y-direction. The magnitude of induced stresses decreases as we move outside the crack.

Table 1 Parameters used to simulate single crack with constant DD

Parameters	Value	Description
E	$4.5x10^6$ psi	Young's modulus
ν	0.25	Poisson's ratio
σ_H	0 psi	Maximum horizontal stress
σ_h	0 psi	Minimum horizontal stress
Dn	0.2 ft	Normal DD
Ds	0.0	Shear DD
No of Elements	10	
Crack length	1 ft	

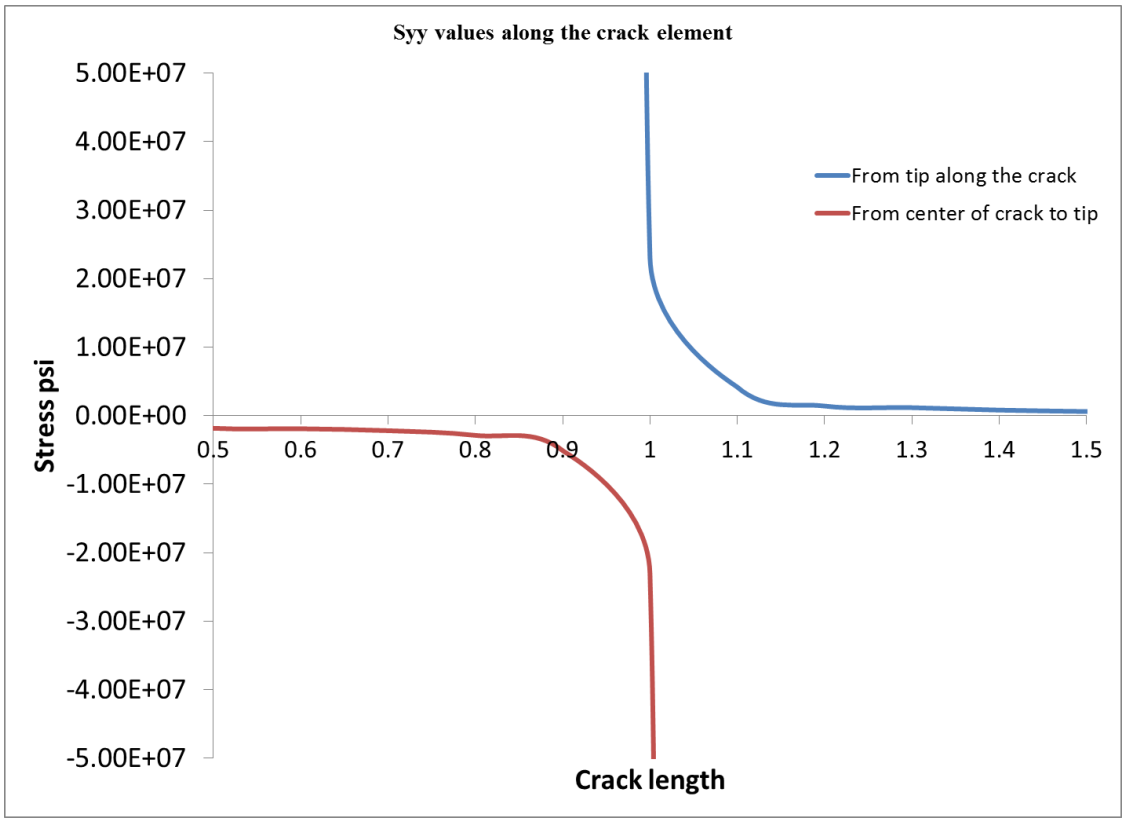

Fig 3. Normal stress S_{yy} values along the crack and near the tips. Due to normal DD (opening of the crack) compressive forces are created along the crack and at the tips stress values become tensile and singular. (tension positive).

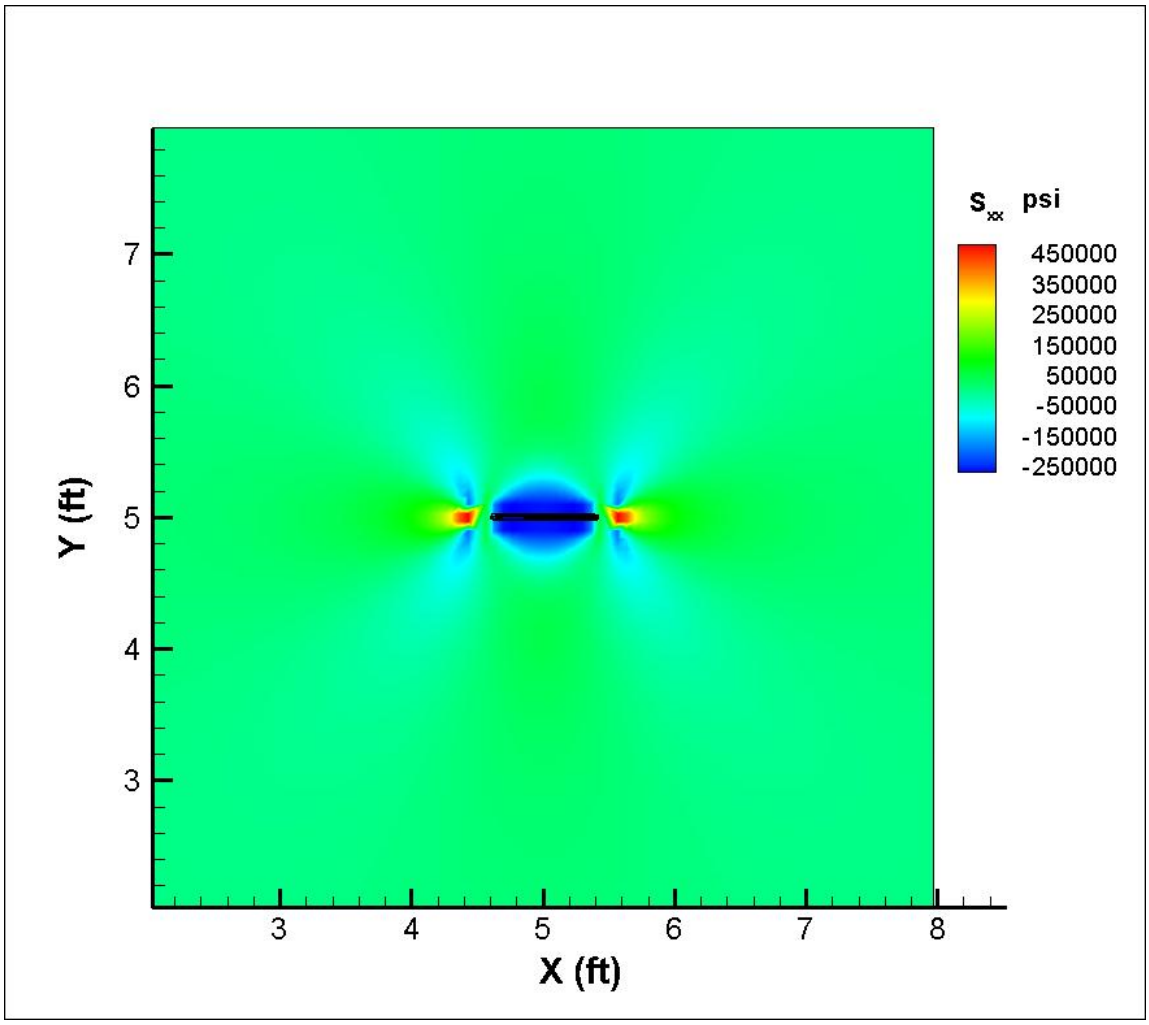

Fig 4. **Induced horizontal stresses in the field the crack is created (S_{xx}, compression negative). The element is shown in black think line. There are compressive stresses induced on the top and bottom of the crack walls and tensile stresses are induced at the crack tips.**

Fig. 5 shows the induced stress in the S_{yy} component of stress. We can see that tensile stresses of magnitude 20000 psi are created at the fracture tips, compressive forces are created along the length of the crack and tensile forces at the tip of the crack.

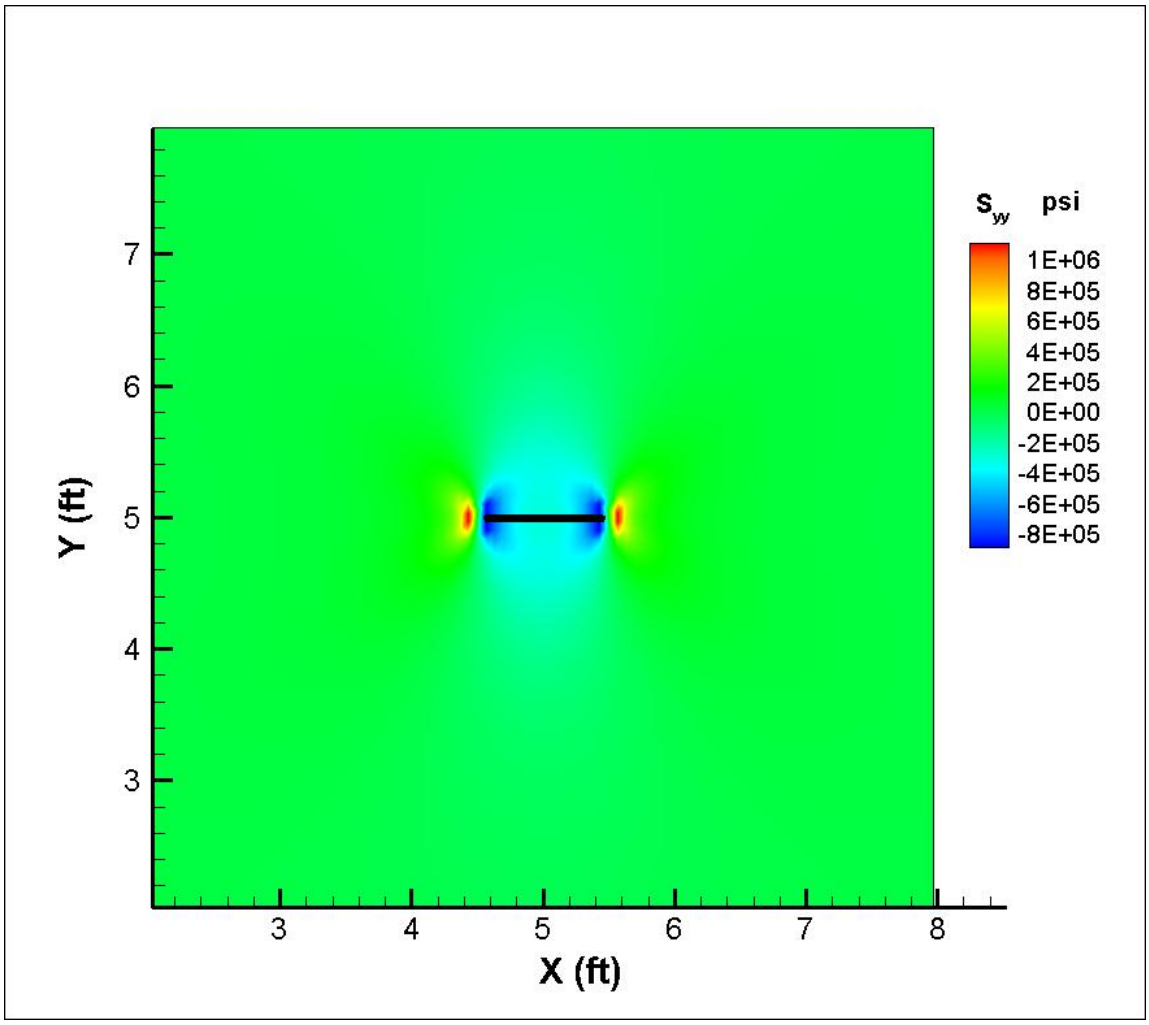

Fig 5. Vertical stresses in the field the crack is created (S_{yy}). Compressive stresses are created along the crack and increased from center to the tips. Element tips experienced large tensile stresses. (compression negative).

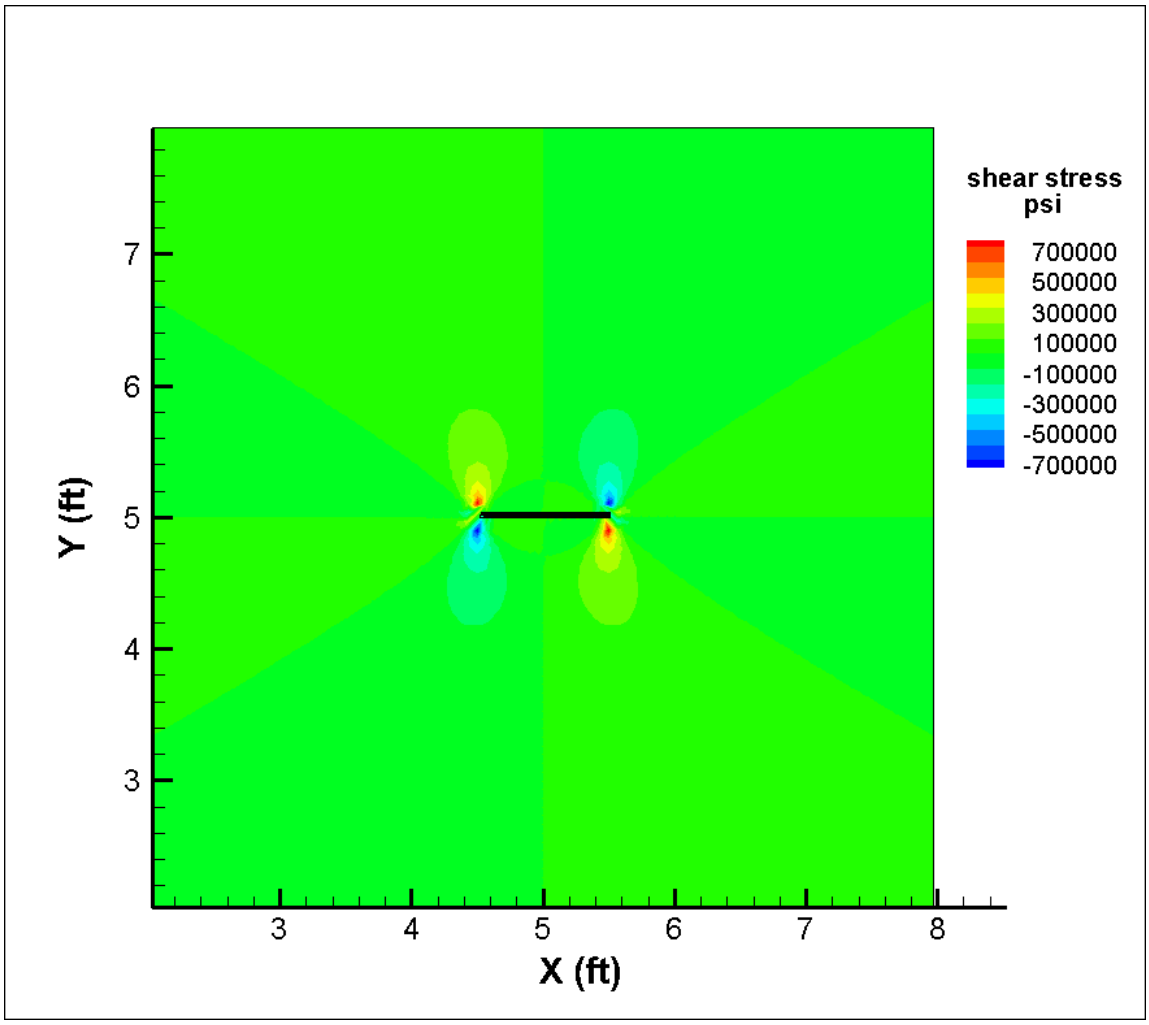

Fig 6. **Induced shear stresses. The shear stresses near the top and bottom surface of the fracture are equal in magnitude but opposite in direction hence keeping the crack in equilibrium. The sign of shear stress only indicates it direction.**

From the Fig. 6 we can see that shear stresses are induced near the top and bottom of tips of the crack. The shear stress component changes sign from one quadrant to another. This is because of the change in the direction of shear DD.

3.2 Stress Distribution and Rock Failure around Multiple Transverse Fractures

Consider a horizontal well in a homogeneous reservoir intersected by 3 horizontal transverse hydraulic fractures each having a half-length of 50ft (Fig. 7). The wellbore is along the y-axis, which is the direction of minimum horizontal principal stress, and the fractures are along the x-axis, which is the direction of maximum horizontal principal stress. All the 3 fractures are spaced parallel to each other as shown in the Fig. 7. The distance between each fracture is 20ft. the origin of co-ordinate axis is taken at the tip of the center fracture.

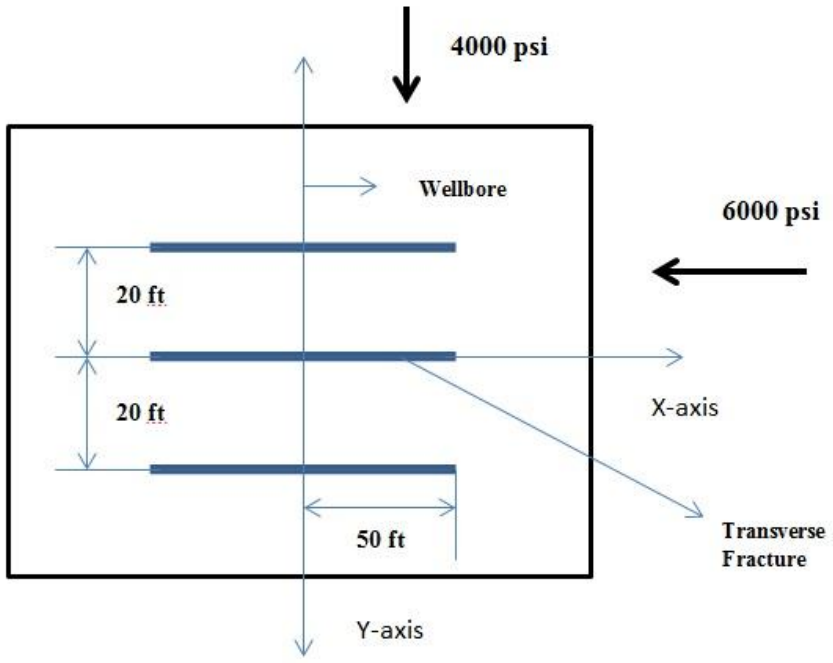

Fig 7. **2D Transverse fracture model and boundary conditions.**

The in-situ stress conditions and rock properties are given in **Table 2** (Cheng 2009). The stress distributions obtained for multiple transverse hydraulic fractures are shown below

Table 2 Parameters used to simulate multiple parallel transverse fractures

Parameters	Value	Description
E	$4.5x10^6$ psi	Young's modulus
ν	0.25	Poisson's ratio
σ_H (S_{xx})	6000 psi	Maximum horizontal stress
σ_h (S_{yy})	4000 psi	Minimum horizontal stress
P_n	500 psi	Net pressure inside the fracture
τ	0 psi	Shear stress
Lh	50 ft	Fracture half length
ws	20 ft	Spacing between the fractures
No of ordinary elements in one fracture	998	
No of tip elements in one fracture	2	
Ordinary element size	0.1ft	
Tip element size	0.1ft	

3.2.1 S_{yy} stress distribution

Fig. 8 shows the induced stresses in S_{yy} direction. This induced value is should be superimposed on the far-field stress to obtain the total stress. From Fig. 8 we can see that induced stresses are higher in areas around the middle fracture where the rock in between is compressed by the pressurization of the three neighboring cracks. There is a very large stress decrease at the fracture tips because of the large tensile forces (hoop stress) induced there. This stress distribution is in accordance with the one obtained for a

single DD element in which is shown in the Fig. 5. The stress interference between the fractures changes the fracture geometries of all the 3 fractures. The fracture widths of all the 3 fractures are decreased because of the high stresses (stress shadow) at the center of the fractures caused by opening of the cracks. The opening of the center fracture is restricted by the opening of top and bottom fractures.

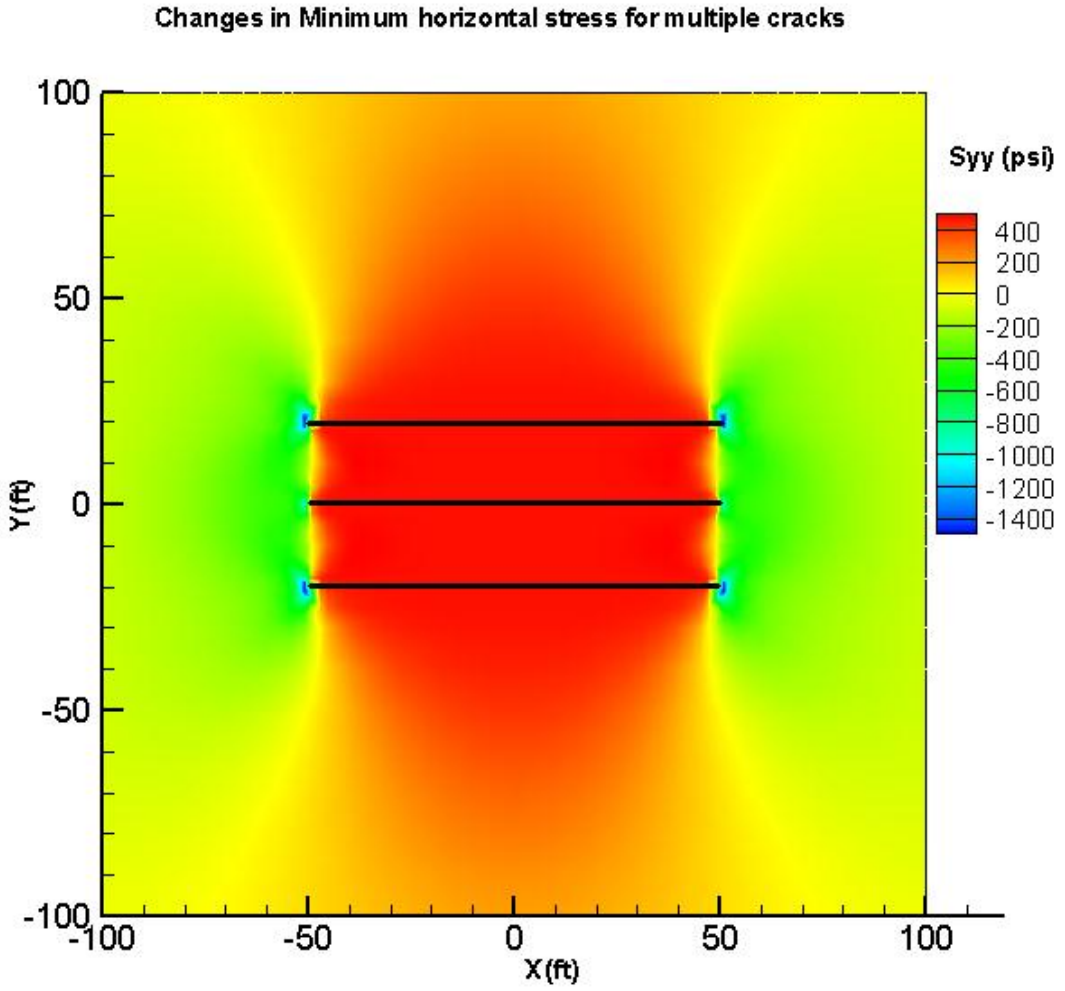

Fig 8. Change in S_{yy} due to the presence of hydraulic fractures. Center of the fractures experienced increase in stress while fracture tips experienced decrease in stress. (compression positive).

3.2.2 S_{xx} stress distribution

Fig. 9 shows the change of stresses in S_{xx} direction. It is interesting to note that the induced values are lower in the area between the fractures where the crack opening is lower resulting in lower induced tangential stress. The fracture tips are experiencing high tensile stresses of around 800 psi.

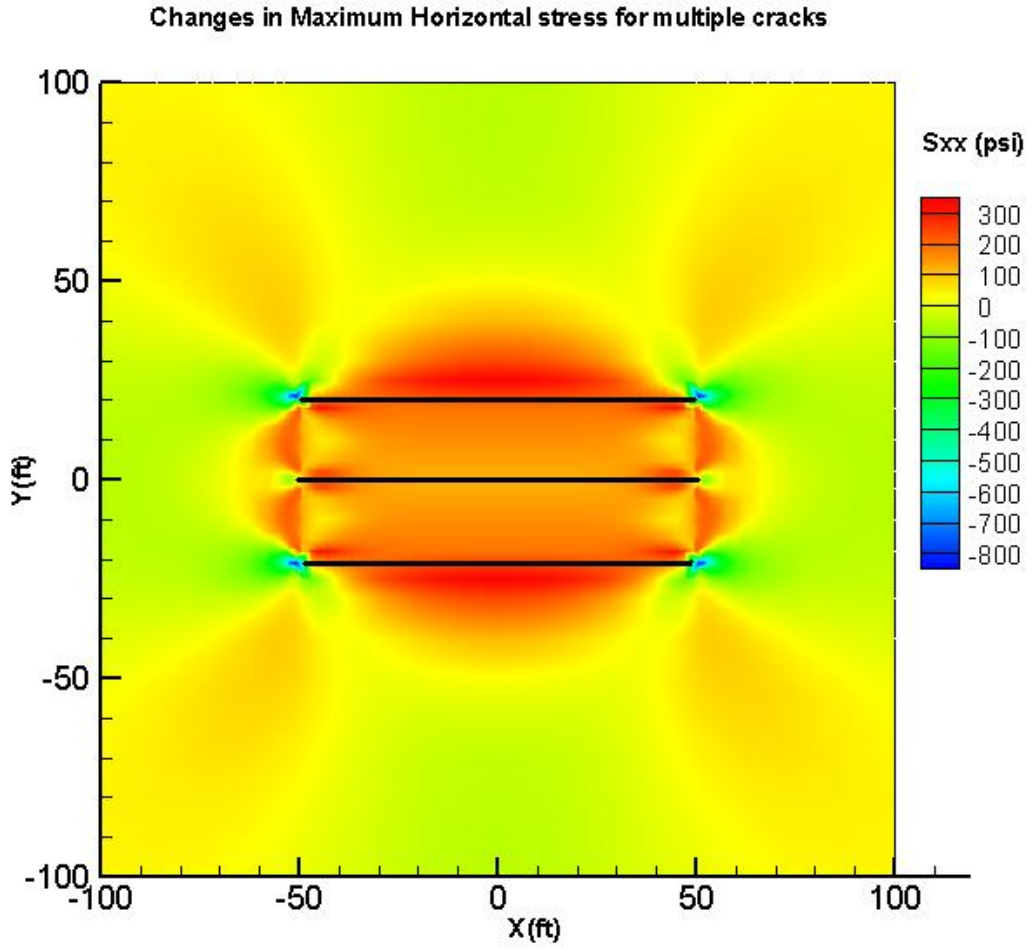

Fig 9. Change in S_{xx} due to the pressurization of hydraulic fractures. S_{xx} is increased more along the outer edges of the outer fractures (compression positive) and those fractures open more.

3.2.3 Induced shear stress

Fig. 10 shows the induced shear stresses. Unlike in shear stresses induced for single constant DD element (Fig. 6) the shear stress induced on multiple cracks tips is not equal in magnitude on the 2 sides (upper and lower) of the top and bottom cracks due to interference of neighboring cracks. The outer surfaces of the outer cracks experienced high shear stresses due to higher deformations as shown in Fig.11. Thus, these uneven shear stresses at the fracture tips will tend to turn the exterior fractures away from the central fracture if they are very close to each other. Sign change in shear stress can be understood from Fig.11 where we can see the displacement of crack elements changes direction from left to right.

3.3 Transverse Fracture Geometries

Fig. 11 below shows the fracture geometries obtained from the simultaneous pressurization. The central fracture does not open as much as the others, the width of the center fracture is 0.00189 ft. which is 6.5 times, lower than the top and bottom fractures (width is 0.0122 ft.). The upper and lower surfaces of the center fracture are symmetrical along its axis, hence no tangential stress discontinuities will be observed between these two surfaces. The top and bottom fracture surfaces are not symmetrical along their respective fracture axis. Hence a tangential stress discontinuity is expected between these surfaces.

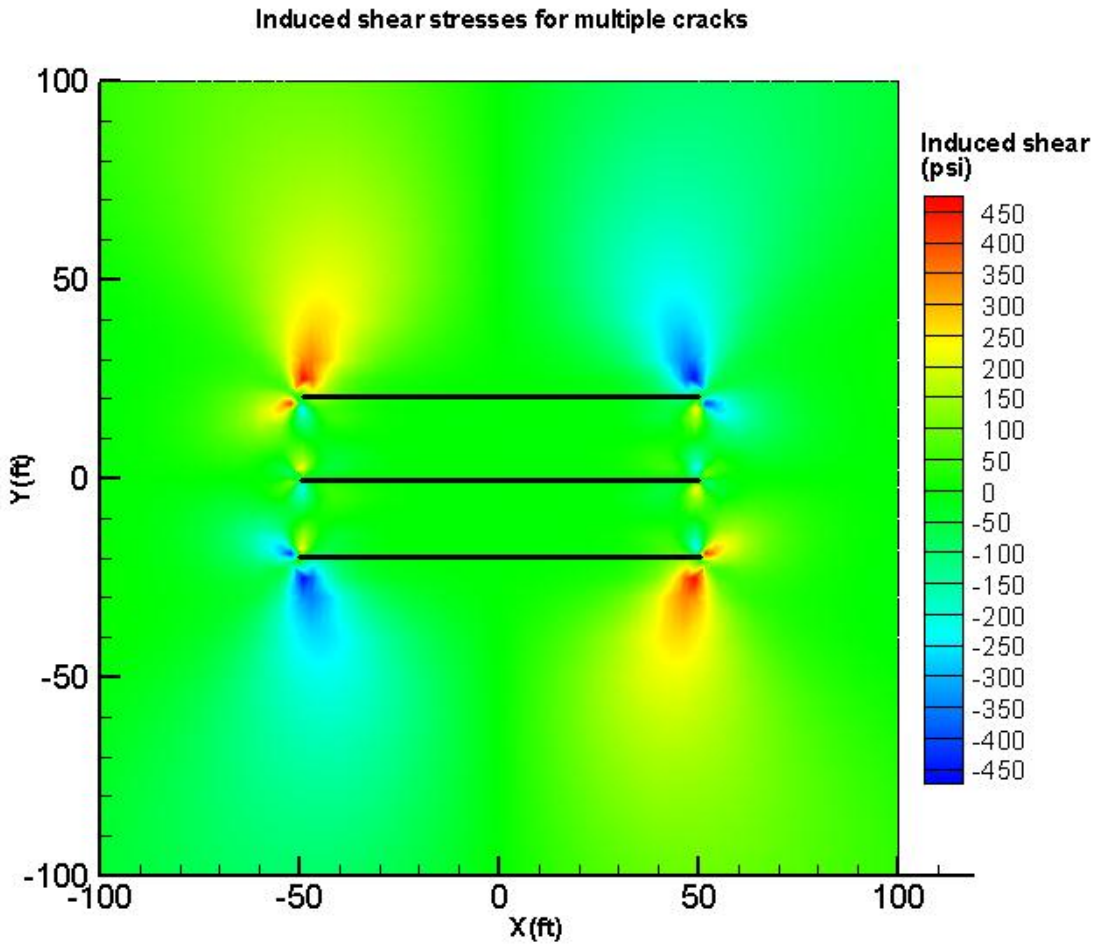

Fig 10. Induced shear stress due to the pressurization of three hydraulic fractures. The high shear stress near the fracture tips of the outer fracture will likely rotate the fractures away from the center fracture and truncate if they are very close to each other. They are also sites of rock failure and induced seismicity.

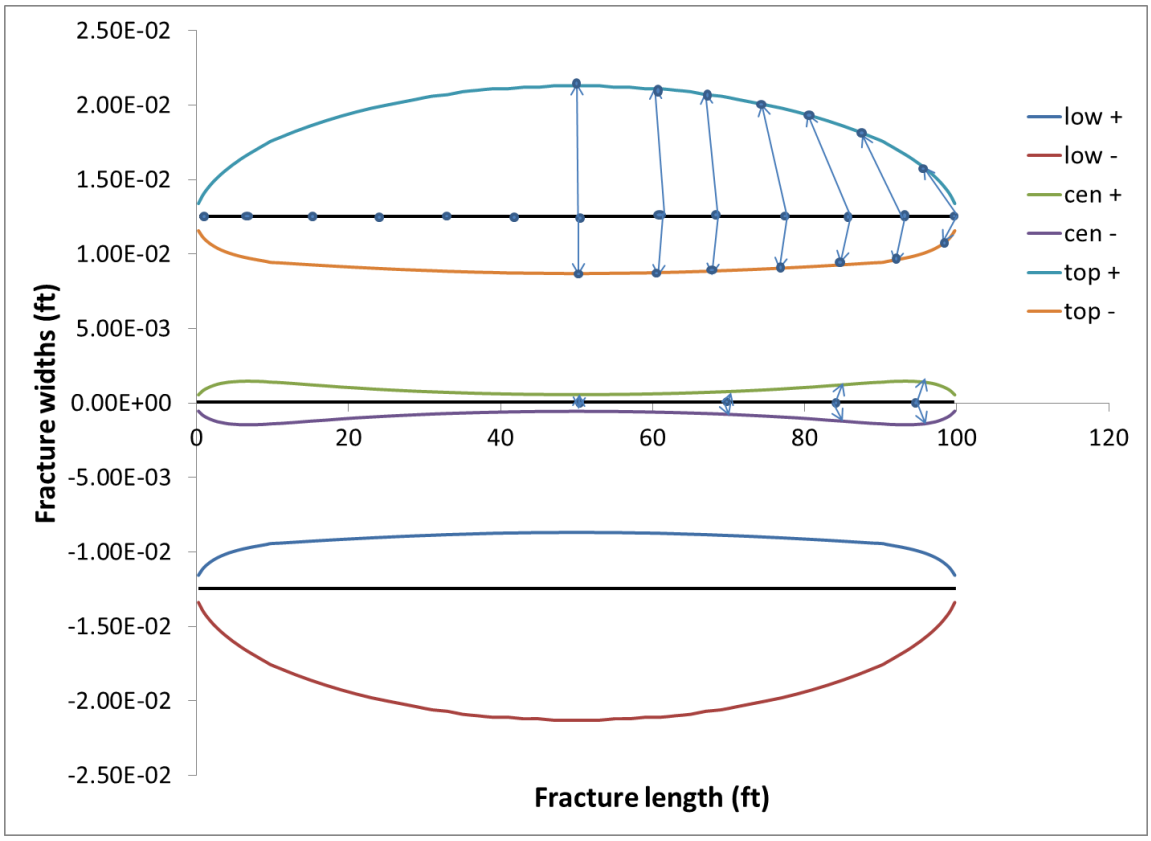

Fig 11. Fracture opening for three transverse fractures. In the legend (+) sign indicates upper surface of the crack and (–) sign indicates the lower surface of the crack.

3.4 Tangential Stress on the Crack Walls

Tangential stresses plays a crucial role in assessing the rock failure, thus an accurate values of the tangential stresses are needed. Fig. 11 shows that the crack walls are deformed as a result of tangential strains on the walls. The maximum tangential stress is obtained on the crack wall where the maximum deformation takes place. Tangential stresses on the two surfaces of the crack are equal if only one crack is present in the field, since the crack surfaces are symmetric along the line of its axis. However, for the multiple crack case the tangential stresses on the 2 surfaces of the exterior cracks are not

the same since the surfaces of the crack are deformed unsymmetrically along their line of axis as shown in Fig. 11. Thus, the tangential stress is discontinuous when moving from one surface of the crack to other of its own. A method to calculate the tangential stresses from the shear DD components of the elements is described in Crouch and Starfield (1983). This method failed to fully capture the discontinuity in tangential stresses, occurring from one surface of the crack to the other surface for cracks with unsymmetrical shapes. Whereas a linear DD method does not have the problem of not being able to model tangential stress discontinuities between crack surfaces (Vijayakumar et al., 2007). Based on this, a patch term is introduced which can be used with constant DD method to directly calculate the tangential stress more accurately on the crack surfaces.

3.5 Improved Method to Calculate Tangential Stresses

The value of the discontinuity in tangential stress at any point along a crack is proportional to the tangential derivative of the shear component of displacement discontinuity at that point. The results are established using the Hooke's law for the case of plane strain. According to Crouch and Starfield (1983), the tangential stress discontinuity along a crack can be calculated from Eq. 8:

$$\sigma_{xx}^{-} - \sigma_{xx}^{+} = \frac{2G}{1-\nu}\frac{\partial}{\partial x}(u_x^{-} - u_x^{+}) \tag{8}$$

The quantity $u_x^- - u_x^+$ gives the shear component of displacement discontinuity (DD) at any point along the cracks. The tangential derivative of this quantity determines the amount of discontinuity in the tangential stress.

The patch term (Vijayakumar et al., 2007) is derived by considering linear shear DD. The constant DD method is modified or patched in manner that enables it to directly calculate tangential stress. The tangential stress discontinuity factor (jump term) that occurs during transition from one surface to other surface is defined by the expression:

$$[\sigma_{xx}]_J = \frac{G\beta}{2(1-\nu)} \tag{9}$$

The slope of the shear DD variation β, for a constant element is estimated using:

$$\beta = \frac{D_{x,i-1} - D_{x,i+1}}{2L} \tag{10}$$

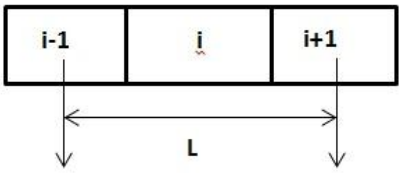

Fig 12. DD Mesh for single crack.

From the Fig. 12, L is the distance between the nodes of the elements i-1, i+1, $D_{x(i-1)}$ and $D_{x(i+1)}$ are the shear displacement discontinuity for i-1 th and i+1 th element respectively.

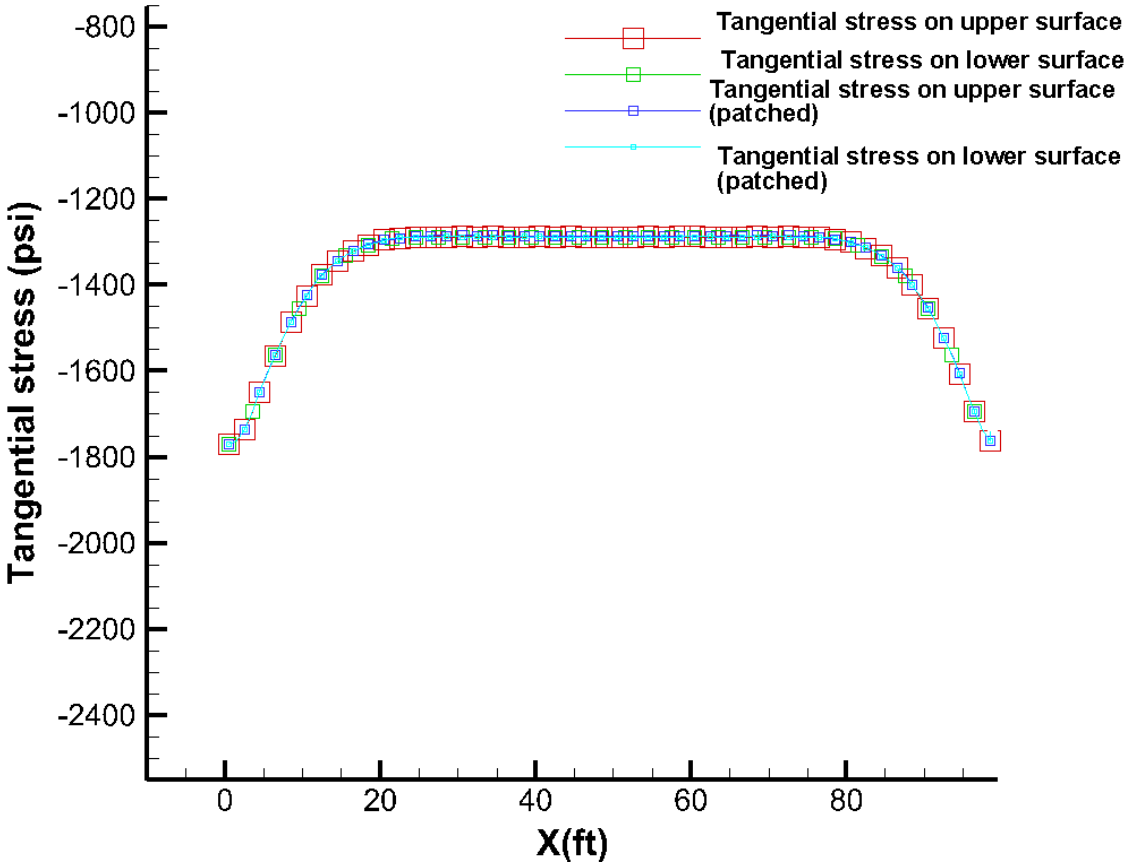

Fig 13. Distribution of tangential stress on the walls of the center fracture. The two sides of the fracture deformed equally, hence no tangential stress discontinuity is observed. The net tensile force exerted on the crack is obtained by subtracting the tangential stress from σ_H.

To obtain the tangential stress for y+ surface at a point x along the crack, σ_{xx} is added to the tangential stress directly calculated from the constant DD method. The tangential stress on y- is obtained by subtracting σ_{xx} from the stress computed from the constant DD method.

For the multiple transverse hydraulic fracture case discussed above, the tangential stresses obtained on the fracture walls are shown below. Fig. 13 shows the tangential stress plot for the walls of center crack. From the Fig. 13 it is observed that there is no tangential discontinuity between the surfaces of the center crack, this is consistent with Fig. 11 which shows the geometry of the center fracture is symmetrical along its line of axis, and also the Fig. 11 shows the displacement of the crack elements, we can see for the center crack the more compressive stress is acting at tips due to movement of the crack elements in the direction towards the tip. Fig. 14 shows the tangential stress plot for the walls of the top crack. Here we can clearly observe the tangential stress discontinuity between the walls of the top (or bottom) crack, which can be explained from the fracture geometry of the top crack from Fig. 11, from where we can see the crack elements are displacing away from the tip causing the tangential stress in tension nature at tips. The wavy nature of tangential stress observed in Fig. 14 is due to the numerical error obtained in choosing constant DD elements for a continuous crack. The fracture geometry of the top crack is not symmetrical along the line of its axis thus the discontinuity in shear DD.

The patch term also plays an important role in accurate calculation of the tangential stresses. Fig. 14 shows the difference of 200 psi (i.e., 40% of net pressure) at the tips and 50 psi (i.e., 10% of net pressure) at the center of the crack, between the corrected tangential stresses and directly calculated tangential stresses from constant DD.

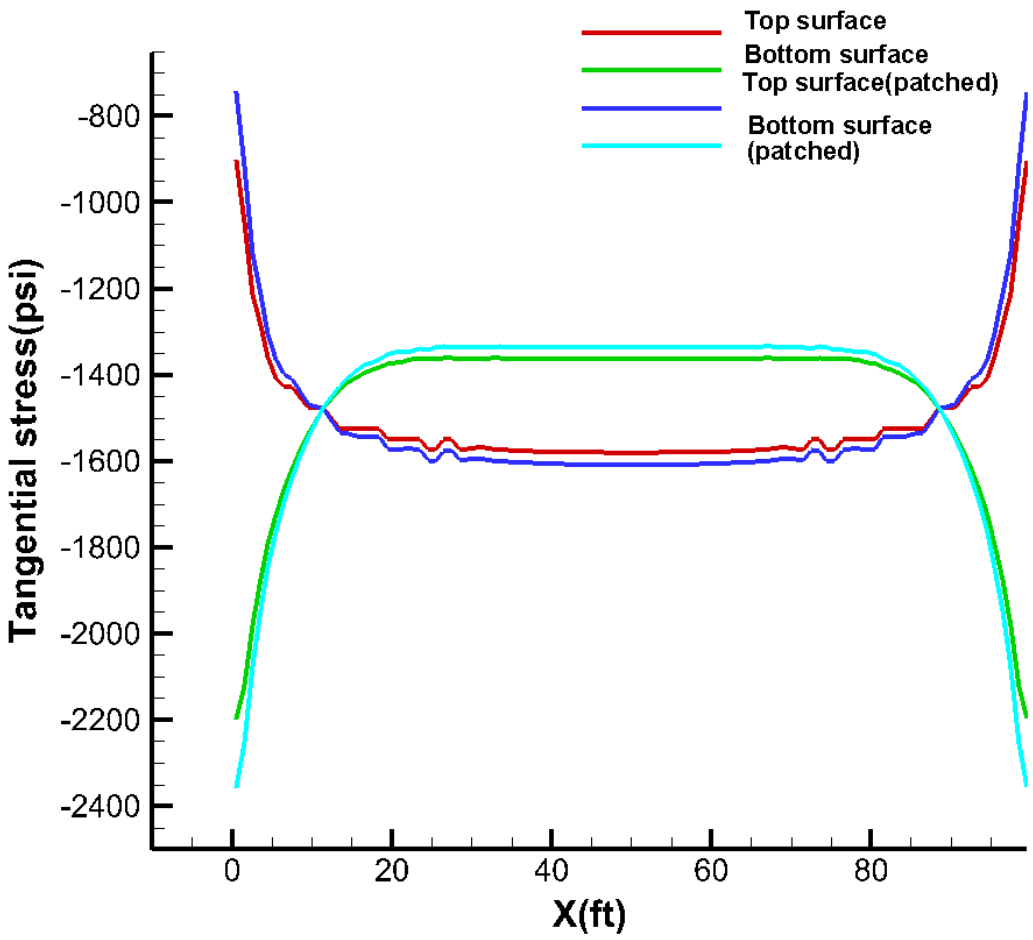

Fig 14. Distribution of tangential stress on the walls of top fracture. The two sides of the fracture deformed unequally (unsymmetrical along the line of the axis of top fracture), hence tangential stress discontinuity is observed.

3.7 Sensitivity Analysis

A sensitive analysis was performed on the multiple transverse fractures. In this analysis three cases are considered with different rock properties shown in the **Table 3**. With the change in rock properties (E, v) the changes obtained in the stress distribution around the fractures and the fracture geometries are studied.

Table 3 Parameters used to simulate sensitivity analysis

Case	E (Young's modulus)	ν (Poisson's ratio)
Case 1	$3x10^7$ psi	0.05
Case 2	$2x10^7$ psi	0.1
Case 3	$1x10^7$ psi	0.45

3.7.1 Changes observed in the stress distribution

There is no change in stress distribution observed with the change in rock properties. However, the effect of the rock properties is directly manifested in the fracture widths. Fig. 15 and Fig. 16 show the variation of the fracture widths for all the 3 cases. There is no change observed in stress distribution because the fracture widths are not prescribed rather they are calculated for a give applied pressure. If the fracture widths are kept constant and the required pressures are determined, then the effect of material properties will be seen in the stress distributions. Accordingly, the stress concentration between the fractures will increase with the increase in Young's modulus. Note that the stress concentration also depends on the spacing between the transverse fractures. The closer the fractures are the more the stress increase is observed in between them.

3.7.2 Changes observed in fracture geometry

The fracture widths are decreasing with increasing the Young's modulus (Fig. 15). For the same net pressure and boundary stresses, it is more difficult to open the crack in a rock with a higher Young's modulus. For a rock with properties in Case 1 the width of

the center fracture is almost negligible, this may cause premature screen out when pumping the proppant in to the fracture, thus much higher net pressure is required to open the center crack. Therefore, in higher modulus rocks it is difficult to create closer multiple transverse fractures (need high net pressures to keep the fractures open which may be uneconomical).

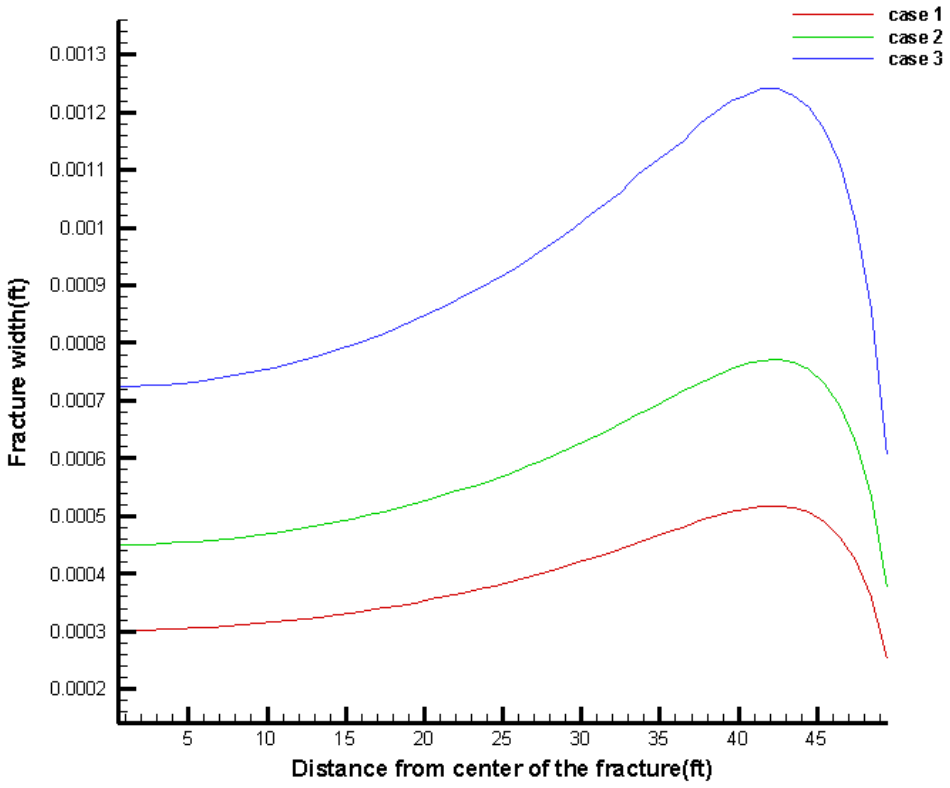

Fig 15. The change in fracture width of center fracture along the length of fracture for all the 3 cases. The higher the Young's modulus and lower the Poisson's ratio, the lower the width of the center fracture.

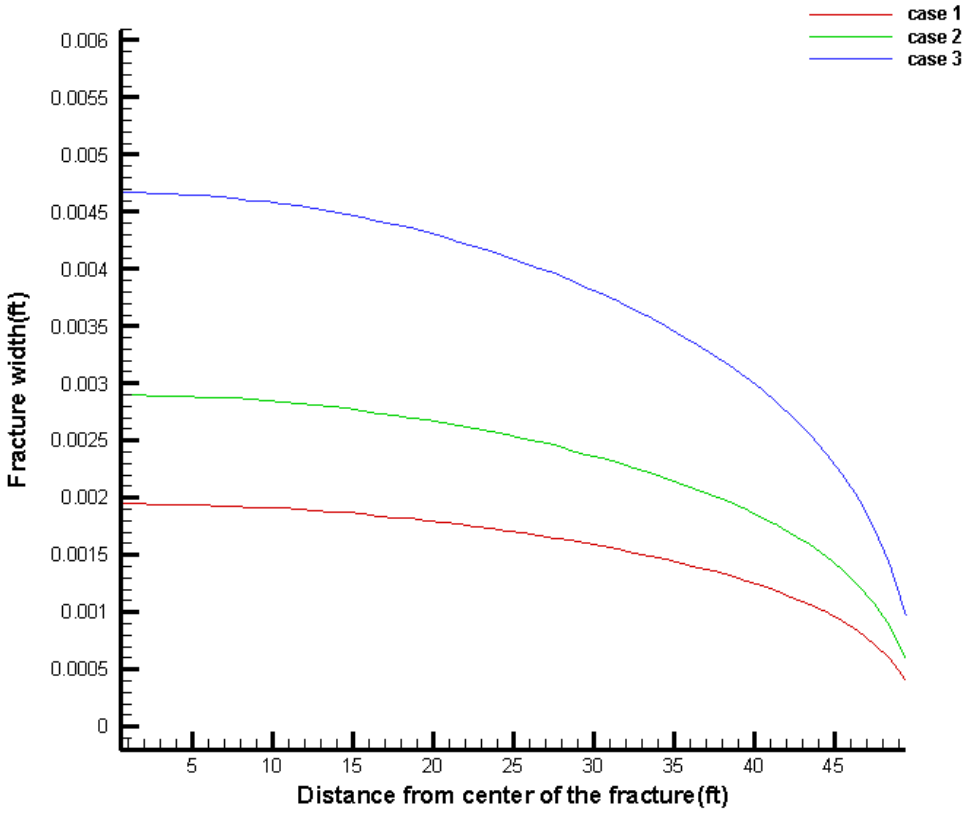

Fig 16. Change in fracture width of top fracture along its length for all the 3 cases. The higher the young's modulus and lower the Poison's ratio, the less the width obtained for top fracture.

3.7.3 Changes in tangential stresses on crack walls

Figures 17, 18 and 19 shows the variation of the tangential stress on the walls of the center and top cracks for all the 3 Cases. Even though there is no change in the stress distribution near the neighborhood of the fractures, there is a significant change in tangential stresses on the walls of the all the 3 cracks with change in rock properties. The tangential stresses on the cracks' walls increases with increase in Young's modulus and Poisson's ratio. This can be explained by noting that increases in Young's modulus

results in less fracture widths and higher stresses build up in the rock. The increase in Poisson's ratio means higher lateral crack wall deformation and thus higher tangential stresses. For the top crack for Case 1 the tangential stress on the upper surface of the top crack at tip is positive (which means it is tensile in nature). If this stress exceeds the tensile strength of the rock, the fracture will fail.

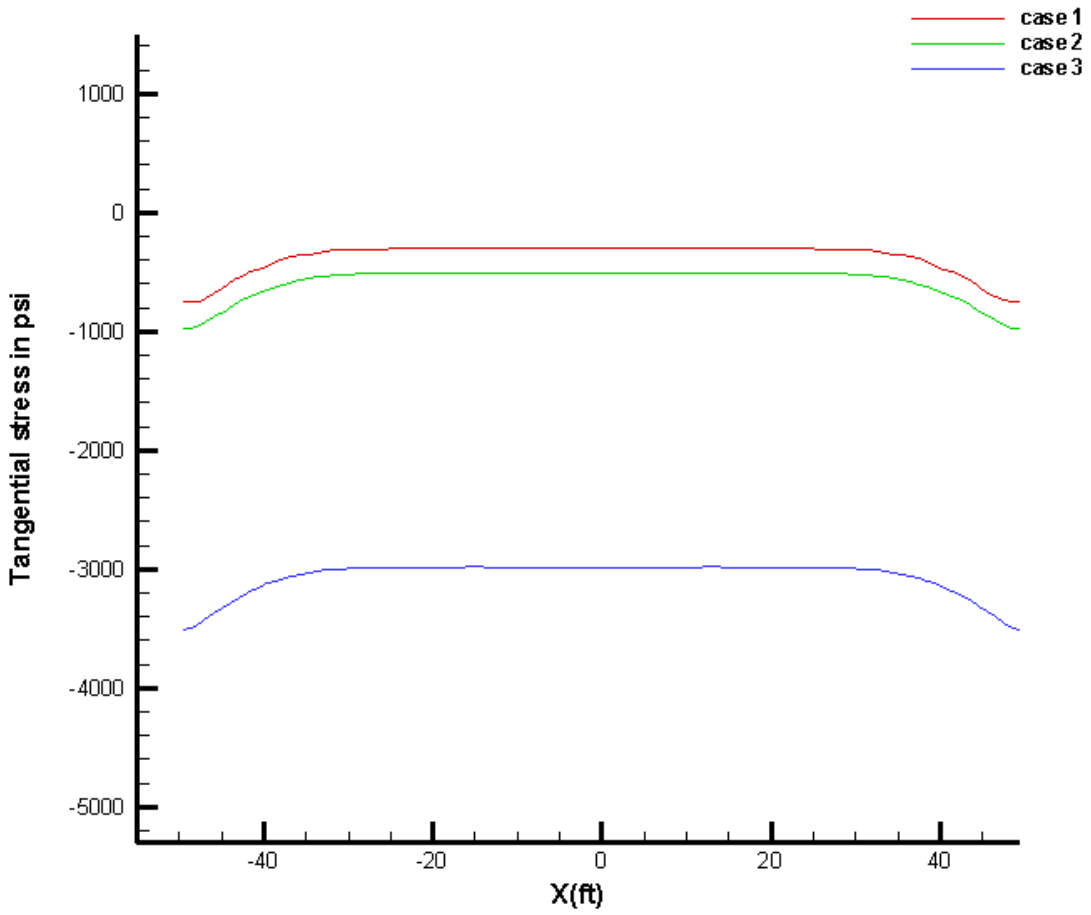

Fig 17. Tangential stress variation on the walls of center crack. With increase in Young's modulus and Poisson's ratio, the tensile stress in S_{xx} direction increases (see Eq. 5) (compression positive)

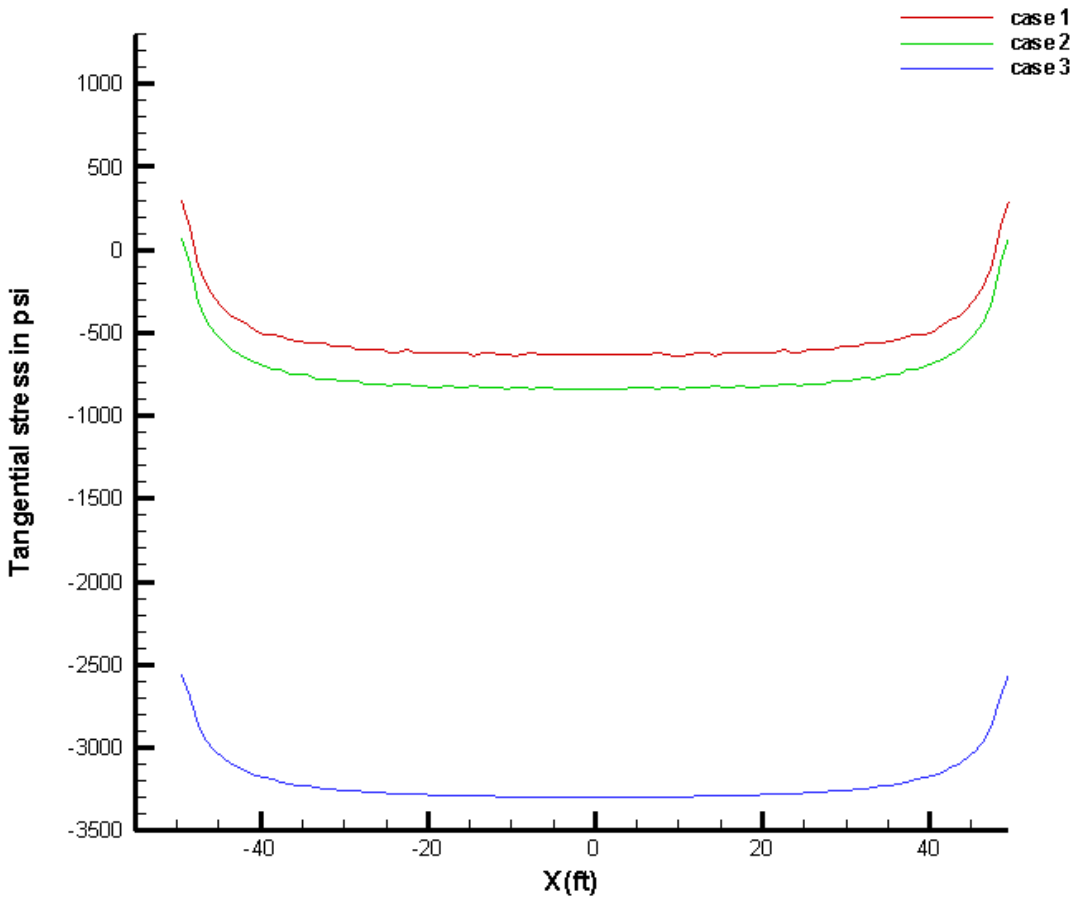

Fig 18. Tangential stress variation on the upper surface of the top crack (and lower surface of the bottom crack) for all the 3 cases.

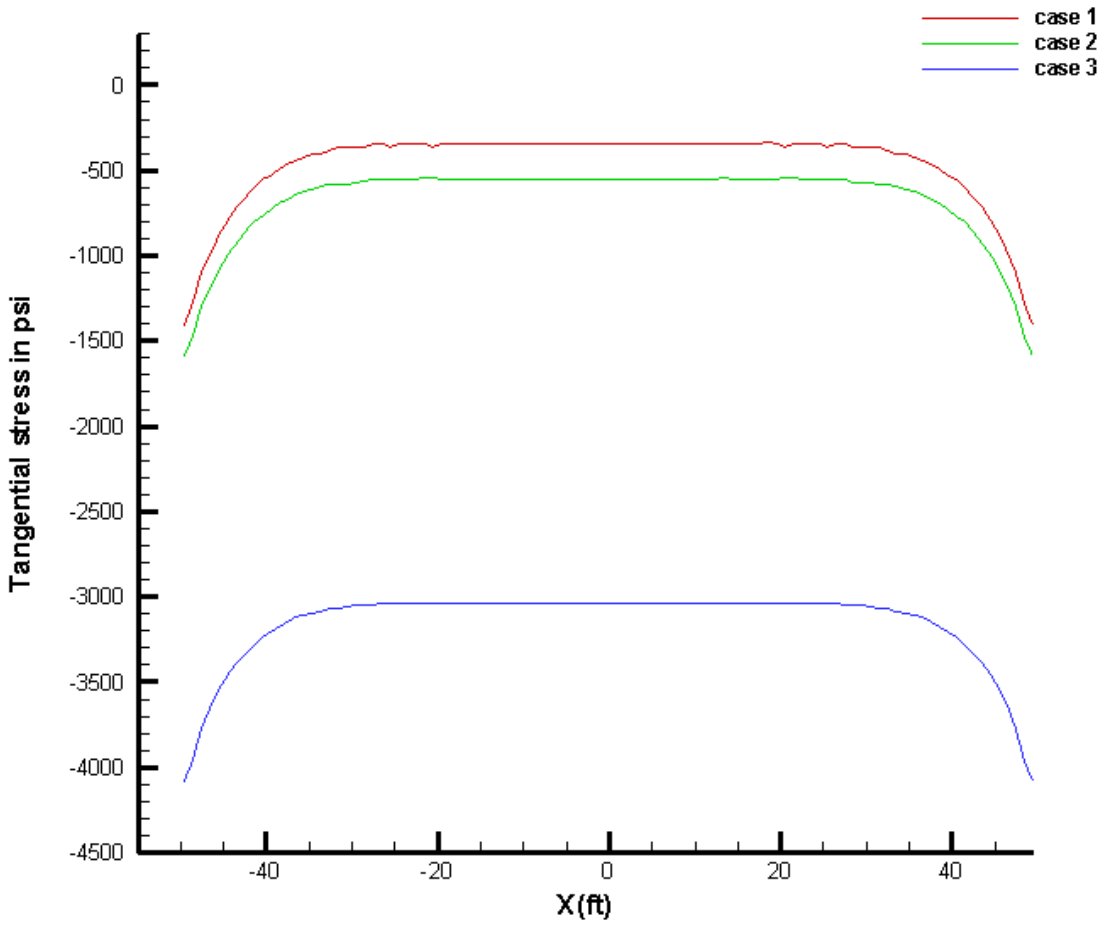

Fig 19. Tangential stress variation on the lower surface of the top crack (and upper surface of the bottom crack) for all the 3 cases.

4. FAILURE POTENTIAL

4.1 Failure Potential

The study of stress distribution near the neighborhood of the fracture is very important to determinate the fracture stability. It can be seen from the stress plots that S_{yy} between the fractures was increased up to 500 psi and S_{xx} increased along the length of the fractures up to 300 psi. The tips of the fracture experience very high tensile stress of around 1200 psi, this tensile stress increase near the fracture tips and the compressive stress increase near the fracture center can cause the stress reversal and thus leading to fracture reorientation by opening another fracture in least resistance path that is in YY-direction (thus creasing longitudinal fracture along the axis of wellbore) if the stress contrast between the 2 in-situ horizontal principle stress is low. The new fractures created will be with low widths and create a more difficultly in communication path between the well and the fractures thus decreasing the productivity. The large tensile forces near the fracture tips can cause mode I type of failure of the rock if the tensile stress near the tips exceeds the tensile strength of the rock. This causes the fracture propagation in the direction of the existing fracture. Thus, these two failures will lead to complex fracture growths around the existing fracture network. The huge shear stresses inducing near the fracture tips (Fig. 10) cause the fracture tortuosity and fracture rotations. In weak plane or on the planes where natural fracture existed the shear stresses lead to the slip of the fractures on weak planes.

4.2 Need for Special Crack Tip Element

It is well known that a reasonably good solution can be obtained by dividing the crack into more elements, but it is apparent that the results are least accurate near the crack tips. An accurate solution near the crack tip is important to predict the fracture failure; hence a more sophisticated approach is needed, which shows the need for the development of the higher order displacement discontinuity elements. (Crouch and Starfield 1983) the simplest higher order element that can be used has a quadratic variation of displacement discontinuity and is constrained to ensure that the slopes of the displacement discontinuities are equal at the nodes of adjoining elements since the slopes will change abruptly at the nodes and stress will be singular at these points. The quadratic elements lead only to a marginal improvement in the numerical solution to the pressurized crack problem, hence we chose special higher order element that takes into account the nature of the stress singularity at the crack tip. From the concepts of fracture mechanics the stress variation near the crack tip is proportional to $r^{-1/2}$ hence the relative displacement between the crack surfaces is proportional to $x^{1/2}$ close to the tip where x is measured from the tip along the crack.

The formulation of crack tip element and comparison of displacements obtained from ordinary elements and crack tip elements is shown in Appendix A.

5. HYDRAULIC FRACTURE PROPAGATION IN THE PRESENCE OF NATURAL FRACTURES

5.1 Introduction

Increased interest in exploration and production of low permeability reservoirs provides new challenges in design and evaluation of hydraulic fracturing (HF) treatments in these reservoirs. Many of the low permeability gas reservoirs, such as gas-bearing shales, and methane-bearing coals usually contain one or more sets of natural fractures that add complexity to HF growth. Under these circumstances, it is necessary to understand HF-NF interactions, and fluid and proppant flow through the pre-existing fractures. Shear stresses accumulated in the rock mass (due to the natural anisotropy of stresses and the presence of discontinuities such as natural fractures and faults) tend to be released during a treatment, triggering shear slippage along the discontinuities and micro-seismicity or micro-earthquakes (Warpinski, Wolhart 2004). Micro seismic fracture mapping is used to map the stimulated volume. It reveals that complex network of fractures can be created in shale reservoir during fracture stimulation. Modeling this process can improve MEQ interpretation and thus reservoir characterization.

The problem of induced and natural fracture interaction has been the subject of many theoretical (Potluri and Zhu 2005), experimental/analytical (Blanton 1982; Warpinski and Teufel 1987), and numerical (Cooke and Underwood 2001; Koshelev and Ghassemi 2003a; Wu and Chudnovsky 2004; Zhang and Jeffrey 2006; Thiercelin and Makkhyu 2007; Nordgren, R.P. 1972) studies. Blanton (1982) presented a simple analytical

fracture interaction criterion relating differential stress and angle of interaction to extrapolate the lab results to field simulations. Warpinski and Teufel (1987) derived a fracture interaction criterion to predict whether the hydraulic fracture causes a shear slippage on the natural fracture plane causing arrest of the propagating fracture or dilates the natural fracture leading to excessive leak-off. Renshaw and Pollard (1995) provided a criterion for crack behavior that is near and orthogonal to un-bonded interfaces. Potluri and Zhu (2005) reviewed various fracture interaction criteria and presented a systematic criterion for different types of fracture propagation modes near natural fractures, based on the conditions of differential stress, angle of intersection, and fracture toughness, and pressure drop within the natural fractures. However, for these analytical attempts, the in-situ stresses along the natural discontinuities were assumed not to have been affected by the hydraulic fracture, i.e., the mechanical interactions between the hydraulic fracture and the natural fractures were not considered. Cooke and Underwood (2001) investigated the local sliding, de-bonding and the subsequent opening along bedding contacts using a Displacement Discontinuity (DD) method to study the probable fracture intersection modes with natural bedding contacts. The bedding contacts they considered were sliding-only interfaces, opening-only interfaces, and both sliding and opening interfaces. However the fracture considered in their study is far-field tension stress driven instead of fluid driven. Koshelev and Ghassemi (2003b) simulated the trajectory of a hydraulically driven crack near natural fractures, and interface between two inhomogeneous blocks using the complex variable hyper singular boundary element method (BEM). They demonstrated that natural fractures and other inhomogeneity's can

generate unstable fracture configurations under different initial crack inclination, loading, and geometry. But the pressure distribution along the hydraulic fracture was assumed to be constant and fluid flow remained to be solved in their simulated process. Wu and Chudnovsky (2004) studied fracture behavior crossing a bi-material interface. They used Griffith type global fracture criterion with anisotropic specific fracture energy, in addition to conventional mass and energy balances. The basic assumption in their study that fluid within the fracture follows a uniform pressure and that the interface is welded and no-slipping remained to be improved. Zhang and Jeffrey (2006) considered fluid flow in the hydraulic fracture and obtained the resulting pressure distribution as it intersected the natural fracture and examined the conditions for further fracture propagation. The rock formation was modeled as an impermeable homogeneous elastic medium, and the fluid was modeled as an incompressible, Newtonian fluid injected at a constant rate. The frictional stress on the surfaces of pre-existing fractures was assumed to obey the Coulomb law. The DD method and the finite difference method were employed to deal with this coupling mechanism of rock fracture and fluid flow.

Thiercelin and Makkhyu (2007) presented a semi-analytical model based on the dislocation theory to predict the reactivation of a natural fault with an approaching hydraulic fracture. They assumed that re-initiation occurs prior to fracture touching the interface. They analyzed the maximum tensile stress on the opposite side of the natural fractures to determine the most probable location of fracture re-initiation. However, the

influence of natural fracture reactivation on the change of in-situ stress and the resultant change of fracture response and interaction mode were not considered. As a result of the complex nature of the problem, these investigations have been limited to the case of one HF approaching a single joint. The results have shown that the fracture patterns that can occur for hydraulically induced fractures propagating near natural fractures can be complex, and are determined by the state of stress in the neighborhood of the intersection and joint material properties.

Generally, four types of interaction have been recognized using the 2D plain strain studies, as shown in Fig. 20. A hydraulic fracture can across the natural fracture without changing direction or it can be terminated by the natural fracture, it can propagate along the natural fracture, or reinitiate and cross the with an offset or jog. Fu et al. (2011) developed a model for HF in a discrete network of fracture. Also, Weng et al. (2011) developed an unconventional PKN fracture model that is capable of predicting hydraulic fracture propagation in a naturally fractured formation. The Natural Fracture deformation and poroelastic effects have not been considered in these models.

Despite their limitations, numerical modeling is an indispensable tool for researchers to obtain a more complete picture of the detailed process of fracture propagation near natural discontinuities. Hydraulic fracture growth behavior in a naturally fractured rock differs greatly from that of an intact rock. Models that can couple fluid flow and rock deformation with frictional and opening behavior of the natural interface and fracture

propagation mechanics are needed to allow estimation of the stimulated volume when fracturing unconventional energy resources.

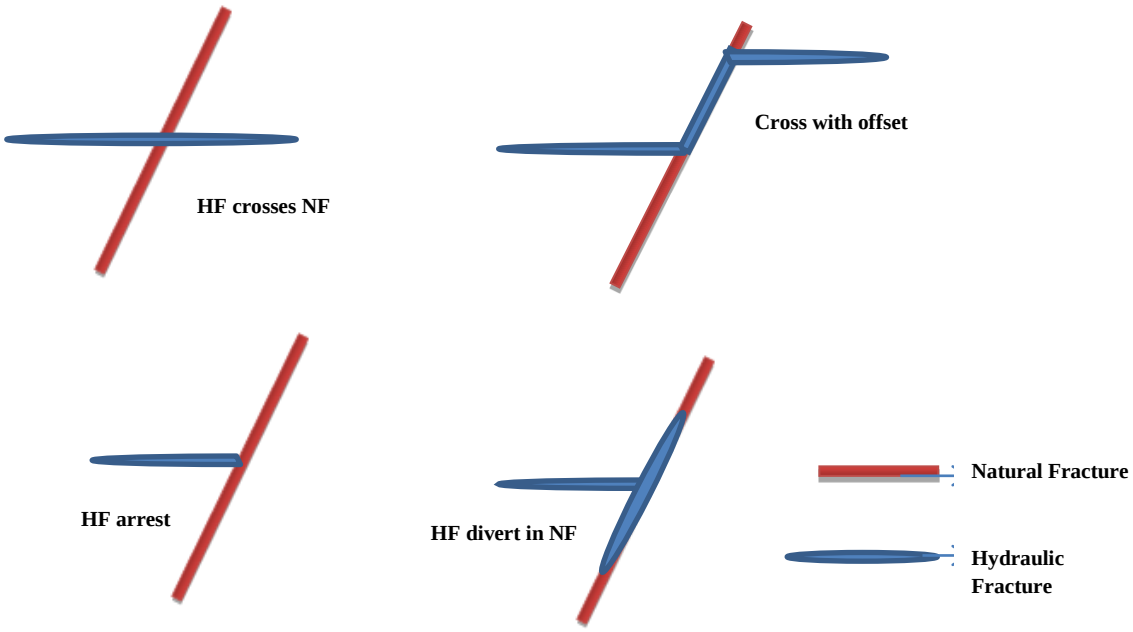

Fig 20. Four types of interaction between hydraulic fracture and natural.

The main feature of this study has been to simulate hydraulic fracture propagation in fractured rock while taking into account natural fracture response under different conditions and considering fluid flow in to the deformable natural fracture to simulate its transition from natural fracture to hydraulic fracture. The model involves coupled fluid flow and fracture deformation using the displacement discontinuity method (DDM) and fluid flow equations.

Often, the model ought to consider poroelastic the effects of pore fluid diffusion on rock deformation to better understand the pressure history recorded during stimulation jobs. These effects are considered in a separate part of this project and will be integrated in the near future.

5.2 Conversion of 3D Fracture Model to 2D Plain Strain Model

In this work, the 3D elliptical fracture model is converted to 2D fracture model by assuming plain strain in horizontal direction (i.e., Y-X plane from Fig. 21). This assumptions means all horizontal sections act independently and width change is only observed along the length of the fracture (i.e., Y- Direction) as shown in Fig. 22. The width is assumed to be constant along the fracture height. This kind of assumption holds well when the fracture height is more than its length.

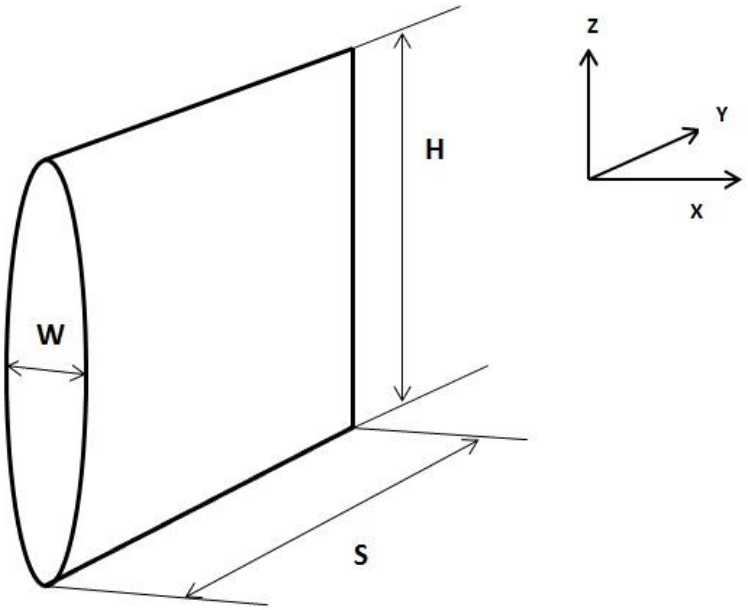

Fig 21. Cross section of 3D elliptical fracture showing w (width), H (height), S (length) of the fracture.

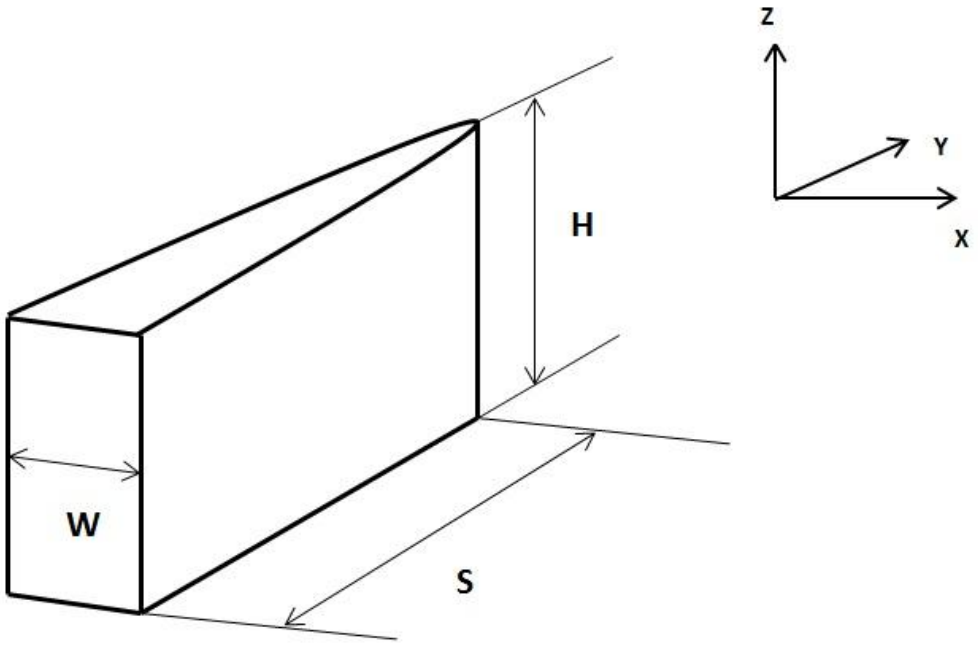

Fig 22. Fracture model with width changing along its length but constant in height. The plane strain is assumed in xy-plane in this model. This model can be compared to KGD model.

5.3 Fluid Flow in a Fracture Network

5.3.1 Governing equation for fluid flow between smooth fractures

The motion of the fluid in the fractures is assumed to be governed by the lubrication equation also called cubic law (Batchelor 1967):

$$\frac{\partial w}{\partial t} = \frac{\partial}{\partial s}\left(\frac{w^3}{\mu'} \frac{\partial p_f}{\partial s} \right) \tag{11}$$

Assuming no fluid leak-off, the global mass conservation equation is:

$$\int_0^l w ds = Q_0 t \tag{12}$$

where: W= width of fracture, X= length of fracture, P_f= fluid pressure inside fracture, μ=

Dynamic viscosity of fluid, and $\mu' = 12\mu$. Currently, it is assumed that no fluid is lost through formation. The boundary conditions are:

At injection point, the fluid flux is equal to injection rate:

$$q(0,t) = Q_0 \tag{13}$$

At propagating fracture tips, the fluid pressure is prescribed. At non propagating fracture tips, no flow boundary condition is given:

$$\frac{\partial q}{\partial s} = 0 \tag{14}$$

The discretization of partial differential Eq 11 is given in Appendix B.

5.3.2 Fluid Flow equation of a connected fracture system

When a hydraulic fracture coalesces with a system of natural fractures, the flow analysis in a fractured network must be considered. In doing this, it is necessary to distinguish between elements of the fracture segments and the intersections where two or more fractures meet. The intersections are the most important geometrical properties of a network for conducting flow. The part of a fracture between two adjacent intersections is called a segment. Considering "n" fracture segments as shown in Fig. 23 connected at intersection "i", and an injection rate, q_i, from the principle of fluid mass conservation, the sum of total inflow rate plus outflow rate should equal to the recharge or discharge rate (Xing 2002):

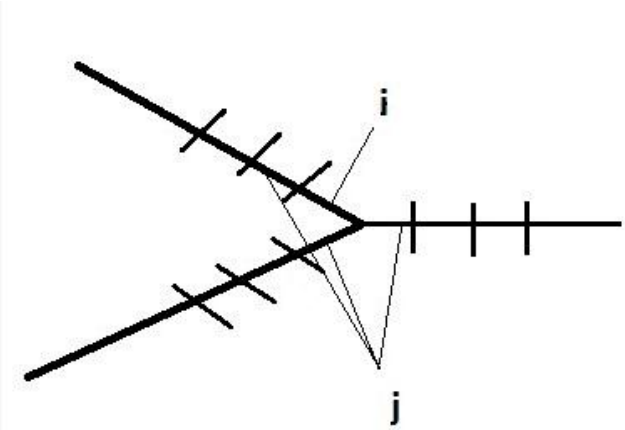

Fig 23. A basic connected fracture system showing intersection i and connected elements j.

$$\sum_{j=1}^{n} \frac{(w_{ij})^3}{12\mu} \frac{p_i - p_j}{L_{ij}} = q_i \tag{15}$$

where p_i and p_j are the pressures at intersection "i" and "j", and w_{ij} and L_{ij} are the equivalent hydraulic aperture and length of the fracture segment between intersections "i" and "j" and μ is the dynamic viscosity of the fluid.

5.4 Joint Element Model

A joint is a natural fracture in rock formed predominantly by mode I failure. For computational purposes, a joint can be assumed as a long, thin crack with a compressible filling. Natural fractures can be assumed as deformable fractures and then a segment of a joint can be treated by using a displacement discontinuity method whose elements have a normal and shear stiffness.

The deformation of the fracture due to an applied compressive stress is called joint closure, which is a non-negative number that increases as the joint compresses. The joint closure is a highly non-linear function of stress and levels off to some asymptotic values as the normal stress on the joint reaches to a high values (Fig. 24). The relation between the joint closures to the stress is given by following empirical relation (Goodman, 1976):

$$\sigma = \sigma_0 \left[1 + \left(\frac{\delta}{\delta_m - \delta} \right)^t \right] \quad \text{for } \sigma \geq \sigma_0 \tag{16}$$

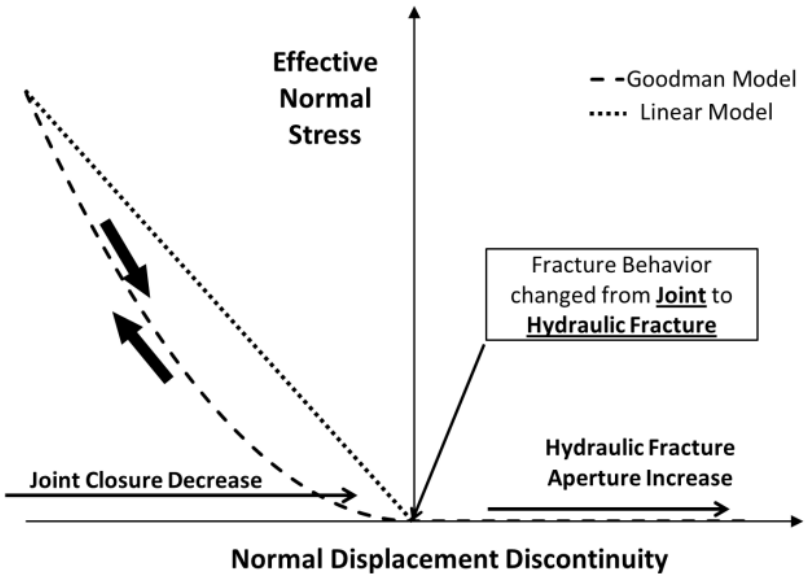

Fig 24. Comparison of Goodman Joint model and a linear joint model. In Goodman model the closure reaches an asymptotic value at high values of normal stress.

where σ_o is some initial stress, t is a dimensionless empirical exponent, and δ_m is the maximum possible joint closure, approached asymptotically as the stress increases.

A linear joint model is given by Crouch and Starfield (1983) in which the joint closure increases linearly with the confining stress. This model assumes that the elements obey simple one-dimensional stress–strain relations for compression and shear. If the joint filling material (thickness hj) is linearly elastic with young's modulus E and shear modulus G, then the normal and shear stresses induced are Crouch and Starfield (1983):

$$\begin{aligned} \sigma'_{yy} &= -E\frac{D'_y}{hj} \\ \sigma'_{xy} &= -G\frac{D'_x}{hj} \end{aligned} \tag{17}$$

The equations in a local s, n co-ordinate system are Crouch and Starfield (1983):

$$\begin{aligned} \sigma'_n &= -K_n D'_n \\ \sigma'_s &= -K_s D'_s \end{aligned} \tag{18}$$

The total stress at element i are given as

$$\begin{aligned} \overset{i}{\sigma}_s &= \left(\overset{i}{\sigma}_s\right)_0^{\infty} + \left(\overset{i}{\sigma}'_s\right)_0 + \overset{i}{\sigma}'_s \\ \overset{i}{\sigma}_n &= \left(\overset{i}{\sigma}_n\right)_0^{\infty} + \left(\overset{i}{\sigma}'_n\right)_0 + \overset{i}{\sigma}'_n \end{aligned} \tag{19}$$

where K_n and K_s are normal and shear stiffness of the joint filling spring.

The above results can be incorporated in to the simple displacement discontinuity stress and displacement equations shown in section 2.2, which results:

- If initial joint deformations are ignored:

$$\begin{Bmatrix} -\left(\overset{i}{\sigma_s}\right)_0 = \sum_{j=1}^{N}\left[\overset{ij}{A_{ss}}\overset{j}{X_s}+\overset{ij}{A_{sn}}\overset{j}{X_n}\right] \\ -\left(\overset{i}{\sigma_n}\right)_0 = \sum_{j=1}^{N}\left[\overset{ij}{A_{ns}}\overset{j}{X_s}+\overset{ij}{A_{nn}}\overset{j}{X_n}\right] \end{Bmatrix} \text{ for } 1 \le i \le M$$

$$\begin{Bmatrix} 0 = \overset{i}{K_s}\overset{i}{X_s}+\sum_{j=1}^{N}\left[\overset{ij}{A_{ss}}\overset{j}{X_s}+\overset{ij}{A_{sn}}\overset{j}{X_n}\right] \\ 0 = \overset{i}{K_n}\overset{i}{X_n}+\sum_{j=1}^{N}\left[\overset{ij}{A_{ns}}\overset{j}{X_s}+\overset{ij}{A_{nn}}\overset{j}{X_n}\right] \end{Bmatrix} \text{ for } M+1 \le i \le N \qquad (20)$$

- If initial joint deformations are considered:

$$\begin{Bmatrix} -\left(\overset{i}{\sigma_s}\right)_0^{\infty} = \sum_{j=1}^{N}\left[\overset{ij}{A_{ss}}\overset{j}{X_s}+\overset{ij}{A_{sn}}\overset{j}{X_n}\right] \\ -\left(\overset{i}{\sigma_n}\right)_0^{\infty} = \sum_{j=1}^{N}\left[\overset{ij}{A_{ns}}\overset{j}{X_s}+\overset{ij}{A_{nn}}\overset{j}{X_n}\right] \end{Bmatrix} \text{ for } 1 \le \text{i} \le \text{M}$$

$$\begin{Bmatrix} -\left(\overset{i}{\sigma_s}\right)_0^{\infty} = \overset{i}{K_s}\overset{i}{X_s}+\sum_{j=1}^{N}\left[\overset{ij}{A_{ss}}\overset{j}{X_s}+\overset{ij}{A_{sn}}\overset{j}{X_n}\right] \\ -\left(\overset{i}{\sigma_n}\right)_0^{\infty} = \overset{i}{K_n}\overset{i}{X_n}+\sum_{j=1}^{N}\left[\overset{ij}{A_{ns}}\overset{j}{X_s}+\overset{ij}{A_{nn}}\overset{j}{X_n}\right] \end{Bmatrix} \text{ for M+1} \le \text{i} \le N \qquad (21)$$

where N is the total number of elements and M is the number of normal elements. K_s, K_n are shear and normal stiffness's of a joint element and X_s, X_n are the total joint shear and normal deformations respectively.

Given the far field stresses $(\sigma_{ij})_0^{\infty}$ and stresses acting on the joint element, the total joint deformation i.e. sum of initial (displacements due to initial stresses on the joint) and induced (displacements due to induced stresses caused disturbance created by fracturing in the formation) can be calculated from the above set of linear equations. The maximum

deformation of a joint element is limited by its closure value (Fig. 24). For a joint in equilibrium condition (i.e., joint do not deform due to initial stresses) the far field stresses are zero in the above equation. In this work, a linear joint model used with normal and shear stiffness and maximum closure specified.

5.5 Fluid Flow in Natural Fractures

Natural fracture in initial state is assumed to be supported by asperities and is hydraulically conductive. When fluid is pumped into the natural fracture the asperities will become contact free and the natural fracture will be transformed to a hydraulic fracture. This transition can be simulated by using the joint model described in section 5.4. As the fluid is pumped in to the natural fracture, the effective stress on the natural fracture decreases thus, decreasing its closure, increasing its aperture. The closure at every time step is calculated to find if the natural fracture is mechanically opened or closed. Increase in fluid pressure will continue to separate asperities, and to increase the stress intensity at the tip of the fracture, which eventually causes propagation.

5.5.1 Joint Contact Iterations

For problems involving joint elements, the state of the contact (stick, yield or open) and the displacements/stresses of each element along the joint are unknown. But if the contact mode is determined, the corresponding governing equations relating the stresses and DD in can be used to solve the DD at each element. Then, the stresses along the joint can be obtained and used to check the contact state again. If the new and the old contact modes are not in agreement, the assumed contact mode must be changed and DD must be solved again. The process will be stopped when the new and the assumed

contact modes are the same and resultant DD and stresses along the joint converge and are known. The corresponding governing equations relating the stresses and DD can be used to solve the DD at each element (Wenxu 2010).

5.6 Fracture Propagation Scheme

The fracture tips are allowed to propagate after every time step for the examples shown in sections from 6.1 to 6.6 without checking the condition for propagation (i.e. $K_I = K_{IC}$). For the simulation of fracture network containing flaw (section 6.7) the condition for propagation is checked in every time step. The model includes square-root tip elements that allow one to calculate the stress intensity factors with relative accuracy. The displacements obtained at the center of the tip element are used to calculate the SIF using the one point formulation. The equations to calculate stress intensity factors are given in Appendix A.

The propagation path of the fracture is calculated using the method of Stone and Babuska (1998) as implemented in Tarasovs and Ghassemi (2010) in which the crack is extended using linear straight line segments. The crack propagation direction (Eq. 22) relies on the maximum tangential tensile stress criterion so that one can use the ratio of the stress intensity factors to compute the angle at which the crack will grow. The crack is assumed to propagate in the direction where the mode II stress intensity factor K_{II} becomes zero.

$$\theta(K_I, K_{II}) = \begin{cases} 0 & if\ K_{II} = 0 \\ 2\arctan\left(\dfrac{\dfrac{K_I}{K_{II}} - \mathrm{sgn}(K_{II})\sqrt{\left(\dfrac{K_I}{K_{II}}\right)^2 + 8}}{4} \right) & if\ K_{II} \neq 0 \end{cases} \tag{22}$$

5.7 Coupling of Fluid Flow and Fracture Deformation

Displacement discontinuity method is used to find the fracture deformation for a given pressure distribution. The fluid injection into the fracture results in change in fluid pressure inside the fracture, which in turn changes the fracture aperture. Thus, the fracture pressure and aperture depend on each other. To solve this problem, the fluid flow is coupled iteratively with DD in order to obtain a unique solution. The coupling is done by assuming the initial pressure distribution in the fracture and finding an initial DD. The calculated DD is then used in the flow solver to find the fluid pressure. This modified fluid pressure is substituted in DD and the same process is continued until the norm associated with the assumed pressure distribution and obtained pressure distribution is less than a prescribed tolerance. Since the problem becomes highly non-linear with more complicated fracture geometries, a simple iterative method will not converge to a solution. Hence we applied Newton-Raphson iterative method to obtain a stable solution to the problem. The iterative algorithm is given in Appendix C.

6. NUMERICAL SIMULATIONS

In order to verify the numerical model and to show its capability, a number of simulations are considered next.

6.1 Injection into Natural Fracture

In this case we consider a natural fracture subjected to fluid injection and the transition from natural fracture to a hydraulic fracture is simulated. The geometry considered is shown in Fig. 25. The input parameters are given in **Table 4**. The results are shown in Figures 26, 27 and 28.

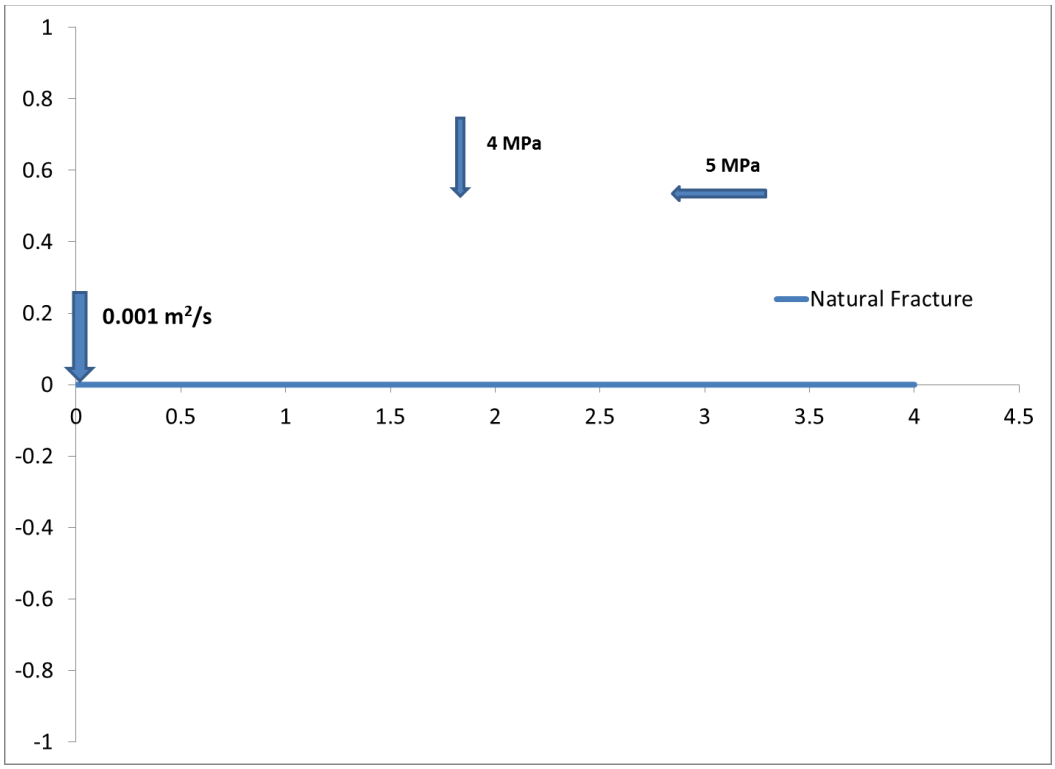

Fig 25. Geometry of single natural fracture, injecton at one end.

Table 4 Parameters used to simulate injection into single natural fracture.

Parameter	Value	Units
Injection rate (Q_0)	0.001	m^2/s
Fluid dynamic viscosity (μ)	0.001	Kg/m.s
Young's modulus (E)	2.7E10	Pa
Poisson Ratio (ν)	0.25	
Max.Horizontal Stress (σ_H)	5	MPa
Min.Horizontal Stress (σ_h)	4	MPa
Natural Fracture Length	4	m
Normal Stiffness (K_n)	0.5E10	Pa/m
Shear Stiffness (K_s)	0.25E10	Pa/m
Max closure allowed(δ_m)	0.3	mm
Hydraulic aperture	0.1	mm

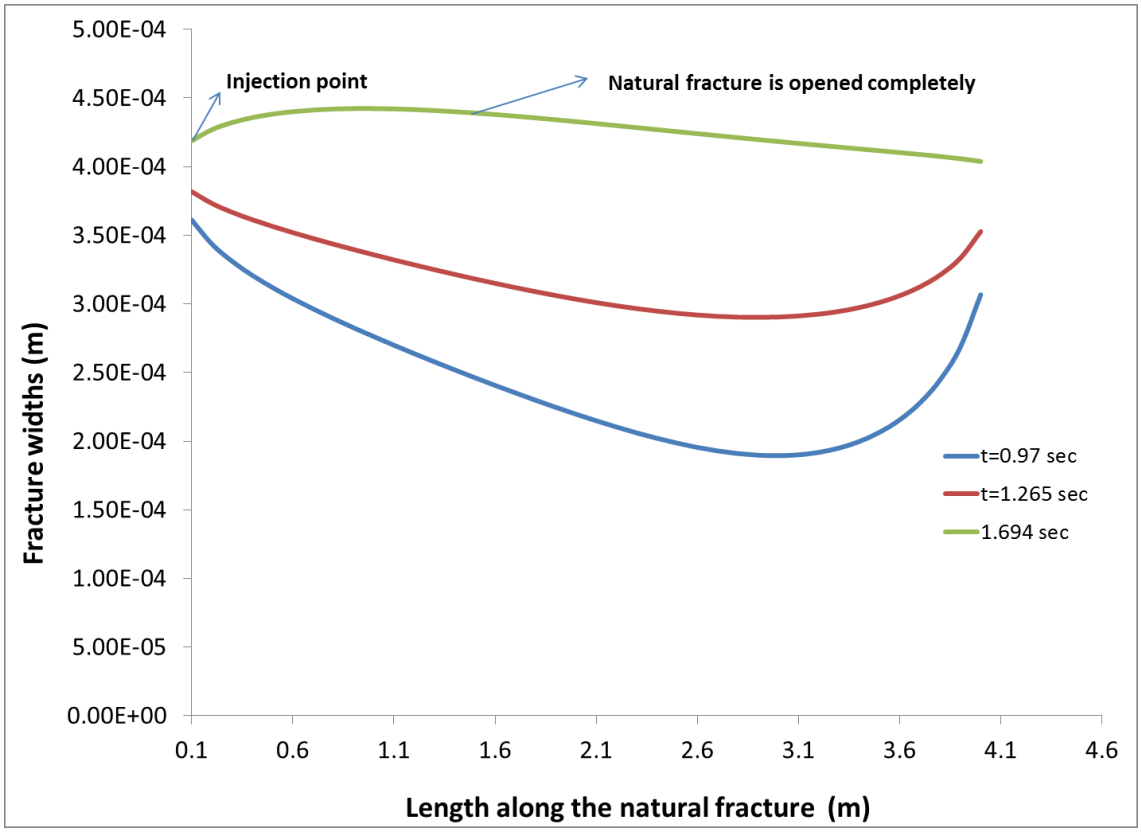

Fig 26. The change in aperture of natural fracture with time as the fluid is injected in to the natural fracture. The NF eventually is transformed into a hydraulic fracture. For the case considered here the transition happened at 1.694 sec.

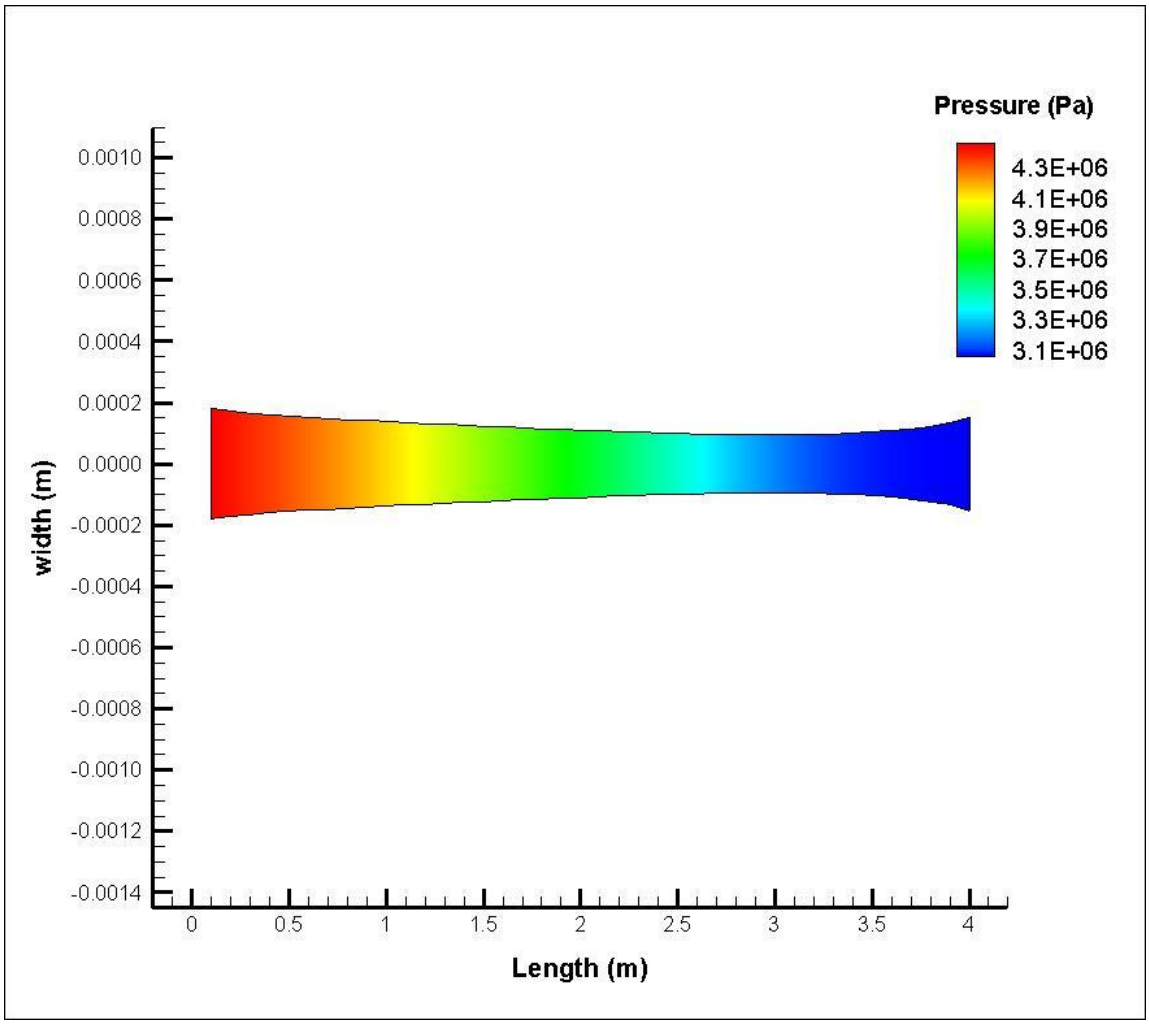

Fig 27. The aperture/pressure of natural fracture at 0.97 sec. The aperture is decreasing along the natural fracture from the injection point to the right end. In the Fig. 26 the aperture at the tip is larger because of the consideration of non-uniform initial closure along the natural fracture. The natural fracture is still closed mechanically but is hydraulically open.

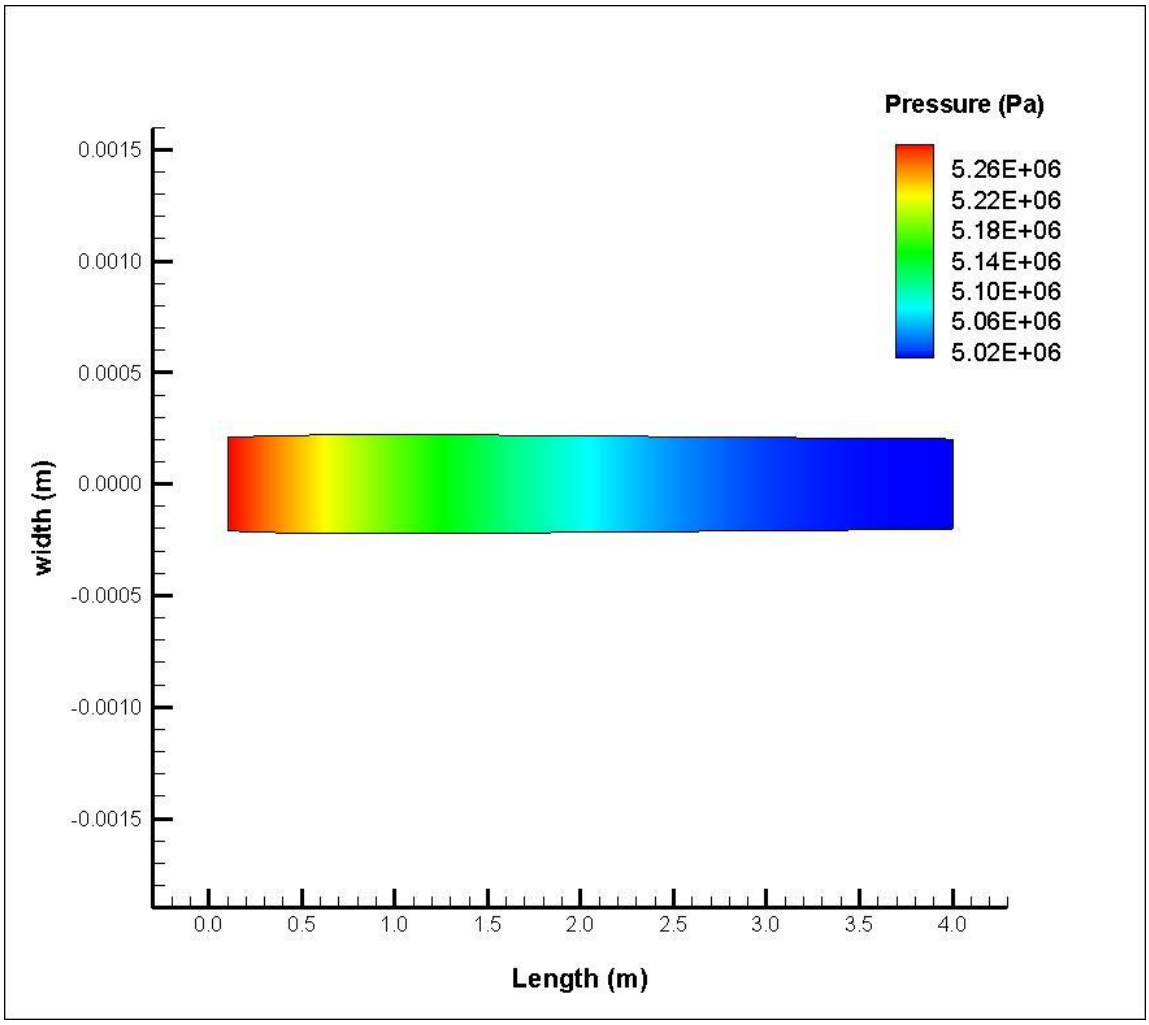

Fig 28. The aperture/pressure of natural fracture at 1.7 sec. The natural fracture is now completely opened and behaves like a hydraulic fracture with widths decreasing along the fracture from injection point (the maximum width is not at the injection point because we are injecting at the tip of natural fracture) to the tip (see green curve in Fig. 25) and eventually propagates when Mode I stress intensity factor equals the fracture toughness.

6.2 Hydraulic Fracture Approaching a Natural Fracture

Consider the interaction between a hydraulic fracture and a natural fracture as aligned in Fig. 29. The natural fracture is assumed to be in non-equilibrium with in-situ stresses. The presence of an inclined natural fracture affects the trajectory of the hydraulic

fracture which leads to a complex fracture model.

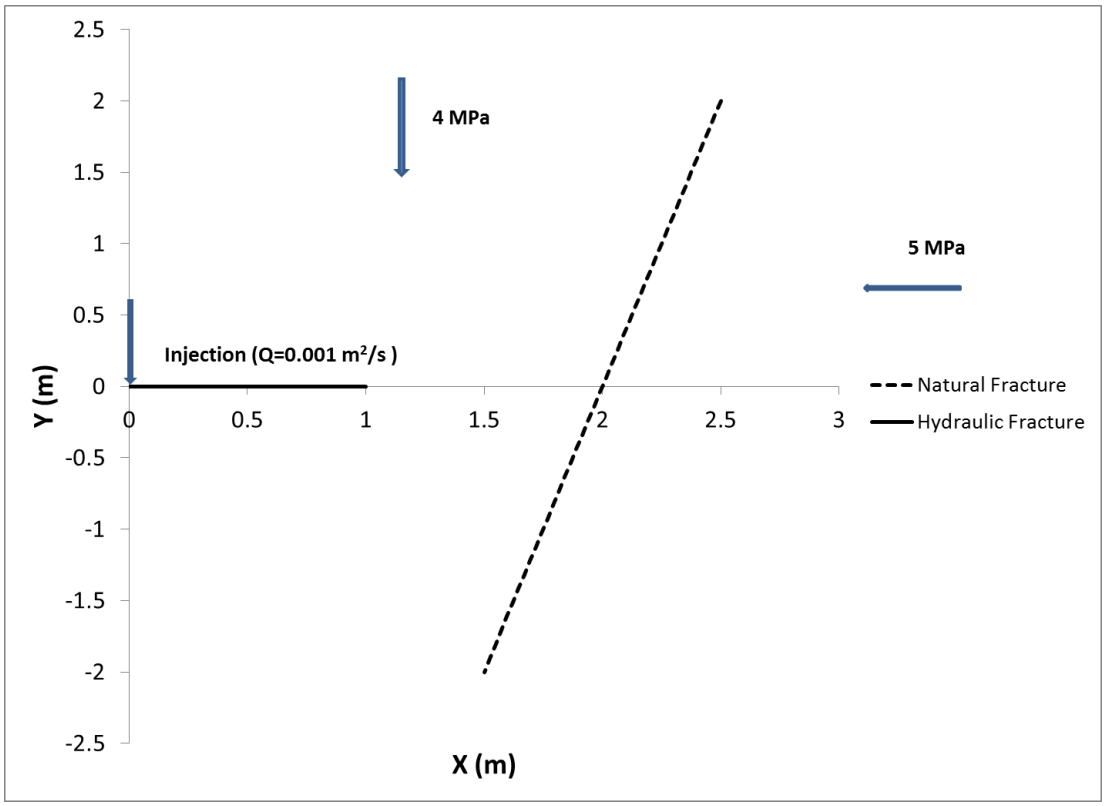

Fig 29. Geometrical configuration of hydraulic and pre-existing fracture for section 6.2.

As the hydraulic fracture tip reaches near natural fracture, coalescence is considered (node to node). To implement this after coalescence the entire fracture network shown in Fig. 30 must is re-meshed as shown in Fig. 31 such that coalescence occurs node to node. After coalescence the fluid will move towards the intersection point at which flux continuity condition for flow into and out of the point are imposed.

Fig. 32 shows the hydraulic fracture trajectory near an inclined natural fracture for the properties given in **Table 5**. The change in the hydraulic fracture path is due to the altered stress field by the deformation of the natural fracture. The fracture trajectory depends on the factors such as far-field stresses, geometry of natural fracture, hydraulic fracture and fluid properties.

Table 5 Parameters used to simulate HF approaching NF which not in equilibrium with in-situ stresses

Parameter	Value	Units
Injection rate (Q_0)	0.001	m^2/s
Fluid dynamic viscosity (μ)	0.001	Pa.sec
Young's modulus (E)	2.7E10	Pa
Poisson Ratio (ν)	0.25	
Max.Horizontal Stress (σ_H)	5	MPa
Min.Horizontal Stress (σ_h)	4	MPa
Natural Fracture Length	4	m
Initial Hydraulic Fracture Half Length	0.5	m
Normal Stiffness (K_n)	0.5E10	Pa/m
Shear Stiffness (K_s)	0.25E10	Pa/m
Max closure allowed(δ_m)	0.3	mm
Hydraulic aperture	0.1	mm

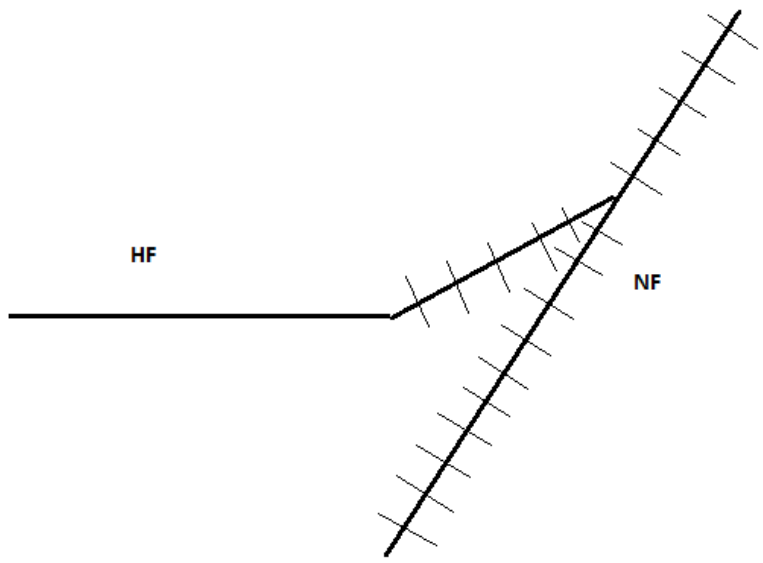

Fig 30. **HF-NF coalescence with initial meshing.**

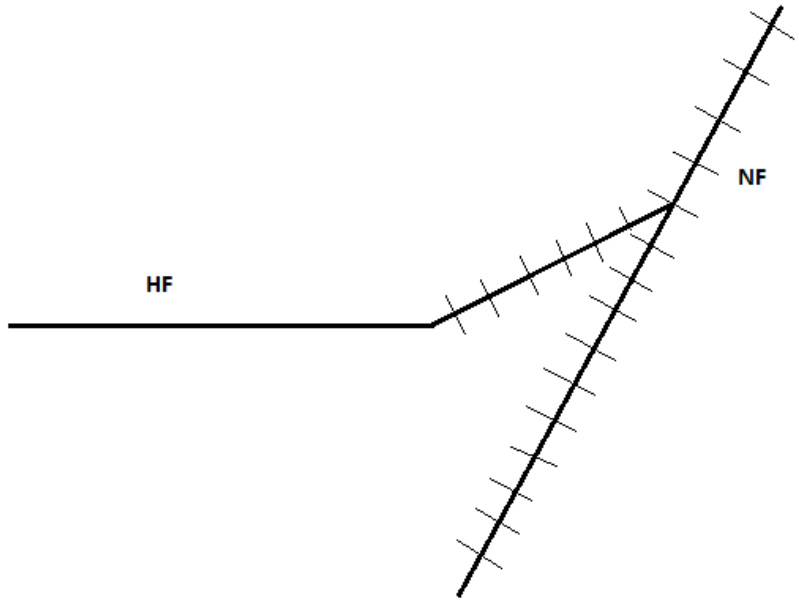

Fig 31. **HF-NF coalescence after re-meshing making it node to node.**

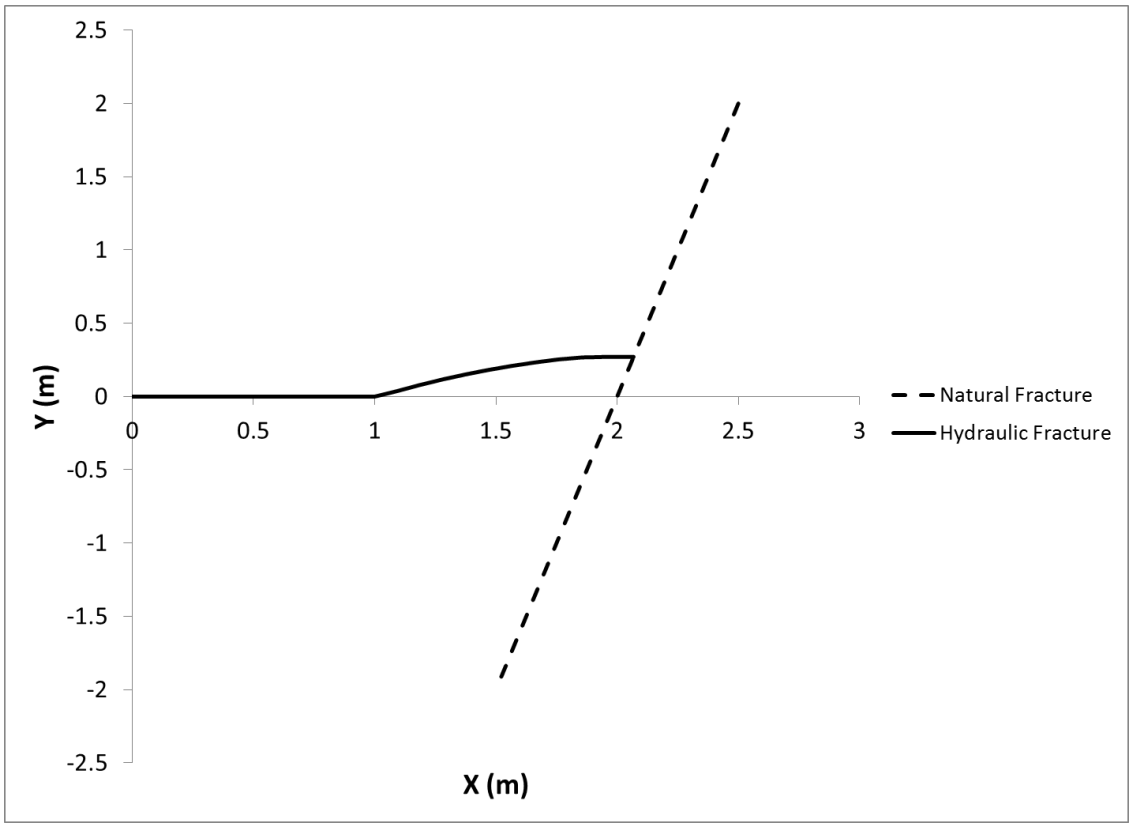

Fig 32. **Hydraulic fracture trajectory obtained for configuration shown in Fig. 29.**

Fig. 33 shows the injection pressure profile with time, the injection pressure continues to decrease as the hydraulic fracture propagates till the point of its intersection with the natural fracture. The injection pressure rises as the fluid is going in to natural fracture because of its smaller aperture, and the higher pressure needed to open the natural fracture from its closure. The value of the injection pressure reached after intersection with the natural fracture depends on the length of the natural fracture, closure stress acting on the natural fracture and its maximum closure allowed.

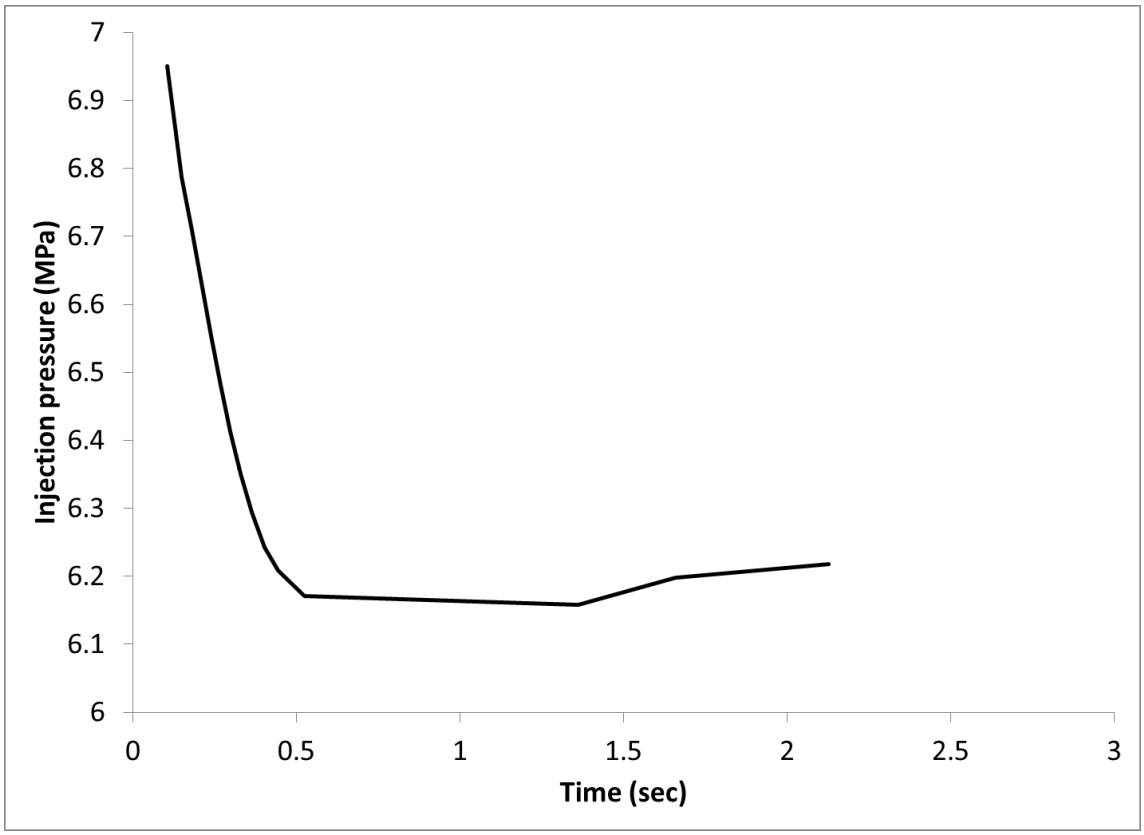

Fig 33. Variation of fluid pressure at injection point with time. The rise of injection pressure after intersection of hydraulic fracture and natural fracture is small compared to the Case 2 because of the large natural fracture considered in this case (the other factors that influence this are discussed below).

Fig. 34 shows the apertures of the hydraulic fracture at various times. We can see there is slight decrease in the fracture widths at length 1m because of the change in fracture trajectory at that point. The hydraulic fracture aperture continues to increase with time as the fracture propagates but when the fracture coalescence takes place the amount of the aperture increase is relatively higher because of the increase in injection pressure after coalescence.

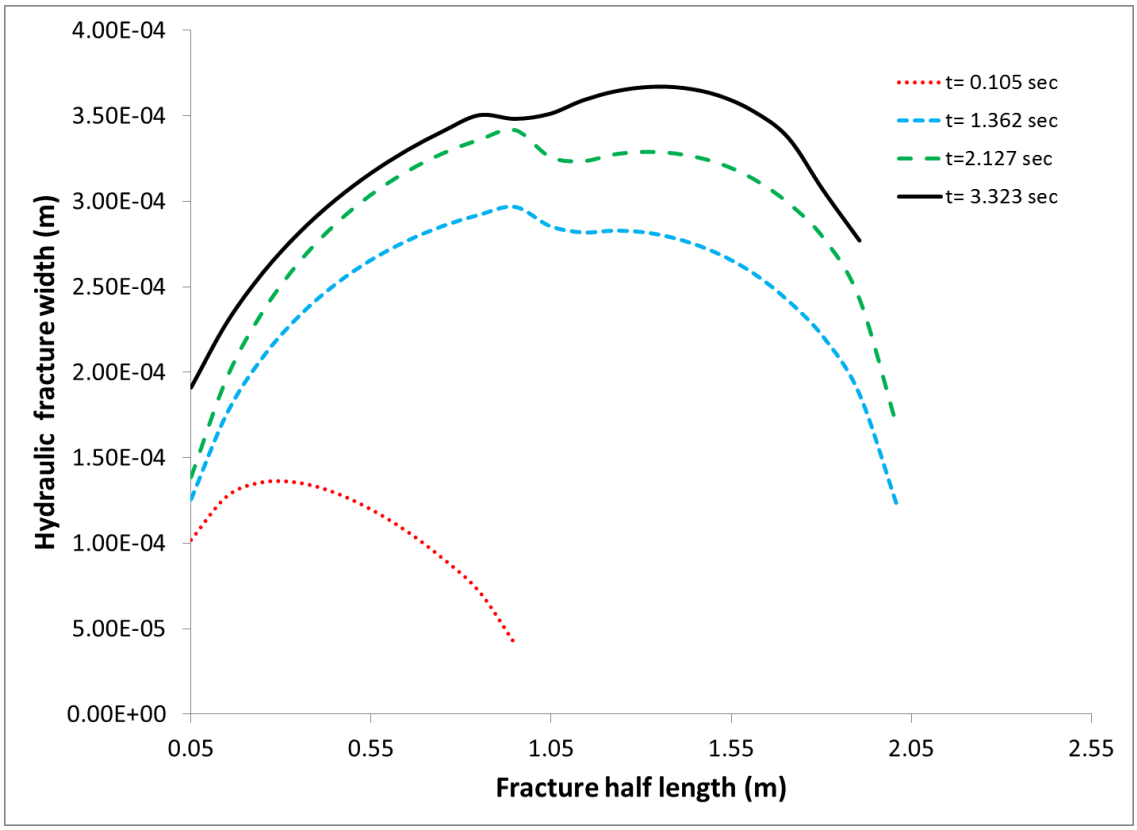

Fig 34. Hydraulic fracture opening profiles at various instants. A sudden decrease in the widths at 1 m is caused by the change in hydraulic fracture trajectory.

Initially the natural fracture is assumed to be supported by pore pressure and asperities. The initial width of natural fracture can be assumed to be equal to its hydraulic conductivity. As the fluid injection continued and natural fracture is pressurized, its width will increase with time, eventually transforming it to a hydraulic fracture. From Fig. 35 at time 1.362 sec we can see that the natural fracture has higher widths than its hydraulic aperture. For the inclined natural fracture considered above the top section of the natural fracture has a higher widths than the bottom section, this is due to the huge stress shadow on the lower section of the natural fracture. Similarly, the fluid pressures

in the bottom section are lower than the top section which is the less restrictive path for the fluid to enter. At time 2.12 sec the entire top section of the natural fracture is completely open and the bottom section of the natural fracture is only partially opened. This will likely lead the top section of the natural fracture to propagate as pressure increases. The lower widths in the bottom section of the natural fracture will act as a constriction to the proppant pumped in to the natural fracture as the fluid will continue to go in to the top section when it starts to propagate.

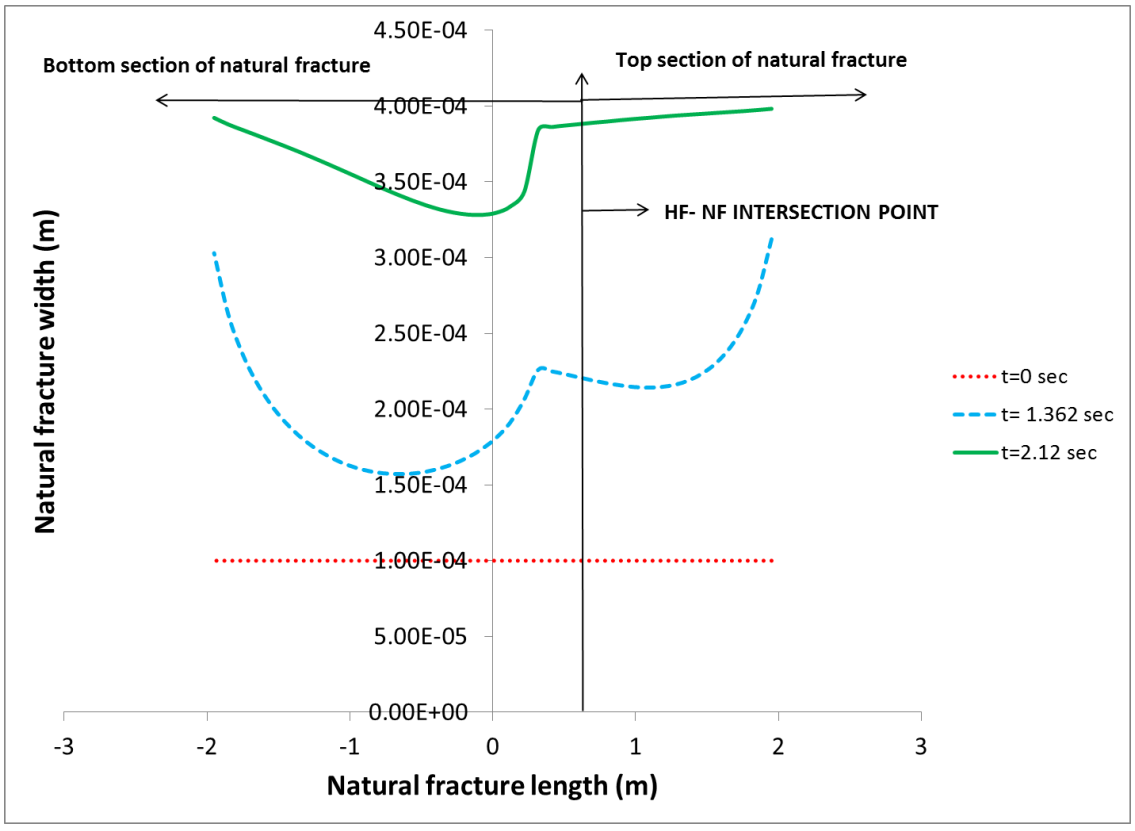

Fig 35. Natural fracture opening profiles at various instants. The widths of the top section of natural fracture are higher compared to lower section because of stress shadow on the lower section of natural fracture. The apertures at the end of top and bottom section of the natural fracture are equal because a joint with high closure at center and low closure at the tip is considered.

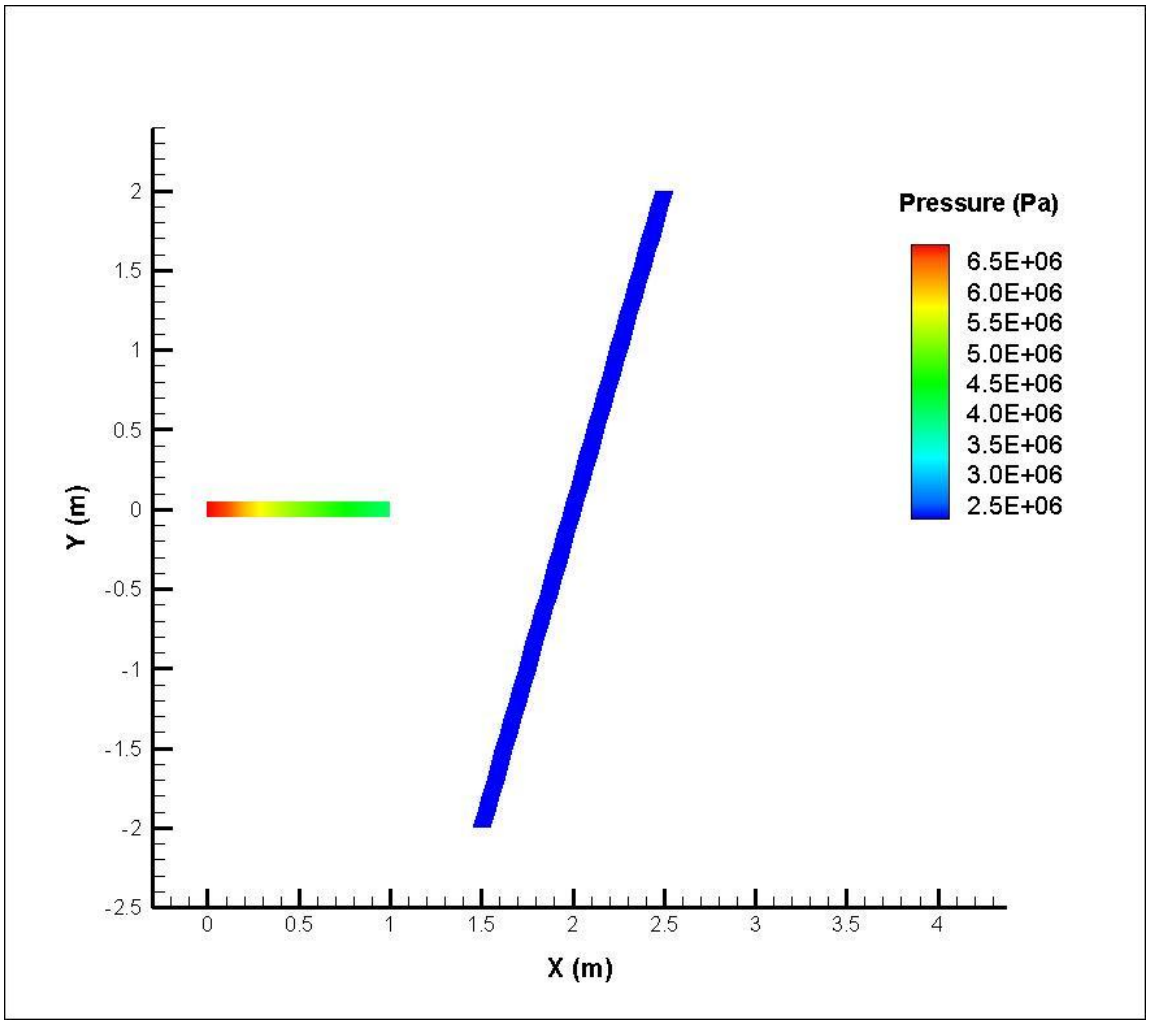

Fig 36. The initial state of hydraulic fracture and natural fracture for the configuration shown in Fig. 29. Initially pressure inside the natural fracture is assumed to be equal to the pore pressure in the formation which is 2.5MPa.

Figures 36, 37, 38, 39, 40 shows the fracture pressures and widths at various instants.

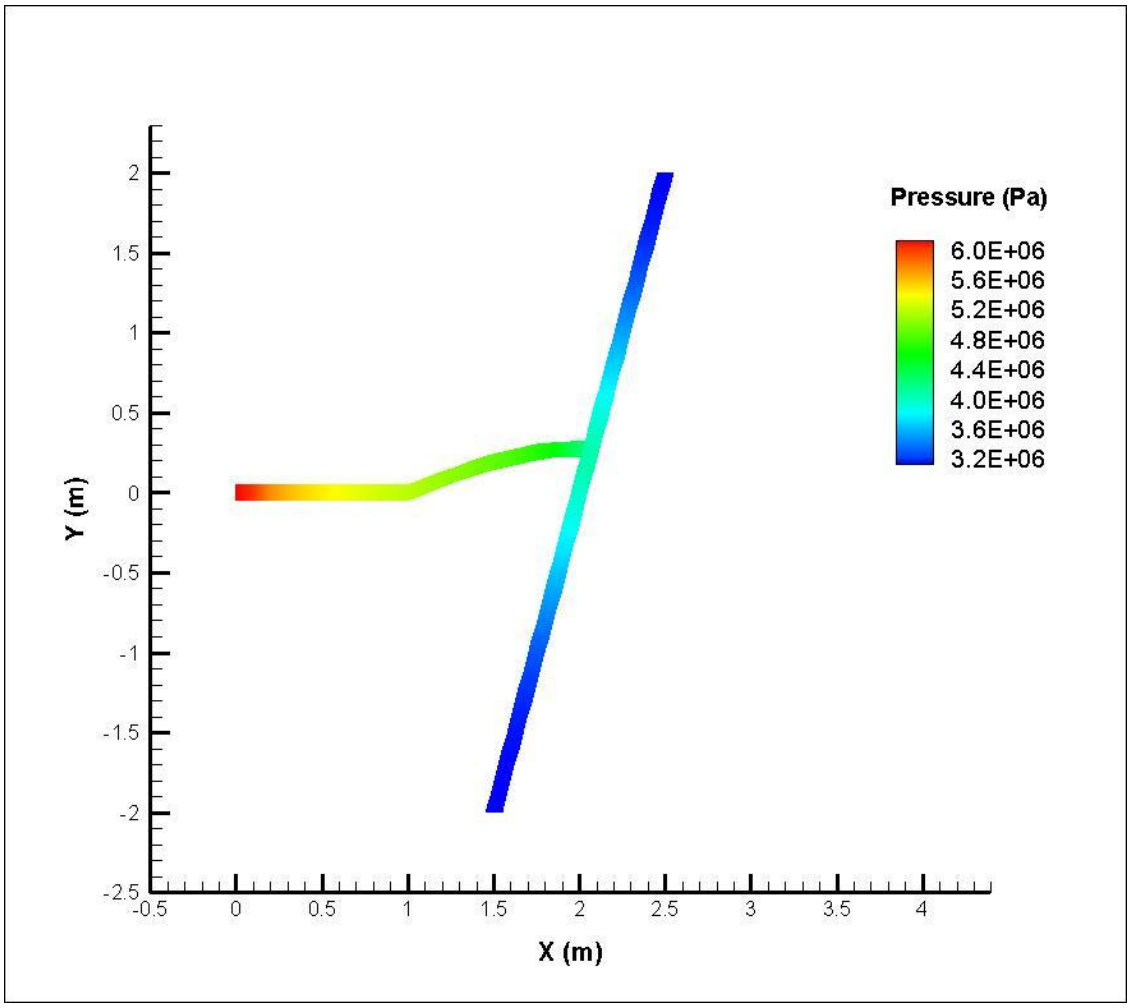

Fig 37. Fluid pressure distribution in the fracture network after HF-NF intersection at time 1.36 sec.

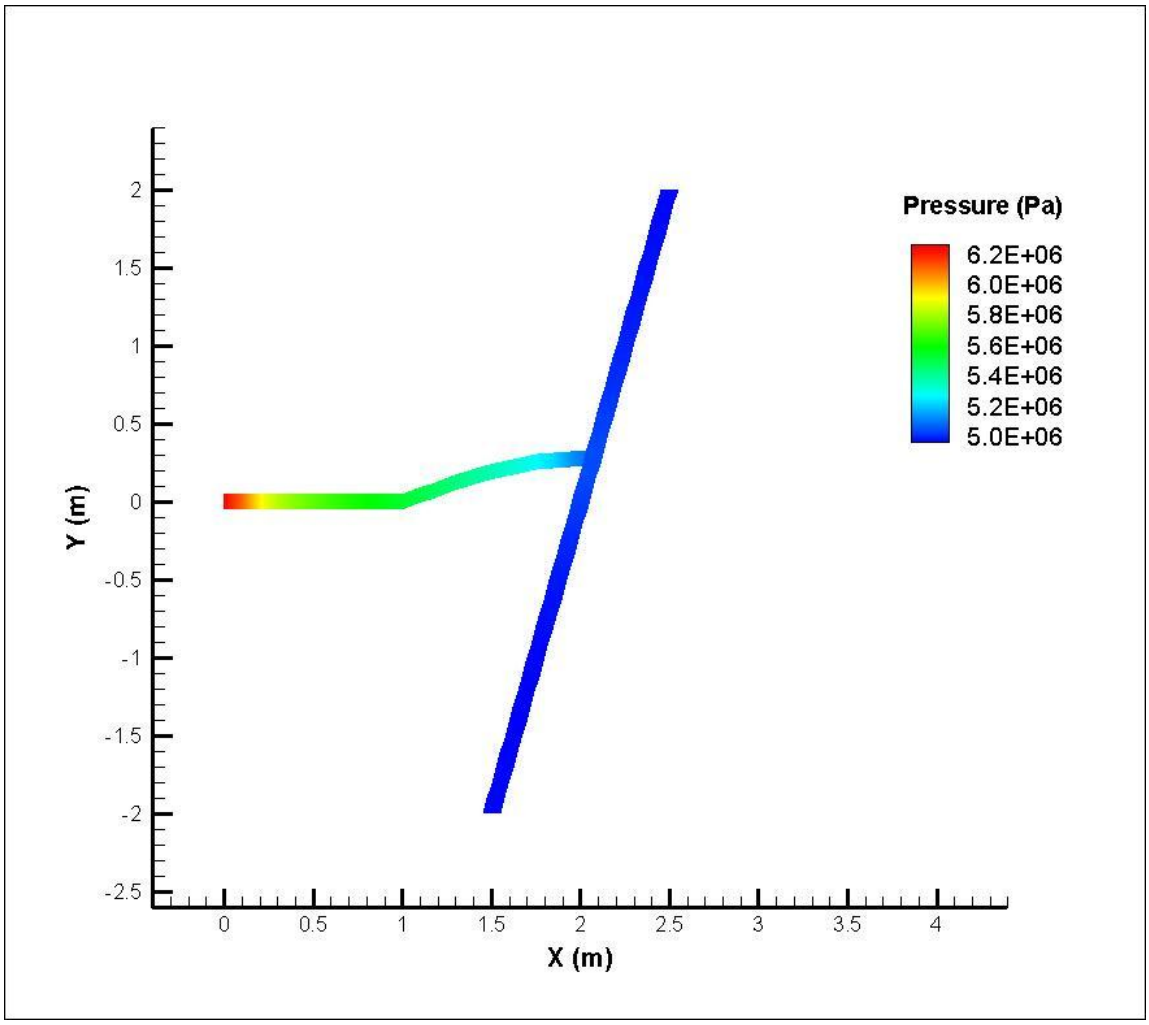

Fig 38. The fluid pressure distribution in the fracture network at time 2.12 sec. Though the pressures were high in the bottom section of the natural fracture, it is still closed mechanically due to stress shadow on bottom section. Thus, top section of the natural fracture will more likely propagate first with injection.

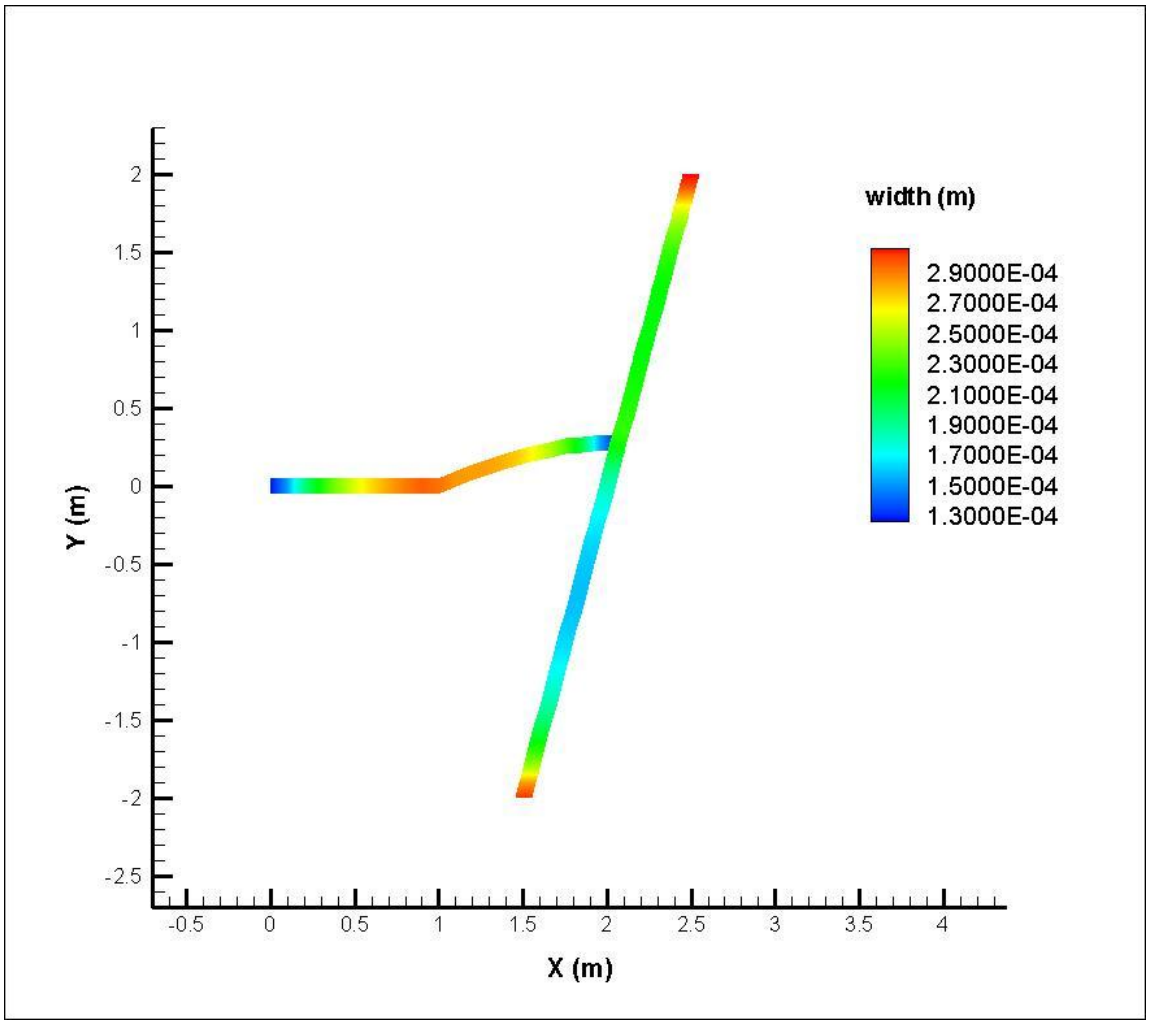

Fig 39. The width profile of HF-NF at time 1.36 sec. The Natural fracture started to open; the widths on the top section of natural fracture are higher than the bottom. As explained above the ends of the natural fractures are having high widths because of the assumption of non-uniform closure values along the natural fracture.

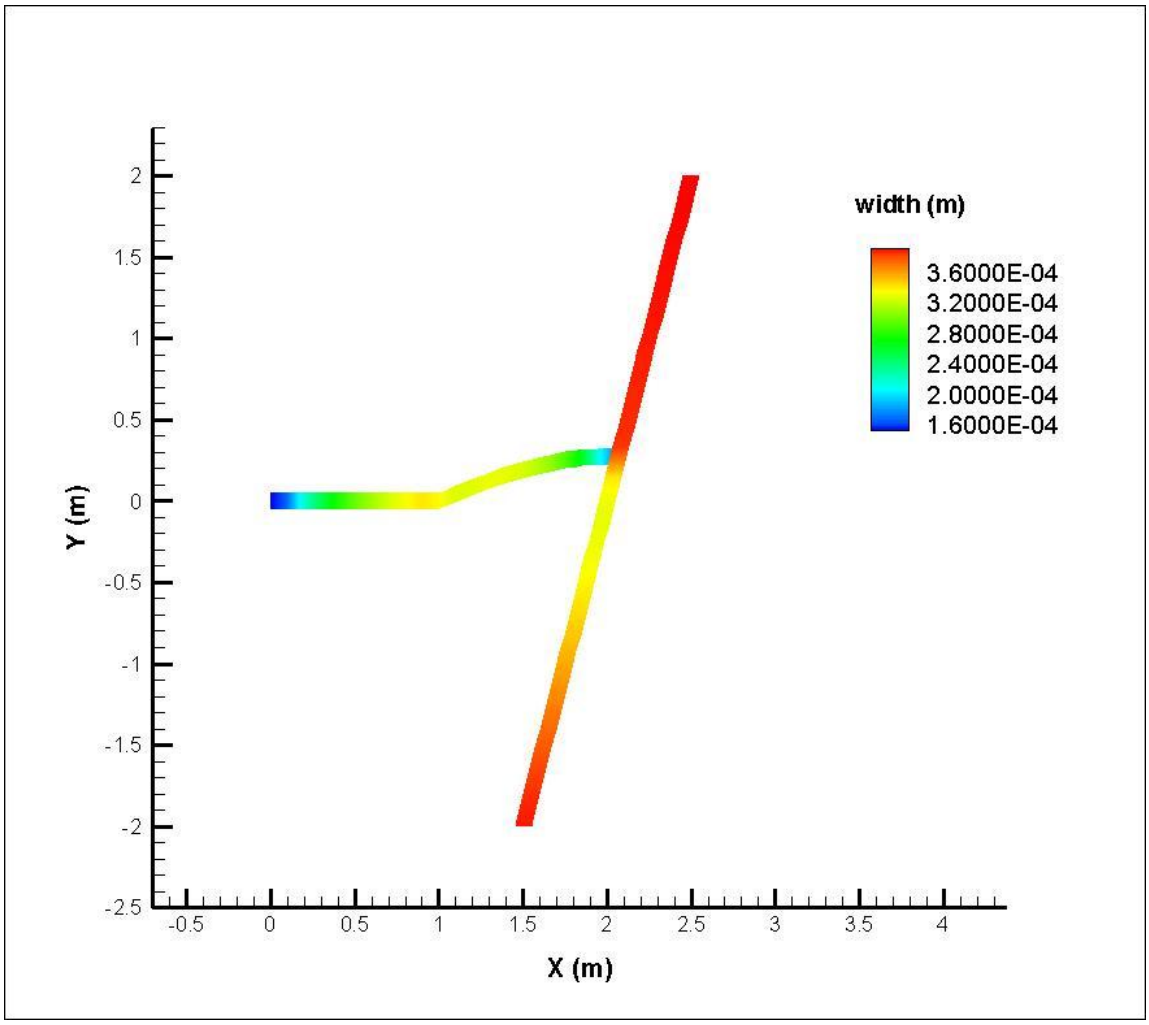

Fig 40. The width profile of HF-NF after 2.12 sec of injction. The top section of the natural fracture is completely opened whereas a portion of the bottom section is not, because of the stress shown on it. It is also seen that there is a reduction in width along the hydraulic fracture at the point where it changes trajectory. The yellow regions in the above figure are areas of potential proppant blockage sites. The widths of hydraulic fracture are lower than the natural fracture because in this model high initial closure value of 0.3 mm and a hydraulic aperture 0.1 mm is considered for the NF. When the natural fracture opens completely the initial closures is converted to width.

6.3 Propagation of Natural Fracture

6.3.1 Example-1

As an example, the geometry shown in Fig. 41 is considered. The rock and fluid properties used in the simulation are given in **Table 6**. The natural fracture is assumed to be in equilibrium with the stress state which means the natural fracture does not deformed due to the initial stresses. The hydraulic fracture is symmetrically placed relative to the natural fracture and is expected to propagate along its original direction until it joins the natural fracture.

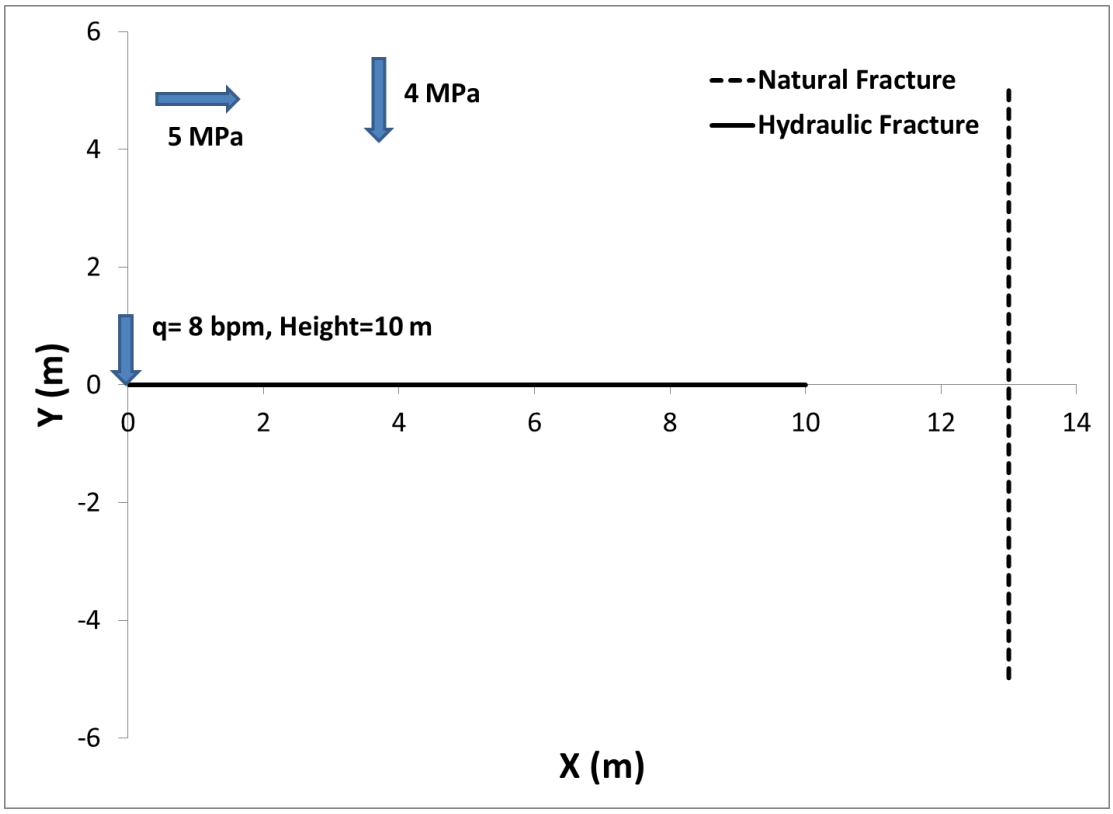

Fig 41. Geometry of HF and NF for Example 1 in section 6.3.

When the hydraulic fracture (HF) intersects the natural fracture (NF) and the latter opens, propagate will continue from the natural fracture as shown in Fig. 42 (fracture crossing and re-initiation from the surface of natural fracture are not given in this model at this time). We can see that the propagated wings from the natural fracture tend to align themselves with the maximum principal stress but because of the stress shadow between them, they deviate away from one another.

Table 6 Parameters used to simulate propagation of NF which is in equilibrium with in-situ stresses

Parameter	Value	Units
Injection rate (q_0)	8	bpm
Fluid viscosity (μ)	1	cP
Young's modulus (E)	27	GPa
Poisson's ratio (ν)	0.25	
(σ_H), (σ_h)	5, 4	MPa
Hydraulic aperture	0.1	mm
Height	10	m

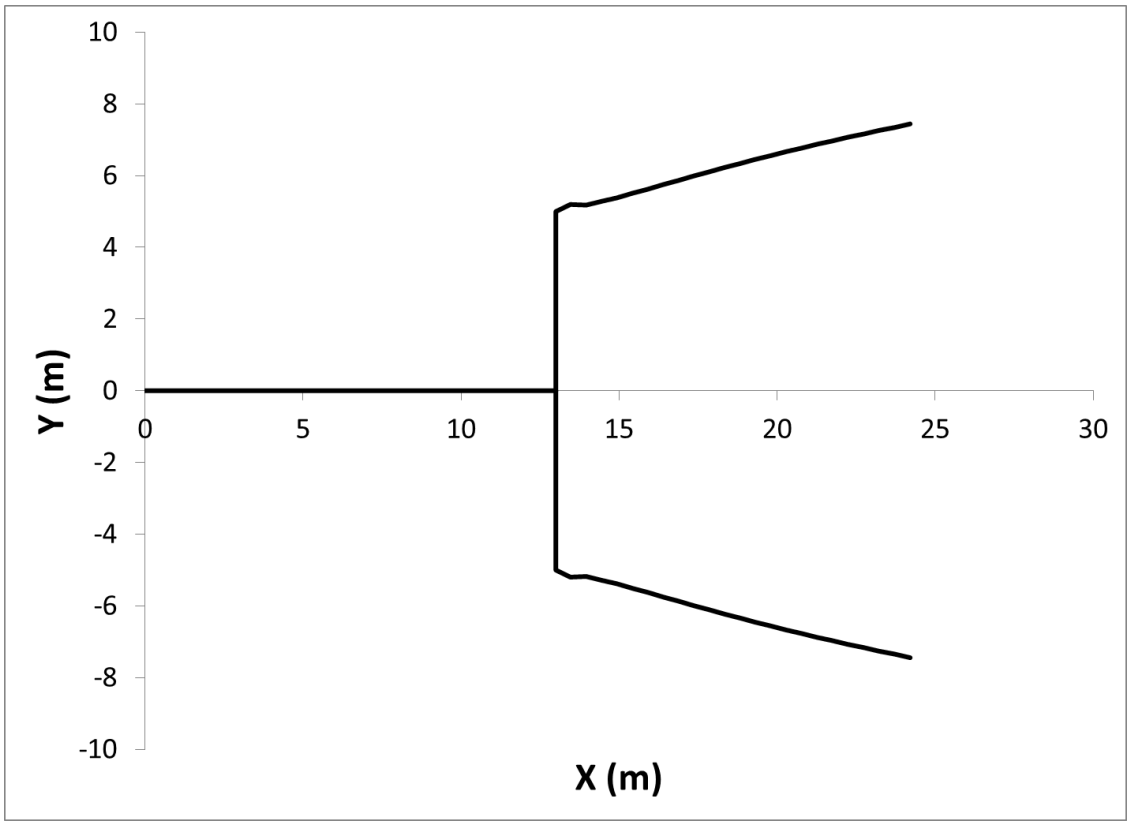

Fig 42. Fracture network at 30 sec. The propagated wings from NF are turning towards σ_H and moving farther from each other.

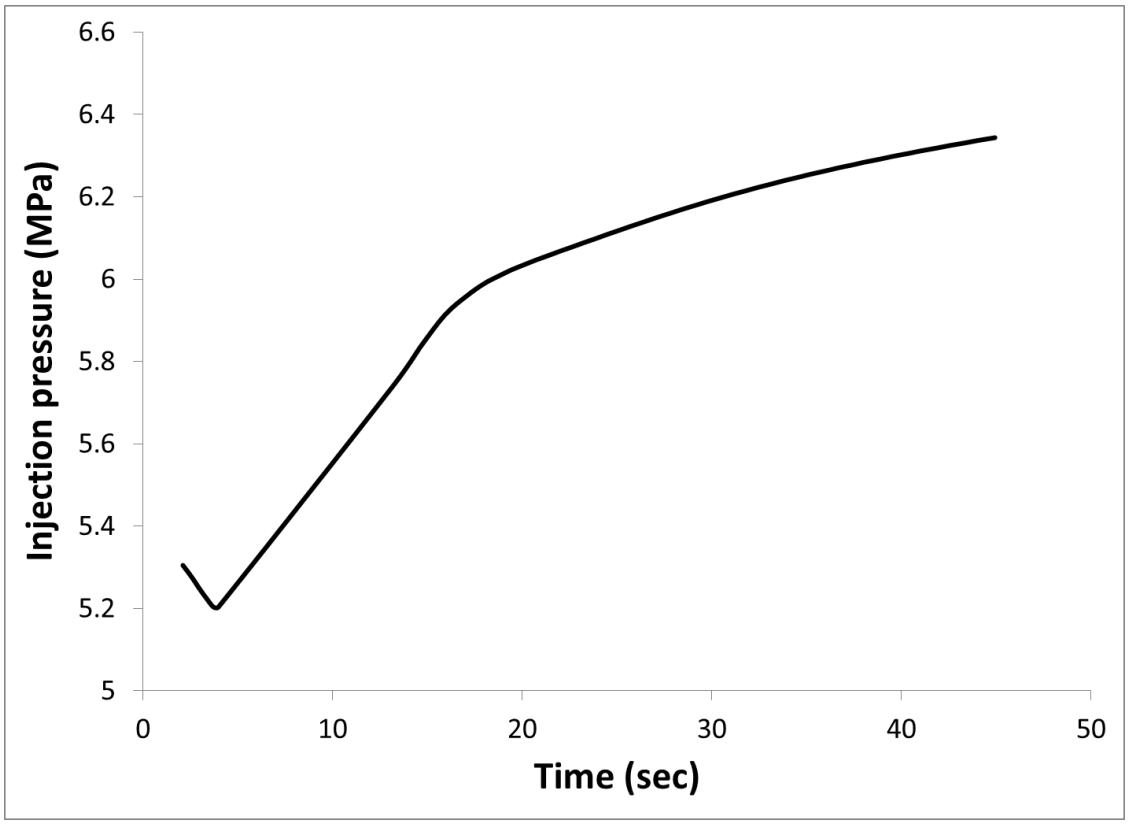

Fig 43. The injection pressure profile for Example 1. In this case, the injection pressure continues to increase after intersection.

Fig. 43 shows the injection pressure profile for the network shown in Fig. 42. The injection pressure is decreasing until the natural fracture is intersected with hydraulic fracture and then pressure starts to increase. This rise in injection pressure is to be expected as the two wings from the natural fracture mechanically interact because of their relatively small spacing and do not completely align in the direction of maximum principal stress.

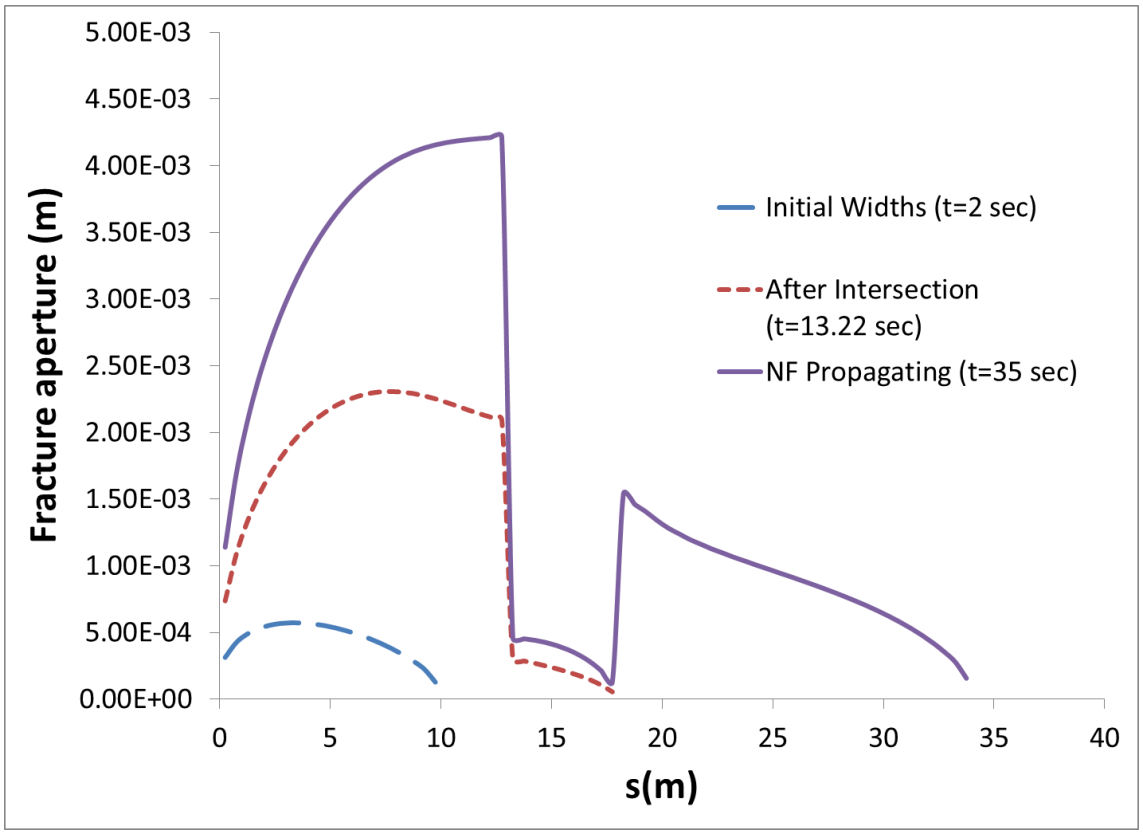

Fig 44. Fracture width profile at various instants. s=13-18m experience low widths as it has to open against high closure stress.

Fig. 44 shows the width profile for the network shown in Fig. 43. For s= (0-13m) the curve shows the widths of the hydraulic fracture while s= (13-18m) shows the widths of the lower wing of the natural fracture. From s=18m onward, it shows the widths of propagated lower wing of natural fracture. The huge reduction in widths over s=13-18m occurred because the fracture has to open against σ_H.

6.3.2 Example-2

The geometry shown in Fig. 45 is considered for this case. The rock and fluid properties used for this simulation are given in **Table 6**.

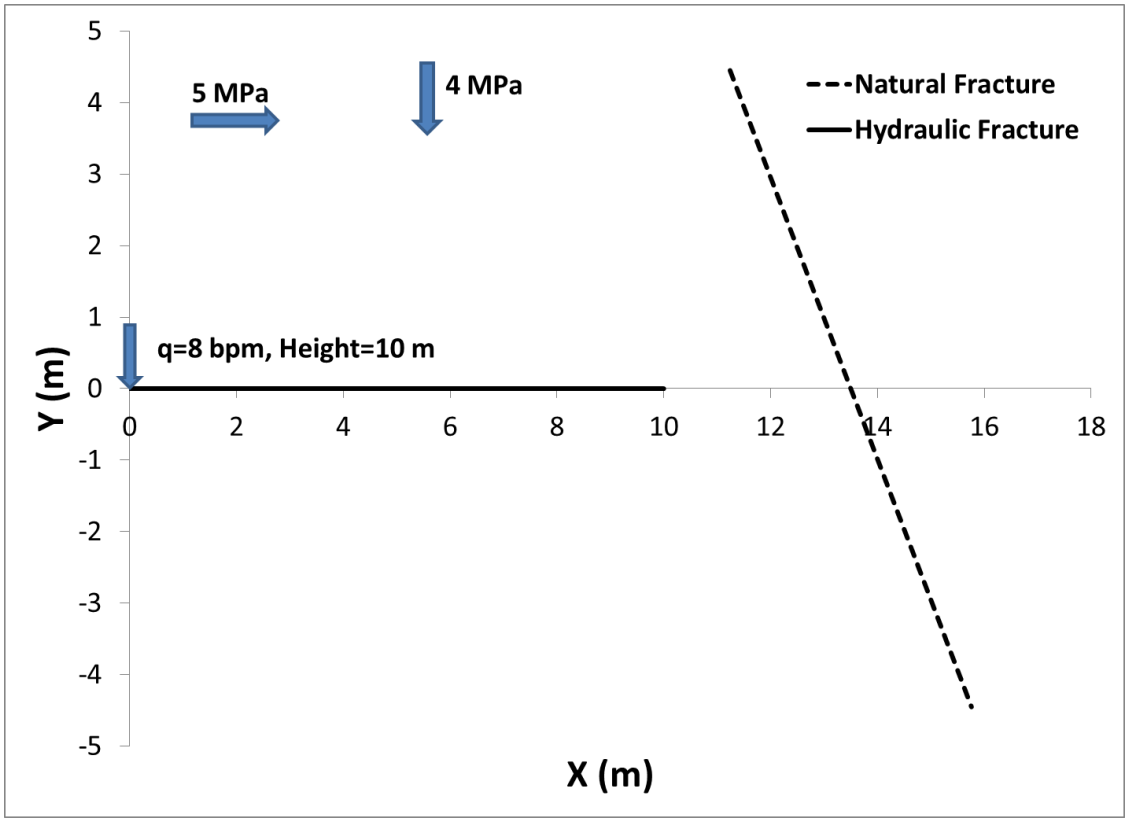

Fig 45. Geometry of HF and NF considered for Example 2.

Since the natural fracture is in equilibrium state (there is no stress redistribution near natural fracture due to initial in-situ stresses) the hydraulic fracture is expected to propagate along its axis (though the tensile stresses created at the hydraulic fracture tip

may cause some opening in the natural fracture, the stress shadow it causes is not significant enough to change the path of the HF). After the hydraulic fracture intersects the natural fracture, the fluid is diverted into the lower part of natural fracture. This is because of the high stress shadow acting on the top part of natural fracture due to hydraulic fracture, hindering its opening. The bottom part of the natural fracture continues to propagate orienting itself towards σ_H (Fig. 46).

Fig. 47 shows the injection pressure profile for this case. The injection pressure is decreasing as the hydraulic fracture propagates. But it rises when the hydraulic fracture tip nears the NF due to stress shadow between them. Then, the pressure decreases when the HF intersects the NF and a larger volume is available. Finally, the pressure starts to increase as the lower wing of NF propagates, eventually developing a decreasing trend as the lower wing of NF is aligned with the σ_H.

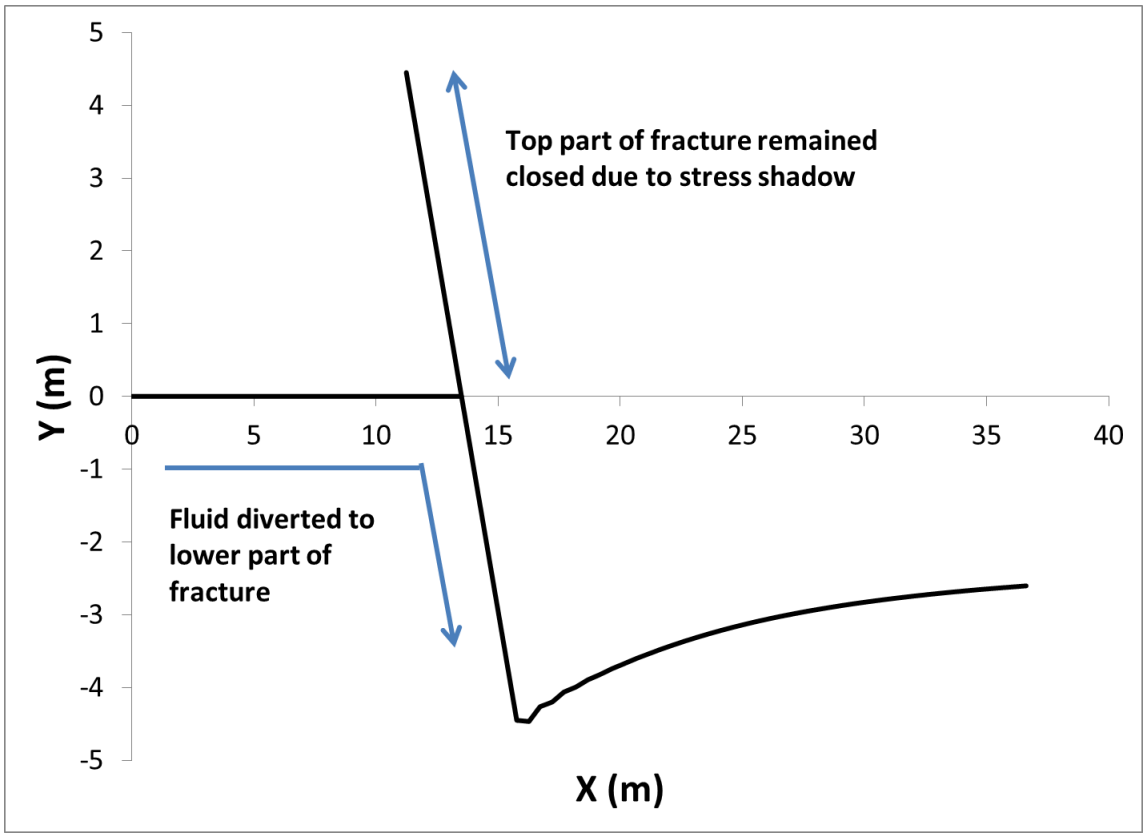

Fig 46. Fracture network of Example 2 after 30 sec. The fluid is diverted to the lower part of the NF as the top part is not opened due to high stress shadow between HF and top part of NF.

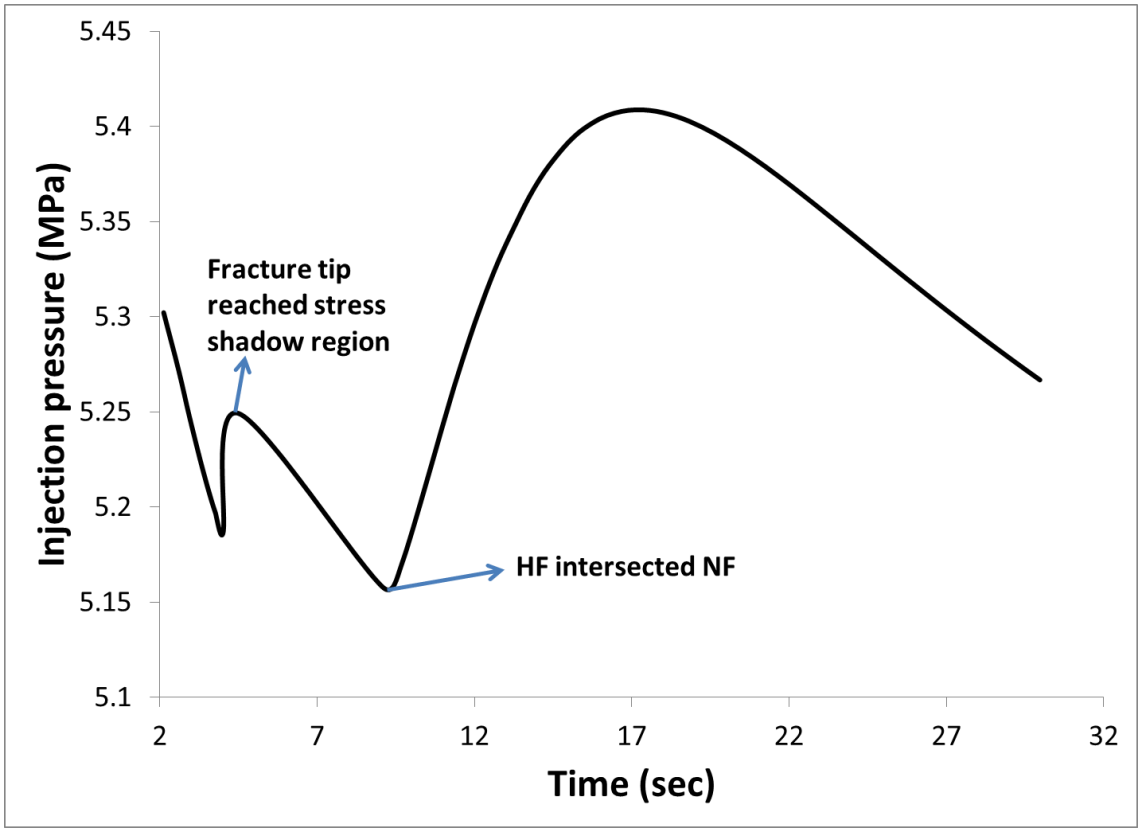

Fig 47. Injection pressure profile for Example 2. Injection pressure begins to increase after HF, NF intersection and later decreases as the fracture is aligning in σ_H-direction.

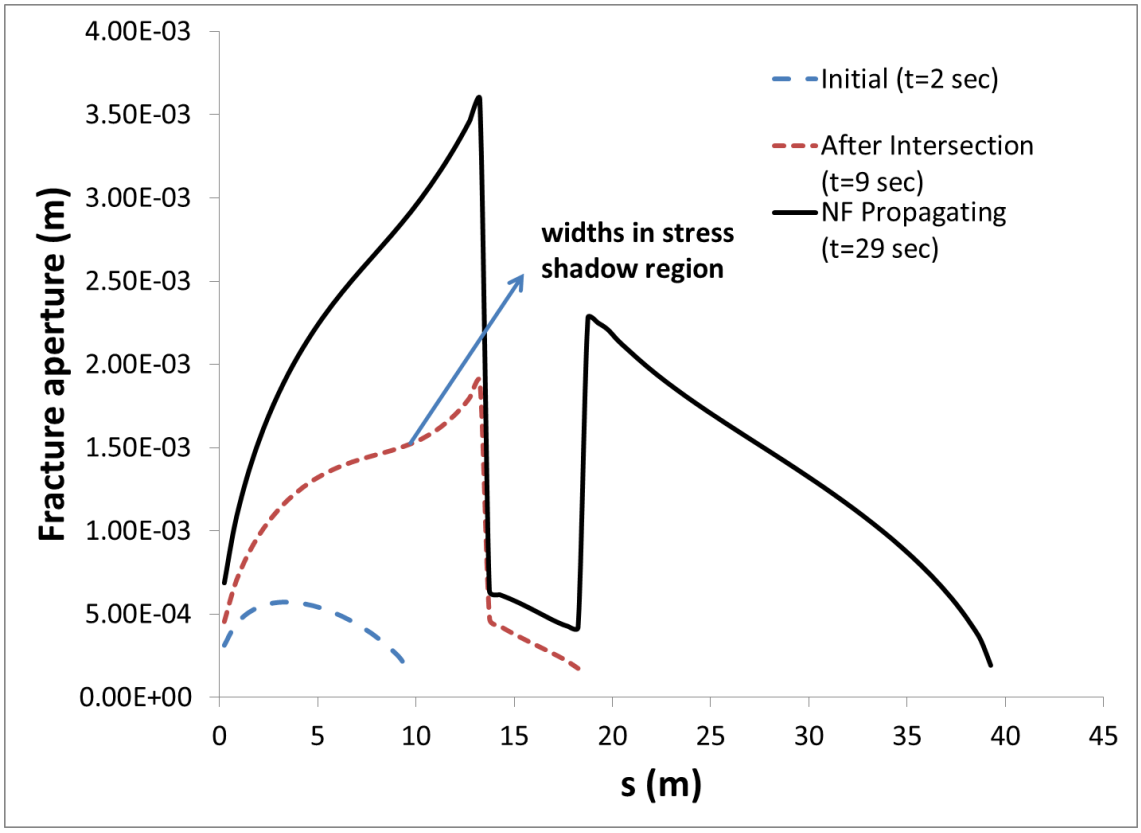

Fig 48. Width profile for Example 2. The profile is almost similar to Fig. 44 except at the end of HF where a slight decrease in width occurs due to the stress shadow.

Fig. 48 shows the widths of fracture network shown in Fig. 46. For s= (0-13m), (13-40), the profile corresponds to that of the HF and NF (lower part), respectively (note the top part of natural fracture is not opened due to stress shadow over it). The width profile is almost similar to what was observed in Example-1 except at the end of HF, where there is a slight reduction in widths due to stress shadow over it.

6.3.3 Effect of distance between HF and NF on injection pressure after their intersection

The example simulation in Section 6.2 and 6.3 showed that after HF intersects a NF, the injection pressure increases to open and propagate the natural fracture. The magnitude of the injection pressure increase is different for each case and, as discussed in Section 6.2, it depends on distance between HF and NF ,viscosity of the fluid injected as well as the closure stress acting on the NF. In this section the effect of viscosity and distance between the fractures on injection pressure after intersection is studied. To study this effect, a sensitivity analysis is carried out using the parameters in **Table 7**. The configuration shown in Fig. 49 is considered. The viscosity and the distance between HF and NF are changed in to see the variation in injection pressure behavior.

Table 7 Input parameters used to simulate HF-NF for section 6.3.3

Parameter	Value	Units
Injection rate (q_0)	0.5	bpm
Fluid viscosity (μ)	1, 100	cP
Young's modulus (E)	27	GPa
Poisson's ratio (ν)	0.25	
(σ_H), (σ_h)	5, 4	MPa
Height	10	M

Table 7 Continued

Parameter	Value	Units
Angle of intersection between HF and NF	90	degrees

The configuration shown in Fig. 49 is considered. The viscosity and the distance between HF and NF are changed in to see the variation in injection pressure behavior.

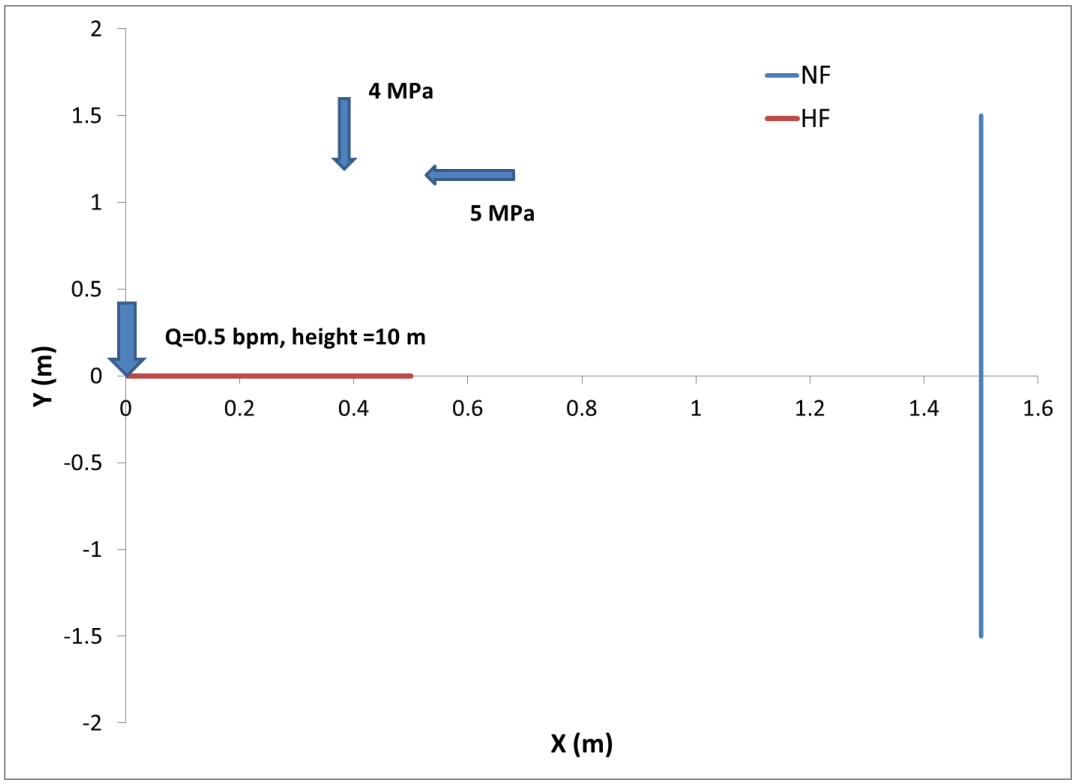

Fig 49. Geometry considered for HF-NF orthogonal intersection.

Table 8 Results obtained from simulation using low viscosity fluid

Distance from injection point to HF-NF intersection point in **m**	Viscosity of the fluid in **cp**	Injection pressure reached before intersection in **MPa**	Peak injection pressure reached after intersection in **MPa**	Change occurred in Injection pressure in **MPa**	Change in injection pressure after intersection(nature)	Time to fill the natural fracture in **sec**
1.0	1.0	5.56	6.01	0.446	increased	3.76
1.5	1.0	5.45	5.93	0.473	increased	5.24
2	1.0	5.36	5.84	0.479	increased	6.82
2.5	1.0	5.28	5.77	0.479	increased	8.64
3.0	1.0	5.22	5.70	0.478	increased	10.66

Table 9 Results obtained from simulation using high viscosity fluid

Distance from injection point to HF-NF intersection point in **m**	Viscosity of the fluid in **cp**	Injection pressure reached before intersection in **MPa**	Peak injection pressure reached after intersection in **MPa**	Change occurred in Injection pressure in **MPa**	Change in injection pressure after intersection(nature)	Time to fill the natural fracture in **sec**
1.0	100.0	8.94	8.63	0.316	decreased	7.83
1.5	100.0	8.60	8.32	0.282	decreased	9.45
2	100.0	8.31	8.07	0.241	decreased	11.32
3.0	100.0	7.87	7.69	0.186	decreased	15.44

From **Tables 8& 9** we can see that for low viscosity fluid, the injection pressure is increasing after HF intersected NF (i.e. while opening of NF). With the increase in distance between NF and HF, the magnitude of injection pressure at intersection point is decreasing, but the amount of increase in injection pressure from before intersection to after intersection is increasing. In the case of higher viscosity fluid, the injection pressure

is decreasing after HF intersected NF; also the amount of decrease in injection pressure is decreasing with increase in distances between the NF and HF fractures. This change in behavior of low viscosity fluid and high viscosity fluid can be explained from Figures 50 and 51.

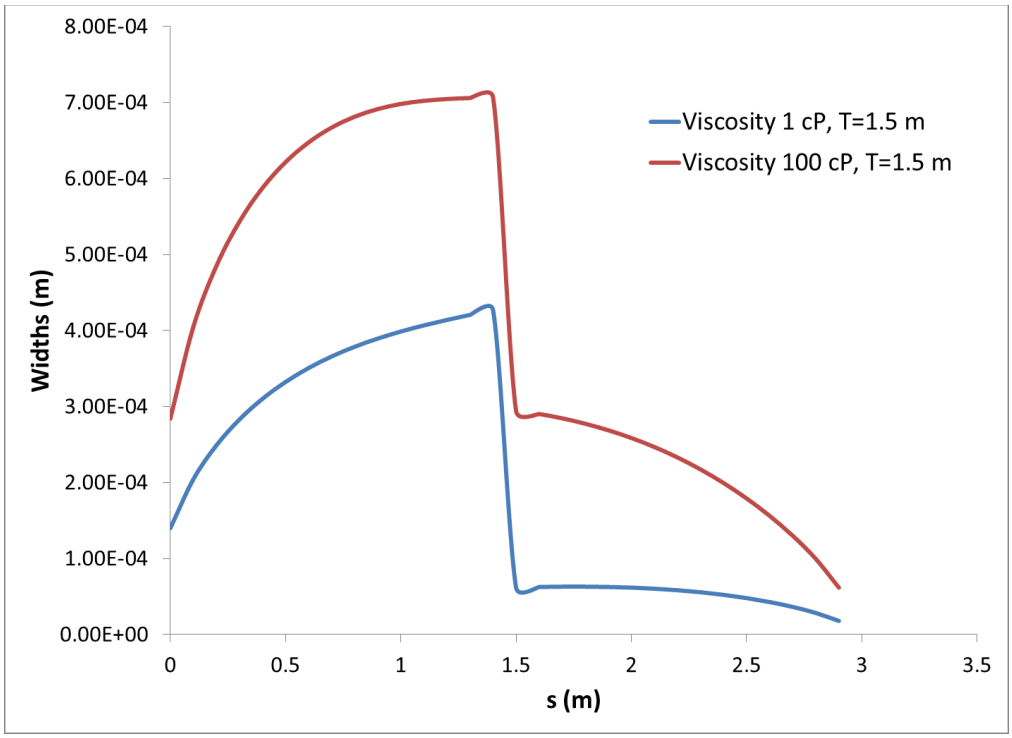

Fig 50. Fracture widths obtained for fluids with different viscosities.

Fig. 50 shows the widths along HF and half-length of NF (HF=s (0-1.5m), NF=s (1.5-3m) for viscosities 1 and 100 cP. T is the distance between the injection point in HF and intersection point of NF and HF. The widths of HF and NF for higher viscosity fluid are much more than those obtained for lower viscosity fluid due to higher pressure generated

from higher frictional fluid. Hence in the case of higher viscosity fluid large volume of fluid is present in HF before intersection to fill up the natural fracture, this results in the pressure decrease after intersection. We can also observe from tables that the higher injection pressure for lower T's is helping the fluid to fill the NF fast, also with increase in viscosity the time taking to fill the NF is increasing.

For larger T, the time taken to fill up the natural fracture is more which means that the natural fracture is accommodating at a slower rate than the fluid injection into HF, as result the amount of increase in injection pressure from before intersection to after intersection is increasing with T increasing. This is also evident from the widths along the NF for larger T's are lower than those obtained for smaller T (Fig. 51). Thus, the competition between the injection rate, the ease at which the HF is accommodating the fluid and the rate of fluid movement in to the NF affects the injection pressure after intersection.

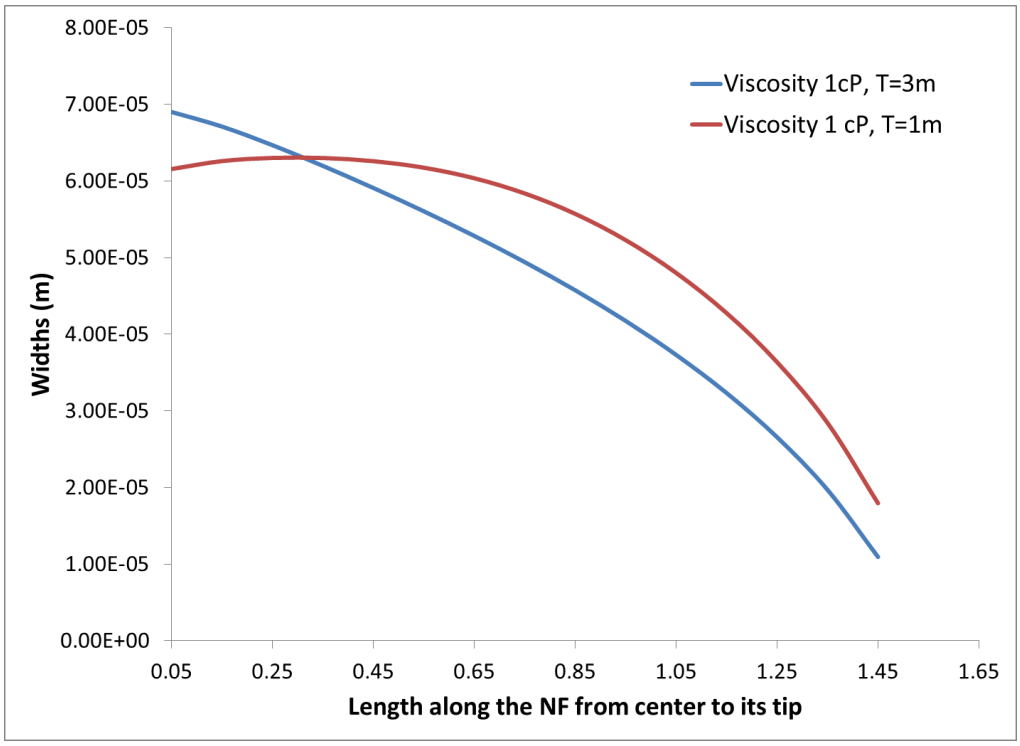

Fig 51. Fracture widths obtained for different T's.

6.4 Multiple Natural Fractures

6.4.1 Example-3

In this section the propagation of hydraulic fracture in a formation consisting of more than one natural fracture is studied by considering the configuration shown in the Fig. 52. Natural fractures NF1 and NF2 are in equilibrium with in-situ stresses and are each 5 m long and 6.25 m apart. The input parameters for this simulation are given in the **Table 10**.

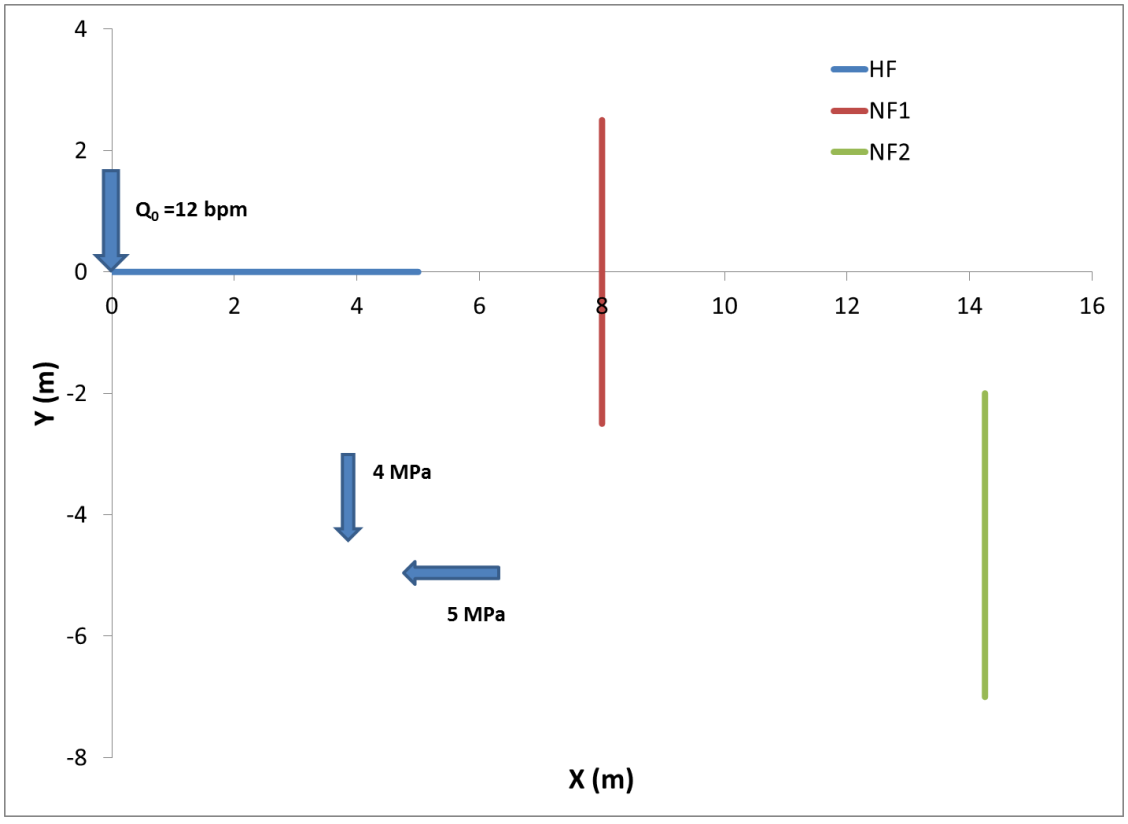

Fig 52. Geometry of Hydraulic fracture and Natural fractures considered for Example 3 in section 6.4.

The fracture network obtained after 12 sec is shown in Fig. 53. After HF intersects NF1, both top and bottom parts of NF1 are allowed to propagate as, HF is in symmetric with NF1. After some time the bottom part of NF1 intersects NF2 and fluid is diverted into the bottom part of NF2 as top part is not opened due to the stress shadow acting over it, similar to the Example 2 shown in section 6.3.

Table 10 Input parameters used to simulate HF-NF for section 6.4.1

Parameter	Value	Units
Injection rate (q_0)	12	bpm
Fluid viscosity (μ)	1	cP
Young's modulus (E)	27	GPa
Poisson's ratio (ν)	0.25	
(σ_H), (σ_h)	5, 4	MPa
Hydraulic aperture	0.01	mm
Height	10	m

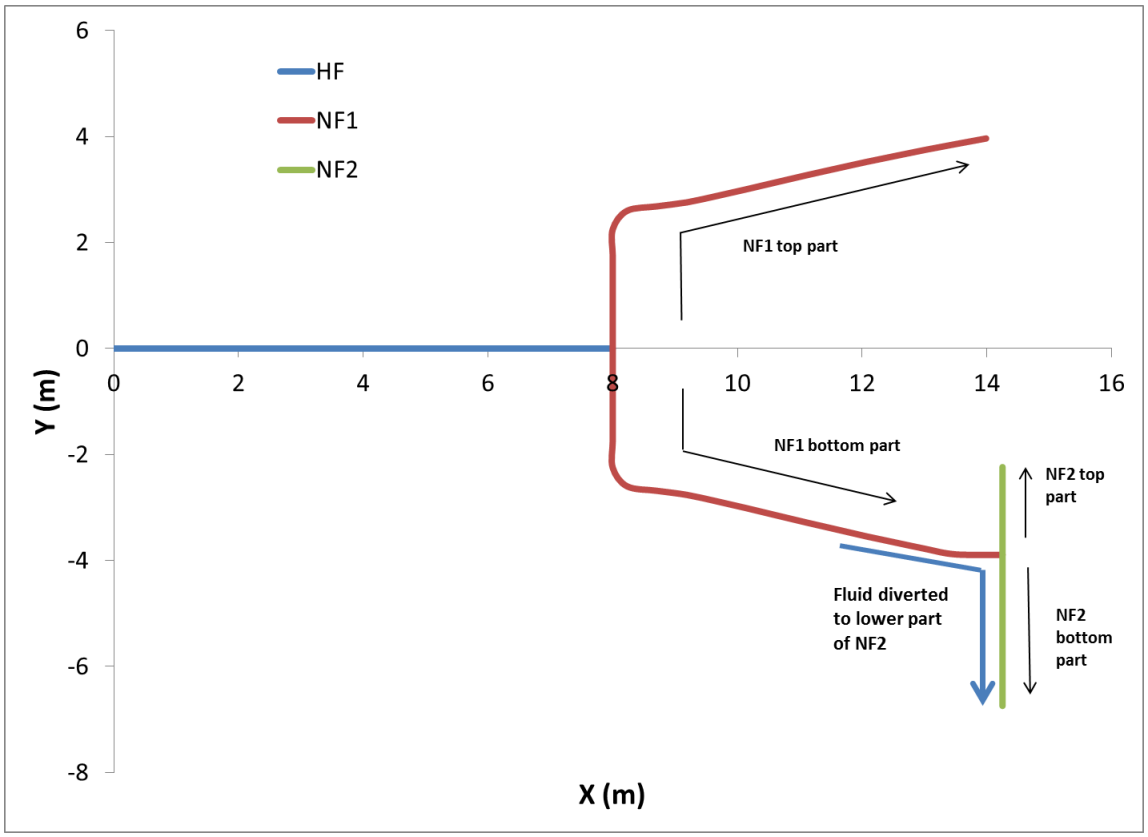

Fig 53. Fracture network obtained at 12sec. The top part of NF2 is not opened due to stress shadow over it.

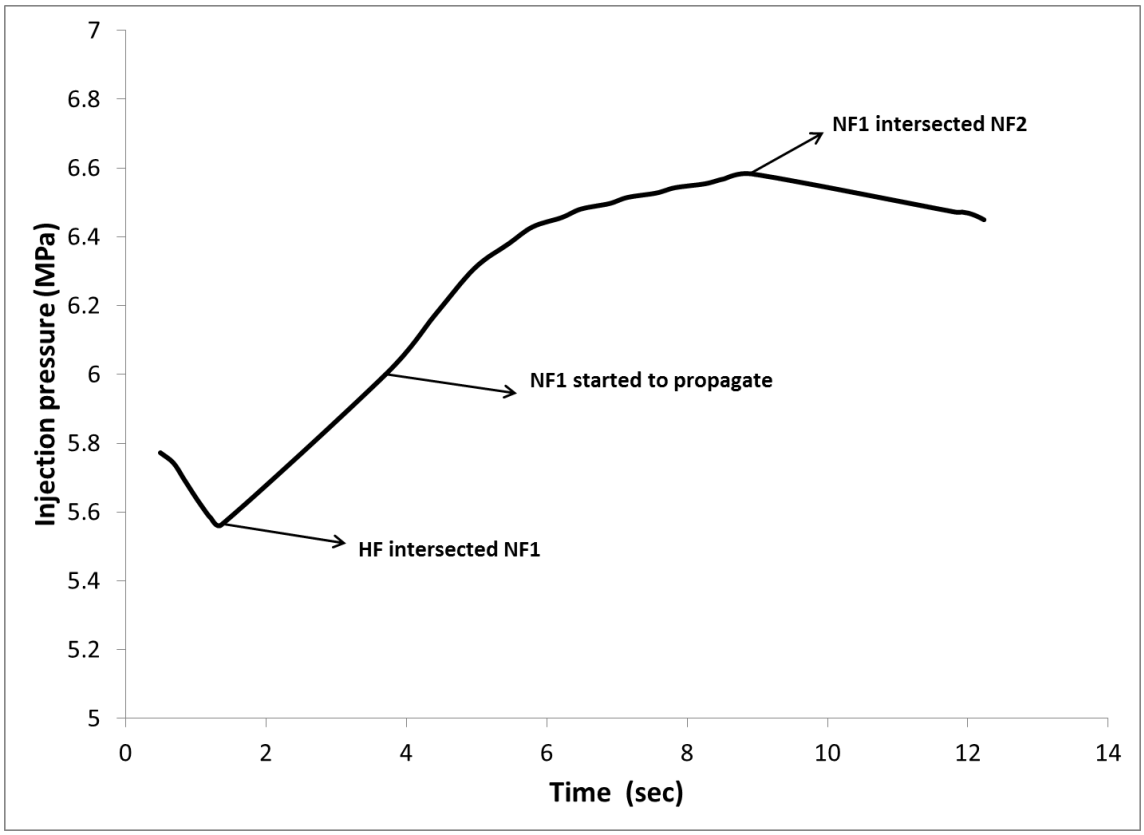

Fig 54. Injection pressure profile obtained for configuration shown in Fig. 52. The injection pressure decreasing till HF intersect NF1, then increases to open NF1 against high closure stresses, and decreases again after NF1 intersect NF2.

The injection pressure profile (Fig. 54) obtained in this simulation is similar to the profile observed for Example 1 in section 7.1 till NF1 intersected NF2. The injection pressure started to decrease after the intersection of NF1 and NF2, this behavior can be explained from the Figures 55 and 56, where we can see that large of fluid is present in both HF and NF1, before intersection, and can also due to the rate of fluid filling into the NF2 is greater than injection rate (see section 6.3.3).

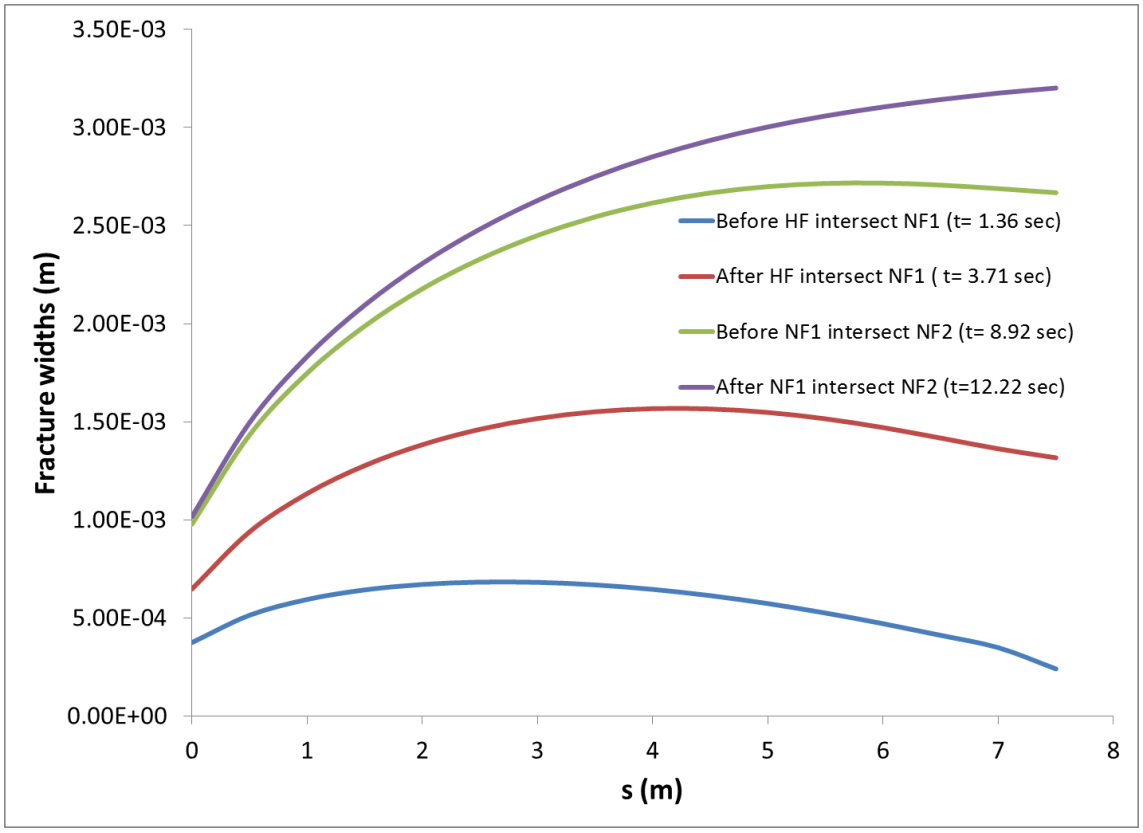

Fig 55. The widths along the HF. s=0m (injection point), s=7.5m (HF end).

The width profile of HF at various instants from Fig. 55 shows the, HF widths kept increasing with time, but it is interesting to note that the maximum opening location in the HF occurred somewhere in between it till NF1 intersects NF2, where their intersection, the maximum opening has occurred at the end of HF.

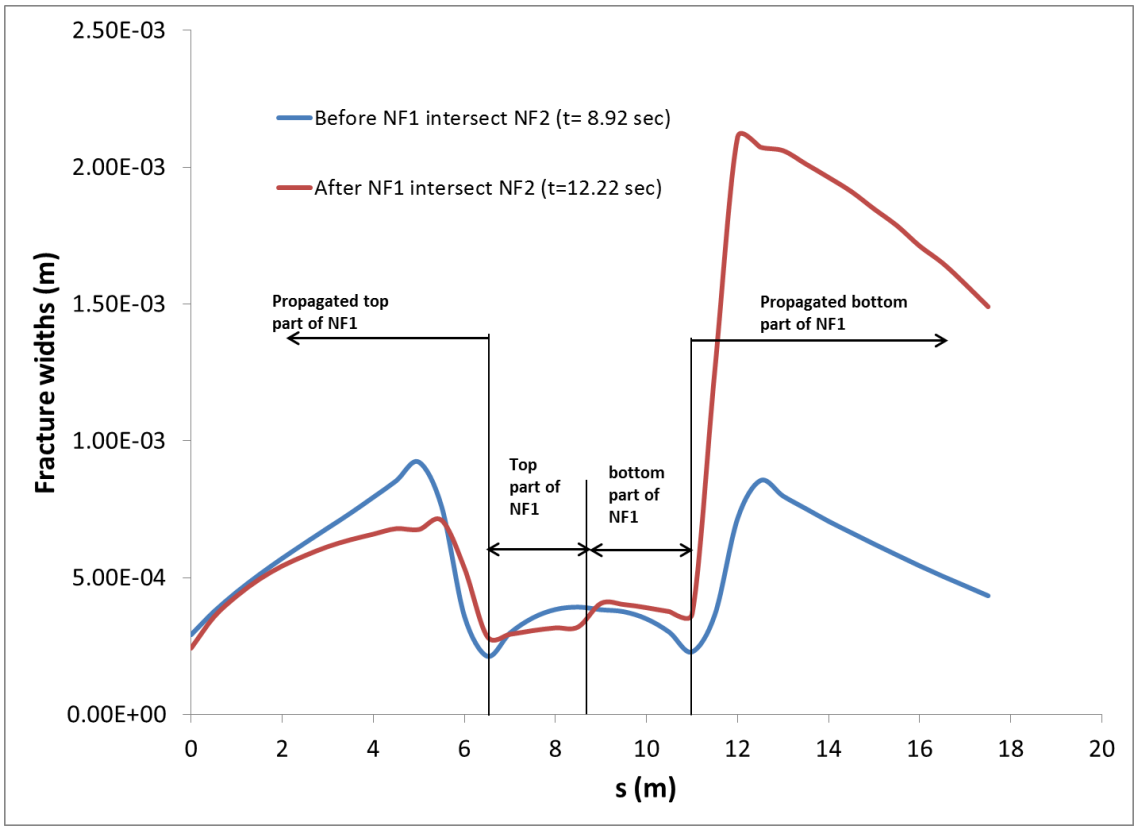

Fig 56. Shows the width profile of NF1 before and after it intersects NF2.

From Fig. 56 we can see that the widths along the top and bottom part of NF1 (s=6.5-11.5m) has less than widths of propagated parts of NF1, because the section (s=6.5-11.5 m) has to open against the higher closure stress (as that section is orthogonal to maximum principal stress). Even before NF1 intersects NF2 the widths near the tip of propagated bottom part of NF2 (s=16-18m) are higher than the widths near the tip of propagated top part of NF1 (S=0-2m). This is because when the bottom tip of NF1 is approaching toward NF2, there is some shearing action on NF2 which is making the bottom tip of NF1 open more than the tip of the top part of NF1. After the intersection of

NF1 and NF2, the bottom part of NF1 gained huge widths due to high pressures occurred along bottom part of NF1 to open NF2 (Fig. 57), whereas the widths along top part of NF1 has decreased even though the pressure along it has increased (Fig. 57) due to the stress shadow on from the bottom part of NF1.

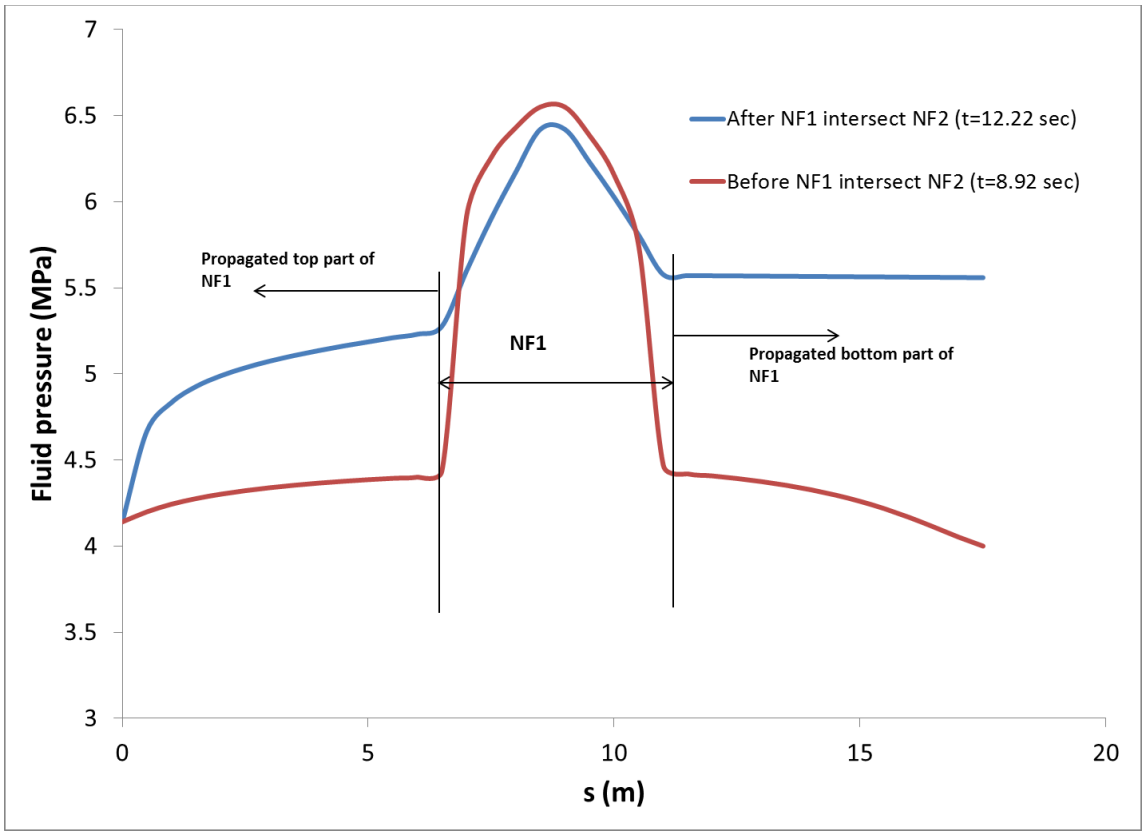

Fig 57. Shows the fluid pressure profile along NF1 before and after it intersects NF2.

From the Fig. 58 we can see that the top part of NF2 remained closed due to the stress shadow over it from NF1, thus the fluid is diverted into the bottom part of NF2 and opened it.

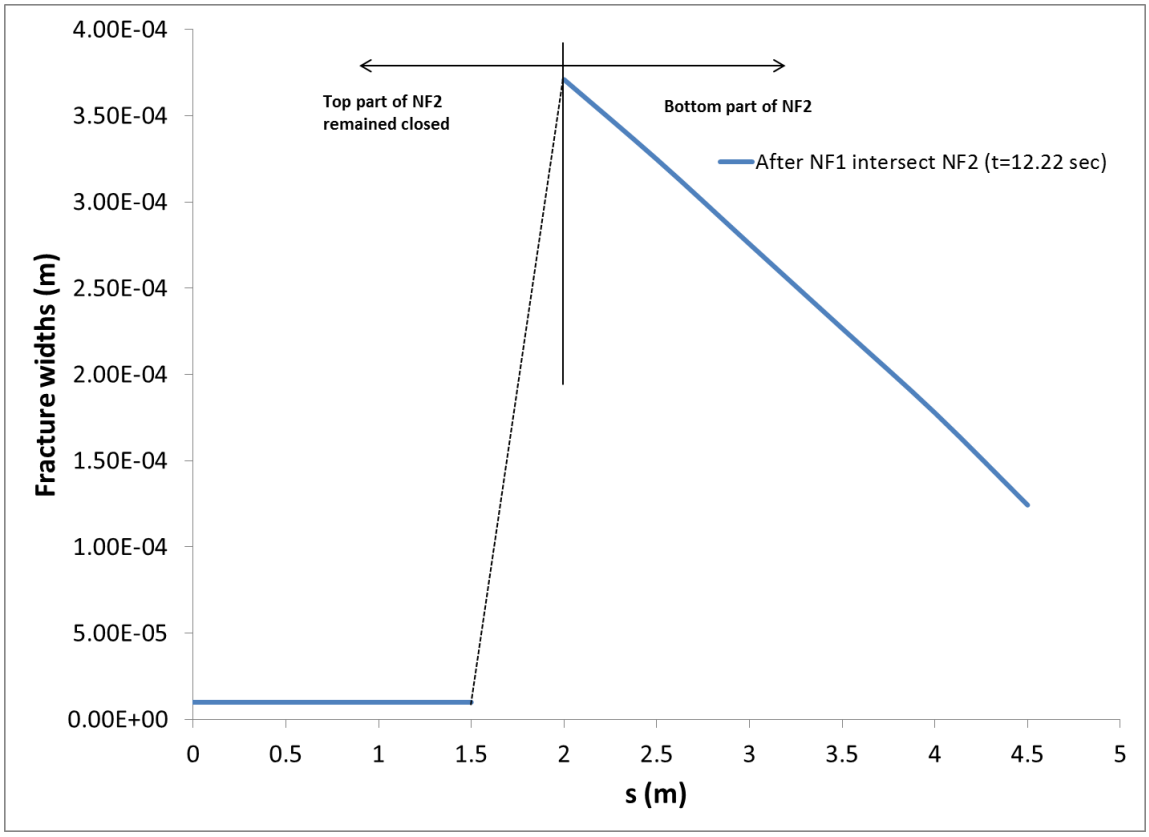

Fig 58. Shows the width profile of NF2 after NF1 intersects NF2. The top part of NF2 is not opened due the stress shadow over it.

6.5 Sequential Hydraulic Fracturing

This section illustrates the modeling of propagation of sequential fractures transverse to the wellbore. The model is able to capture the propagation paths, and the temporal changes in widths and pressures of all fractures. Fracture propagation criterion from section is used to capture the fracture tip propagation paths.

The rock and fluid properties used in this simulation are given in **Table 11**. The initial fractures are considered to be 5 m long. All fractures are allowed to propagate until they reached a length of 20 m when the injection is stopped. The problem is solved for two scenarios.

Table 11 Parameters used to simulate sequential and simultaneous hydraulic fracturing

Parameter	Value	Units
Injection rate (q_0)	20	bpm
Fluid viscosity (μ)	1	cP
Young's modulus (E)	27	GPa
Poisson's ratio (ν)	0.25	
(σ_H), (σ_h)	4.5, 4	MPa
Height	10	m
Normal Stiffness of Proppant (Kn)	20	GPa/m
Shear Stiffness of Proppant (Ks)	20	GPa/m

6.5.1 Case-I

In the first case, once the fracture reaches a desired length, the injection stops and the calculated fluid pressure distribution inside the fracture is averaged and the entire fracture is kept at this average pressure. In this way, the pressurized fracture continuous to exert a stress shadow.

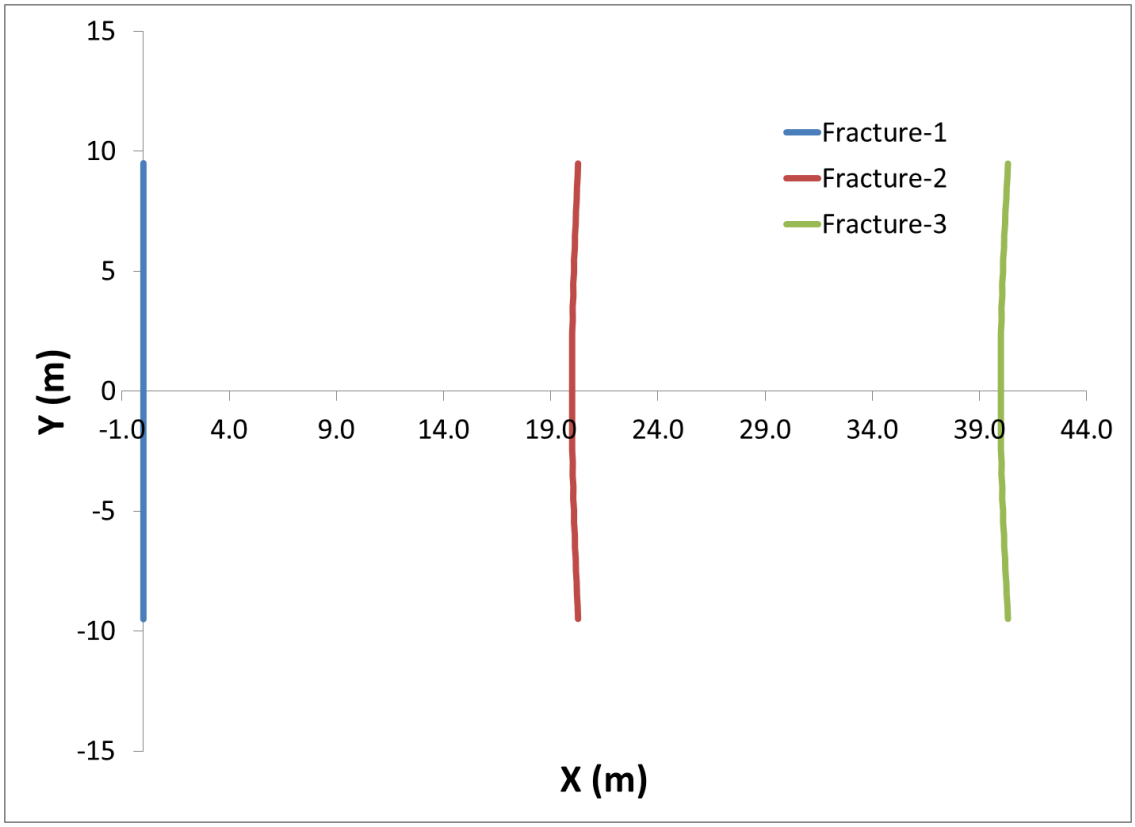

Fig 59. Transverse fractures obtained from sequential injection for Case-I in section 6.5.

Fig. 59 shows the geometry of 3 transverse fractures with 20 m spacing for case I. Fractures 2 and 3 slightly bend away from Fracture 1 due to the stress shadow. But the stress shadow is not strong enough to cause a large deviation.

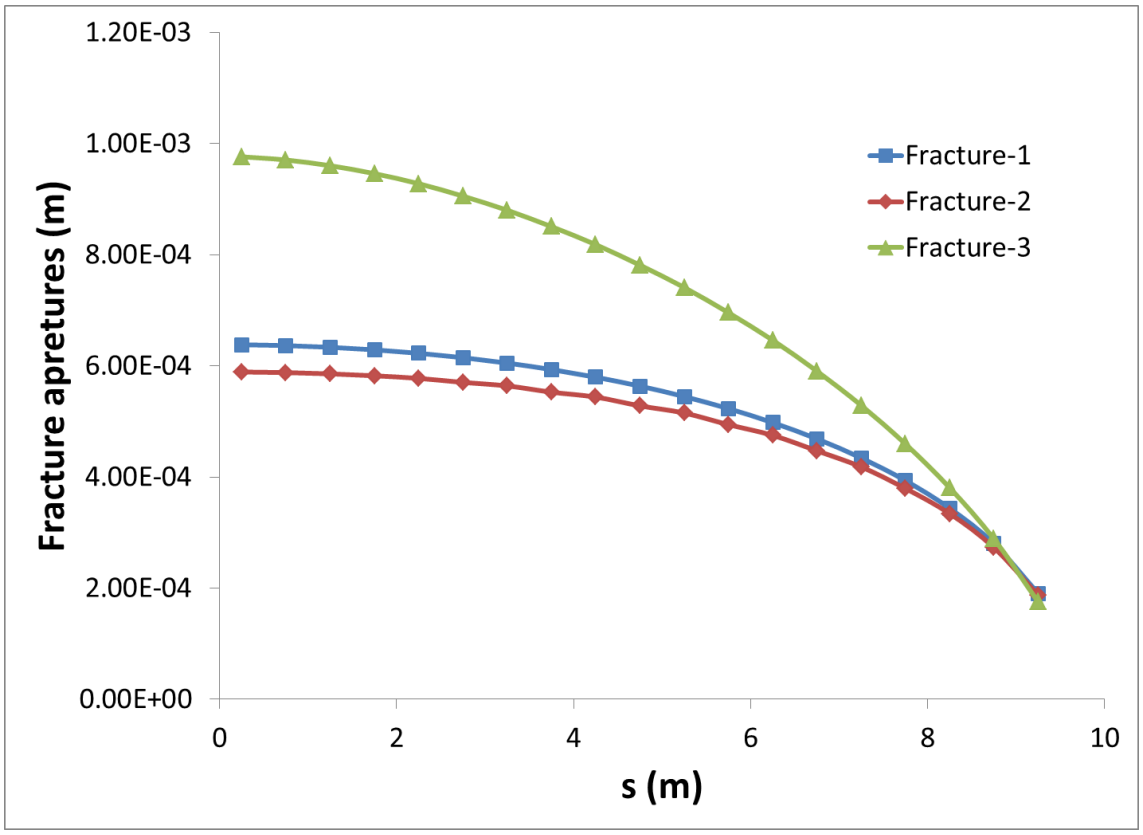

Fig 60. The width profile of all fractures after they reached target length in Case-I. Fracture-2 has the least widths among the three due to high stress shadow over it.

Fig. 60 shows the width profile over a half-length for Fractures 1, 2 and 3 after the third fracture has reached its target length (Case- I). We see that Fracture 3 has the highest width and Fracture 2 has the lowest width (since Fracture 1 and Fracture 3 are exerting stress shadow on Fracture 2).

6.5.2 Case-II

In the second case, it is assumed that once the fracture reaches its target length, the injection stops and the fracture is filled with proppants and is drained (modeling of decreasing in pressure due to leak-off is not included in this study). In this way, we can

study the closure of the fractures over the proppant pack by assigning a stiffness value to the proppant pack. Fig. 61 shows the geometry of fracture network.

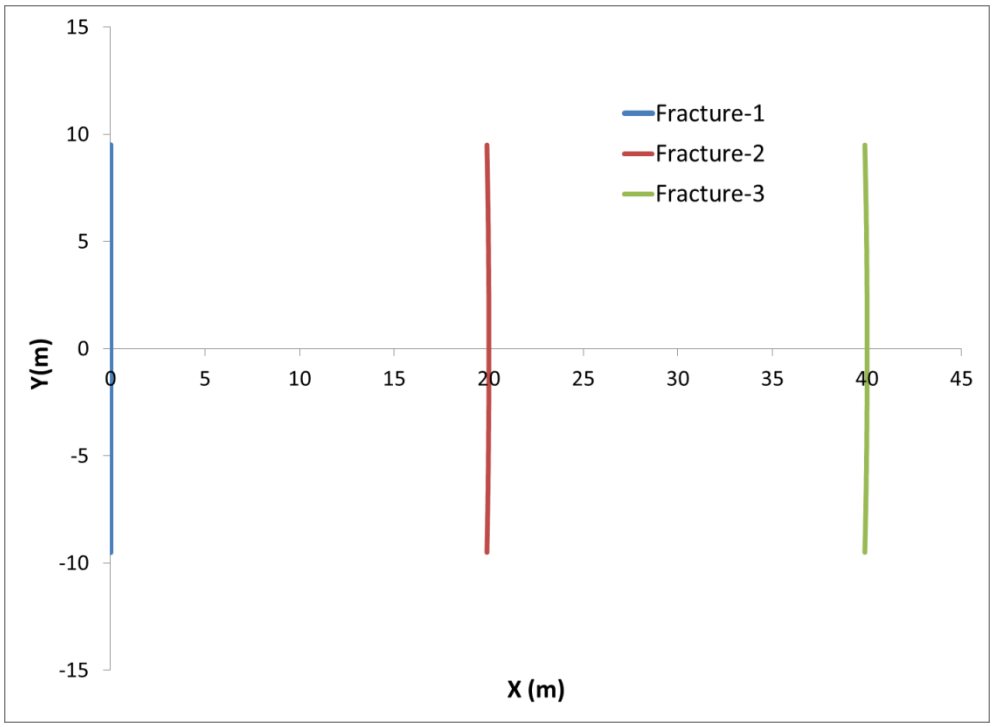

Fig 61. Transverse fractures obtained from sequential injection for Case-II in section 6.5. In this case Fracture 2 and 3 bend slightly towards Fracture 1. This is because the proppant-filled fractures acts a weaker discontinuity and attracts the Fractures 2 and 3.

6.5.3 Comparison of Case-I and Case-II

The same problem (3 fractures with 20 m spacing using properties from **Table 11**) is solved as described in the second case and the results obtained from both cases are compared in Figures 62 and 63.

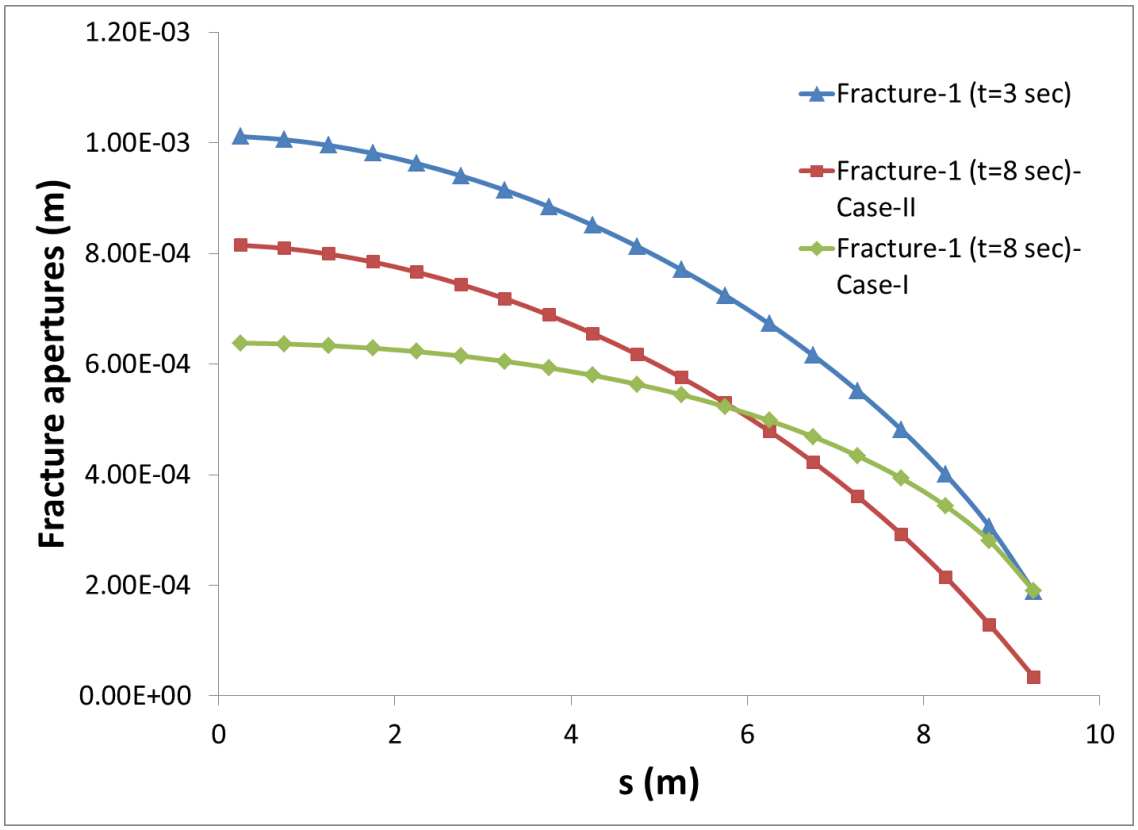

Fig 62. Shows the change in Fracture 1 widths with time from Case-I and Case-II.

Fig. 62 shows the width profile of Fracture 1 at various instants for the two scenarios described above. We can see the width of Fracture 1 decrease with time as other transverse fractures are formed. Note that for Case- I, the width reduction of Fracture 1 is due to the stress shadow exerted by other fractures, whereas in Case- II the width reduction of Fracture 1 is caused by the closure of proppant inside it in response to the in-situ stresses and stress shadow of other fractures.

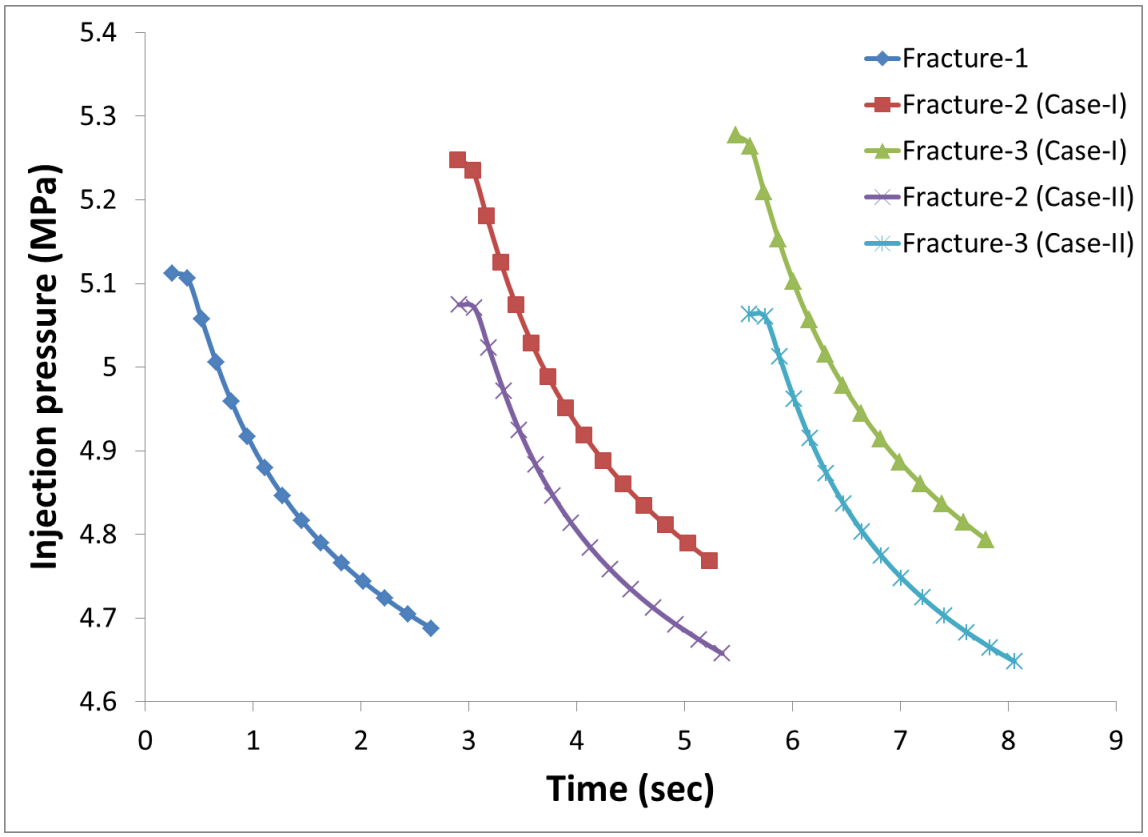

Fig 63. The injection pressure profile for all fractures from Case-I and Case-II.

Fig. 63 shows the injection pressure profile for all 3 fractures obtained from Case- I and Case- II. We can see that the injection pressure is decreasing for all fractures as they propagate. The starting injection pressure for Fracture 2 and Fracture 3 are higher for Case- I because these 2 fractures start in a stress shadow region so they need a higher energy. But from Case- II we observed that the starting injection pressures for Fracture 2 and Fracture 3 is slightly lower. This is because the previous fracture is now proppant filled, behaving like a joint (see section 5.4) and making the rock less stiff. Hence, Fractures 2 and 3 propagate with less pressure.

6.6 Simultaneous Hydraulic Fracturing

This section illustrates the modeling of propagation of transverse fractures while fluid is injected into them simultaneously. All fractures have the same injection rate and initial length (is 5m). **Table 11** shows the input parameters for the simultaneous injection case. The problem is simulated with 10m fracture spacing. The results are shown in Figures 64 and 65.

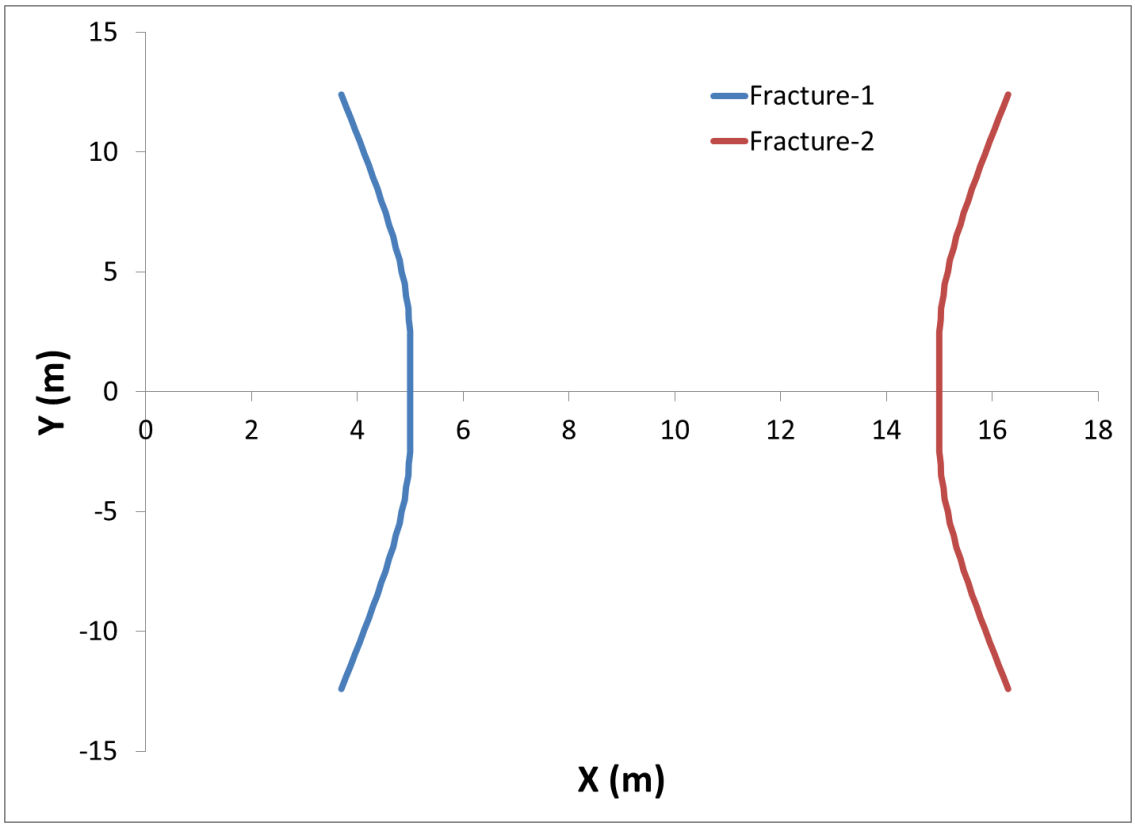

Fig 64. Fracture geometry after 10sec for simultaneous injection of 2 fractures with 10 m spacing.

Fluid is injected into two fractures 10m apart at an injection rate of 20 bpm each. The resultant geometry is shown in Fig. 64. We can observe that due to close spacing of the fractures there is a large stress shadow between the two fractures, which caused them to turn away from each other. Fig. 65 shows the geometry of 3 transverse hydraulic fractures after 12 sec of fluid injection (parameters in **Table 11**).

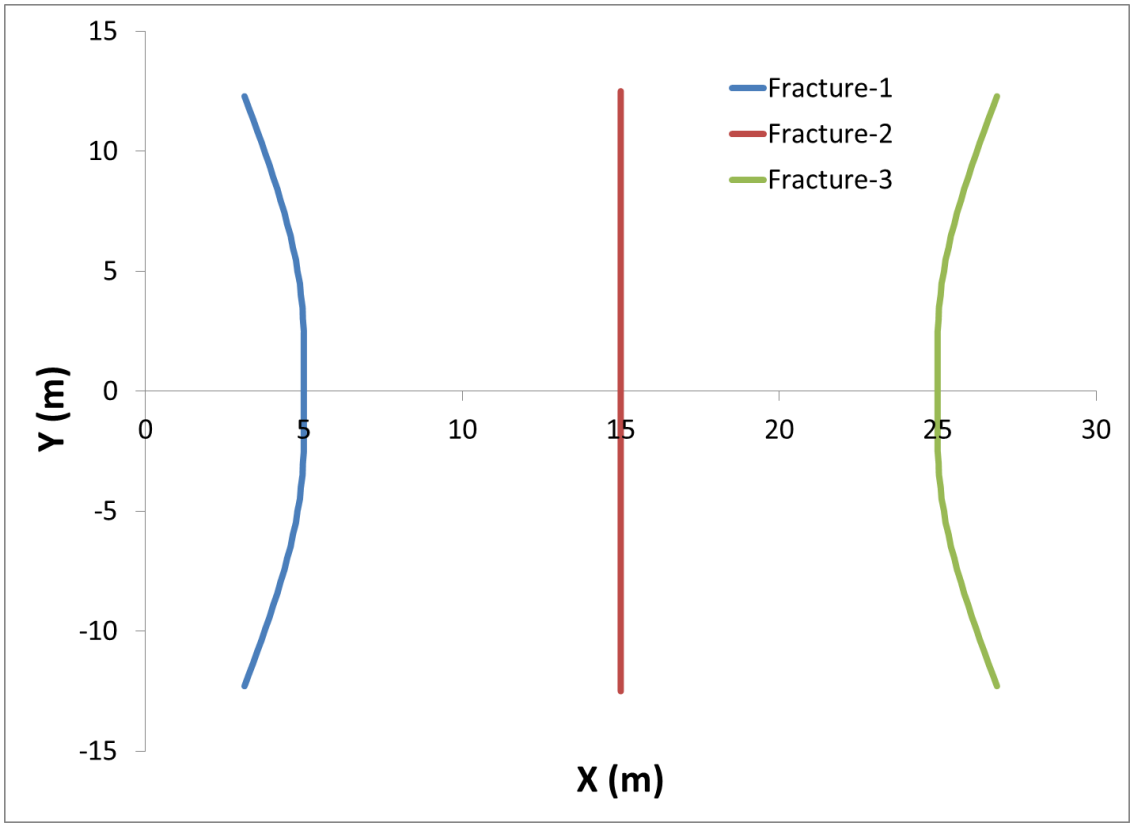

Fig 65. Fracture geometry of 3 fractures with 10m spacing after 12 sec.

From Fig. 65, the outer fracture (Fractures 1 and 3) are deviating away from each other due to stress shadow between them, while the center fracture (i.e., Fracture 2) is moving along its axis due to the symmetric position of Fractures 1 and 3.

As can be seen in Fig. 66, Fracture 2 needs more pressure than Fracture 1 and 3, for it opens against the stress shadow caused by the others. For all three fractures, the injection pressure decreases as they propagate.

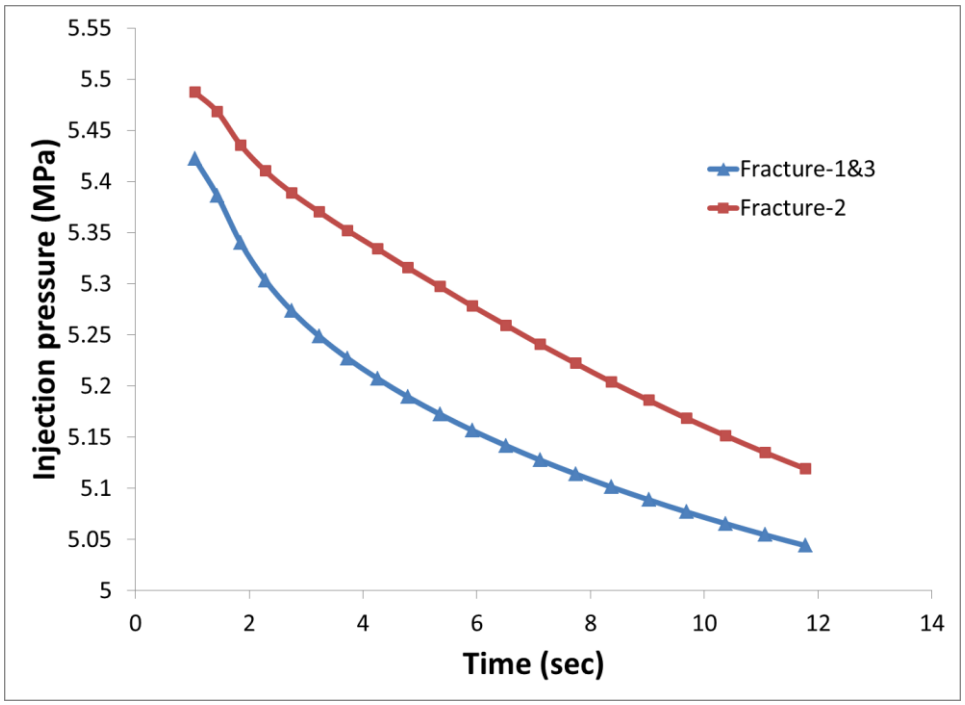

Fig 66. Injection pressure profile obtained for simultaneous propagation of transverse fractures. Fracture 2 needs high pressure to open, because of the stress shadow from Fracture 1 and 3.

Fig. 67 shows the width profile of all fractures (half-length) at various times. We can observe that at a time of 8 sec, widths of Fracture 1 and 3 are slightly higher than that of Fracture 2. This is due to stress shadow acting over Fracture 2. Later at 12 sec, the widths of Fracture 1 and 3 have become slightly less than the Fracture 2 near the fracture center. This might be due to the variation of the stress shadow as Fractures 1 and 3 deviate.

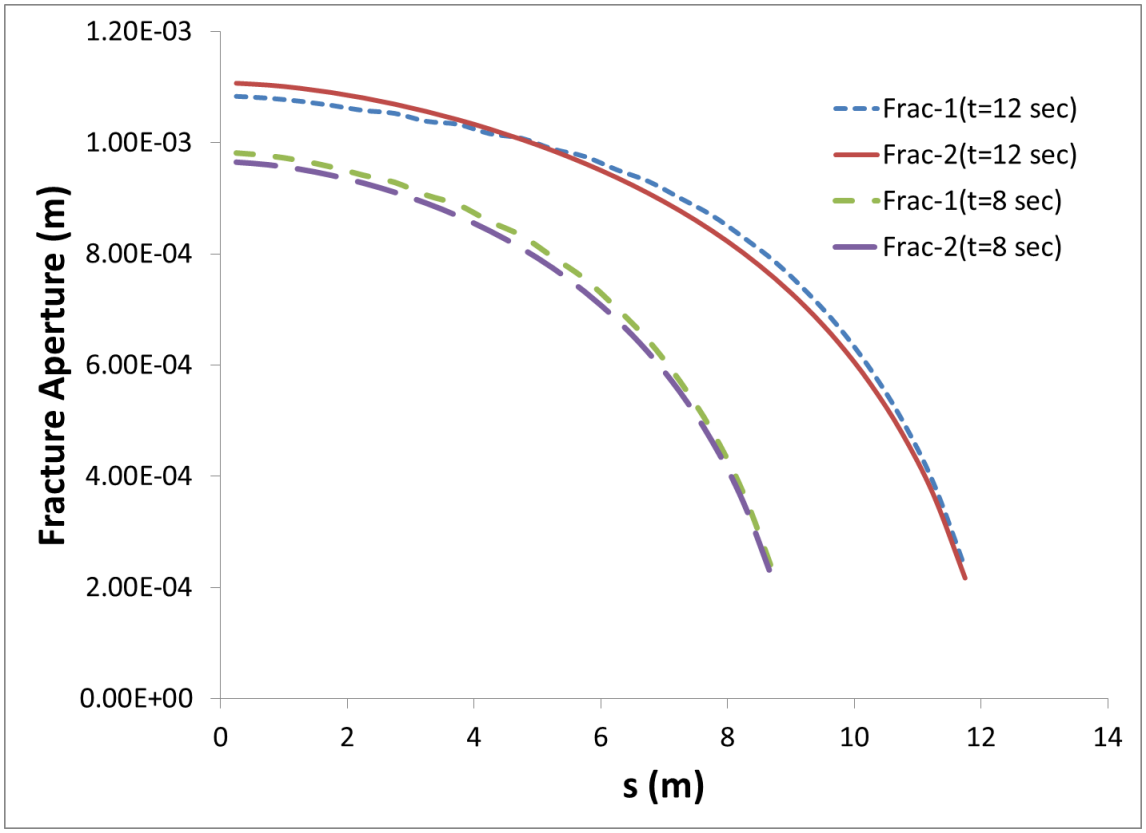

Fig 67. Transverse fractures width profile at various instants from simultaneous injection.

6.7 Fracture Propagation in the Presence of Flaw on Natural Fracture

In this section we consider the cases where there is a flaw located on the natural fracture. As an example the geometry shown in the Fig. 68 is considered. We can see from the Fig. 68 that the flaw is located at a distance of 0.3m from the center of natural fracture. The initial length of the flaw in this case is 0.4m. The other properties used in this simulation are given in **Table 12**. In this simulation after the hydraulic fracture intersect with natural fracture, the tips shown in Fig. 69 are allowed to propagate if their mode I stress intensity factor equals the mode I fracture toughness of the rock $K_I=K_{IC}$. The tip which met this condition first is allowed to propagate first. The pressure required to propagate the fracture is calculated iteratively. Refer to Appendix D for the iterative algorithm.

Table 12 Parameters used to simulate propagation of a flaw on the natural fracture

Parameter	Value	Units
Injection rate (q_0)	0.5	bpm
Fluid viscosity (μ)	1	cP
Young's modulus (E)	27	GPa
Poisson's ratio (ν)	0.25	
(σ_H), (σ_h)	5, 4	MPa
Height	10	m

Table 12 Continued

Parameter	Value	Units
Hydraulic aperture	0.1	mm
Fracture toughness (K_{IC})	2	$MPa.m^{1/2}$

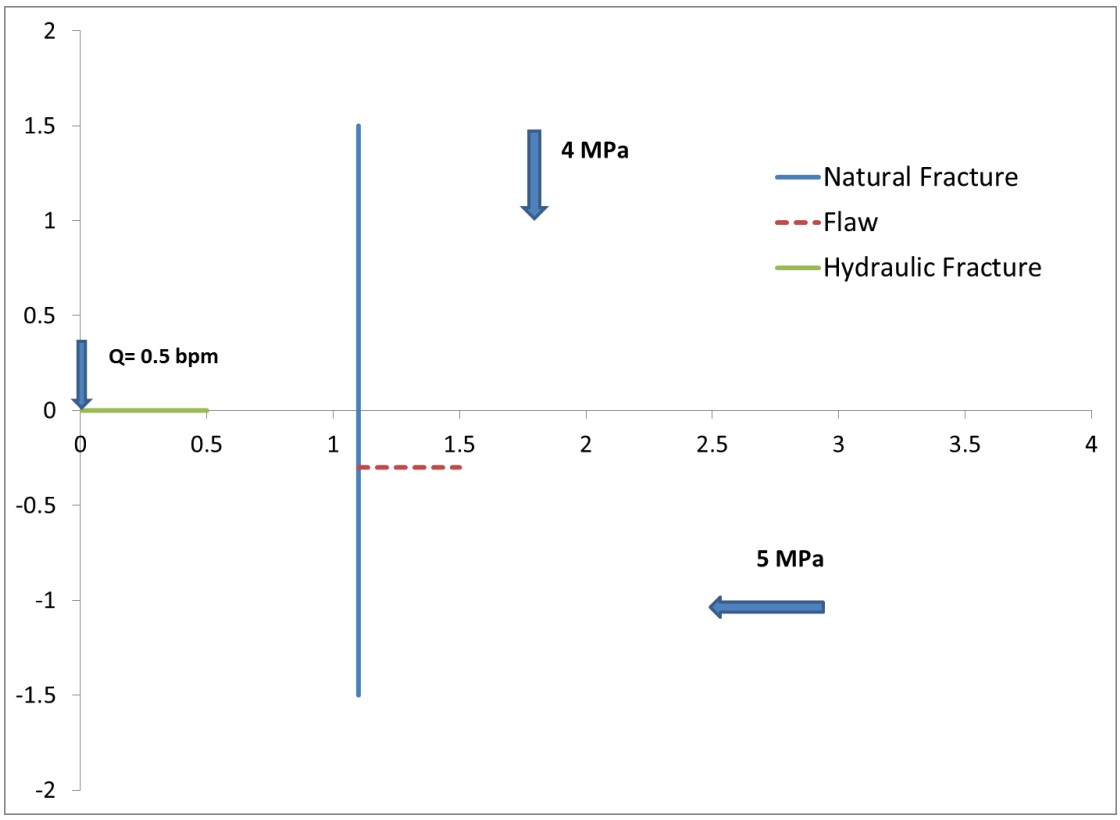

Fig 68. Geometry consisting of flaw (length 0.4m) on the natural fracture at 0.3m from its center.

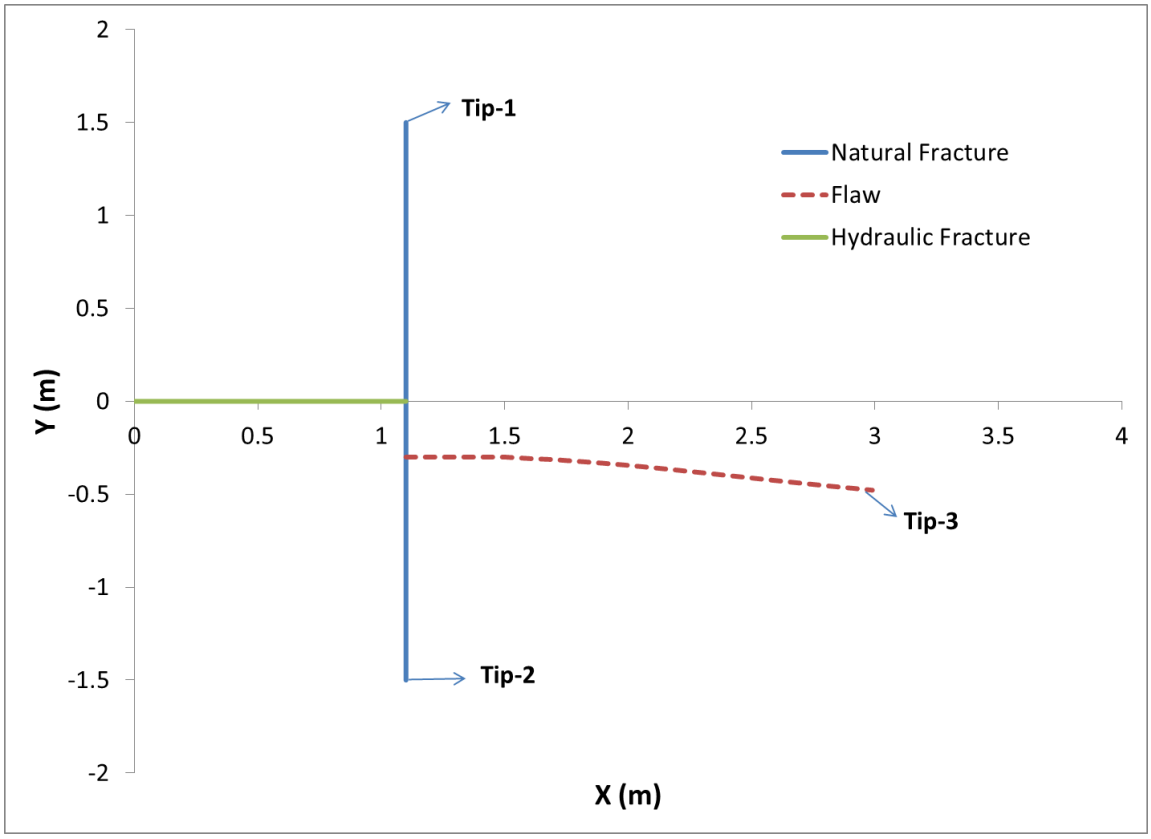

Fig 69. Geometry of the fracture network in Fig 56 after 8 sec.

Fig. 69 shows the geometry of the fracture network in Fig. 69 after 8sec. we can see for the case considered above, the flaw (tip 3) met the fracture propagation condition first and is allowed to propagate. The flaw continued to propagate in the direction of maximum principal stress and slightly bend towards tip 2.

Fig. 70 shows the injection pressure profile for this case. The injection pressures decreased till the hydraulic fracture intersect natural fracture, then after intersection it increased as more pressure is required to open up the natural fracture against the high closure stresses acting on it. The injection pressure continued to increase as the flaw propagated and trying to reach a constant value as the flaw is orienting towards the maximum principal stress.

Fig. 71 shows the pressure profile at flaw tip (tip 3) with time. We can see that the tip pressure is decreasing with time as the flaw propagates. This shows that the pressure needed at the flaw tip to propagate is decreasing as its length increases indicating longer fractures need lower pressure to propagate.

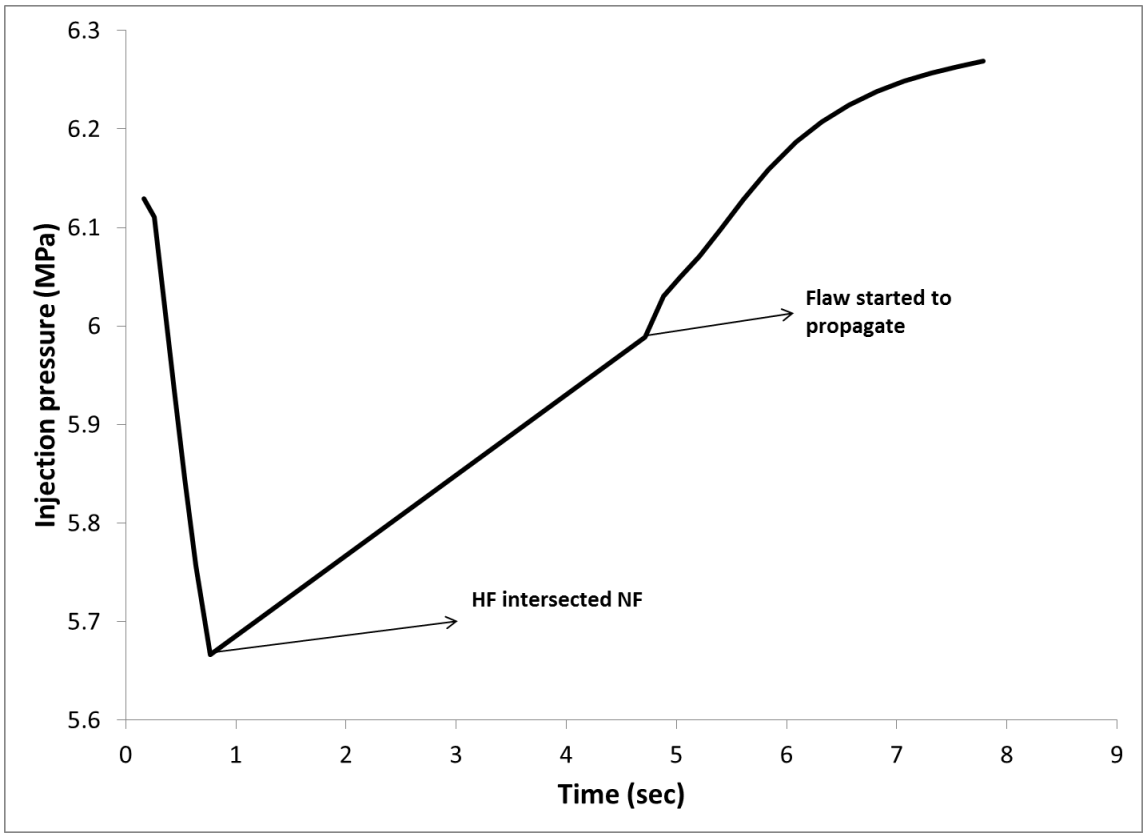

Fig 70. Injection pressure profile obtained for configuration shown in Fig. 68. Injection pressure started to increase after HF intersects NF and continued to increase even after propagation of flaw, finally trying to reach a constant value as the flaw orients towards maximum principal stress.

Fig. 72 shows the width profile for the entire fracture network. For conveniently comparing the widths of the entire fracture network, the fracture widths of all segments are represented under one common axis s. So that s= (0-1m) represents widths along hydraulic fracture, s= (1-4m) represents widths along natural fractures and from s=4m represents widths along the flaw.

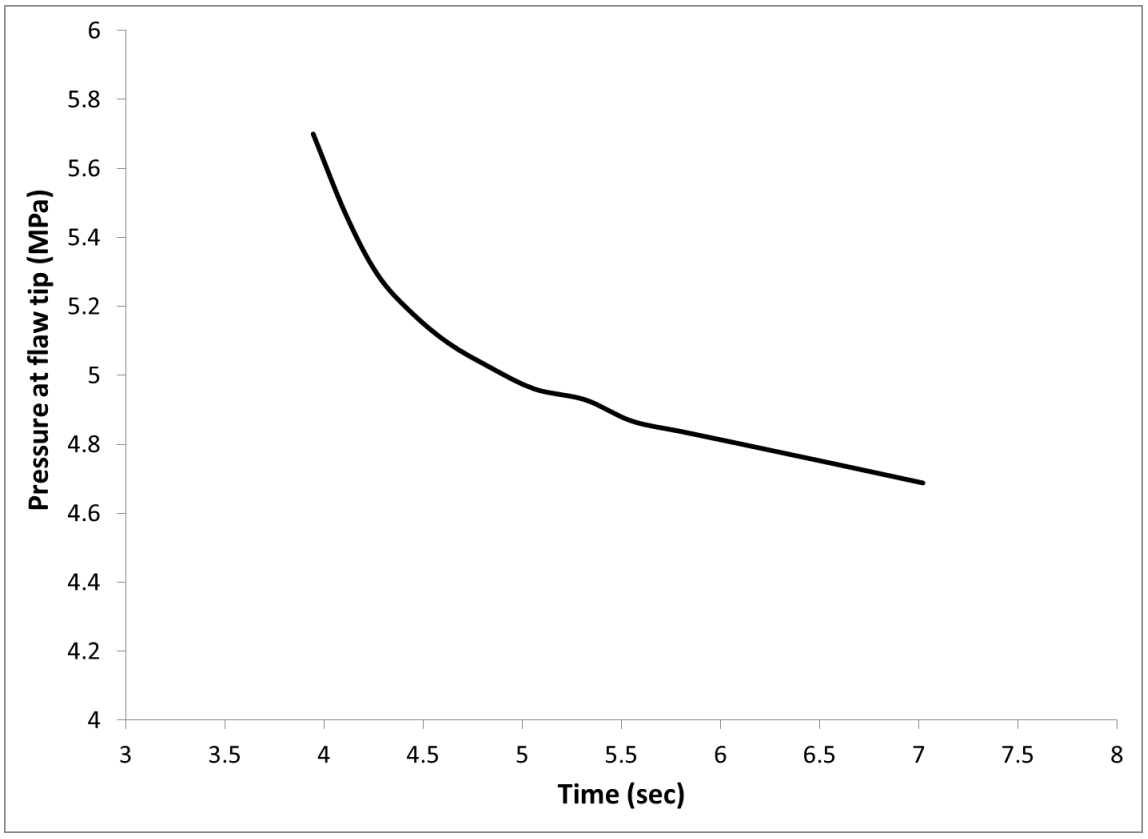

Fig 71. The pressure at flaw tip is decreasing as it propagates, which shows larger crack lengths needs less pressures at their tips to propagate.

We can see from the Fig. 72 that the natural fracture has the least widths of all (as it needs to open up against higher closure stress). At s=3m (i.e. just after the location of flaw on the natural fracture) huge reduction in widths occurred due to stress shadowing between the natural fracture and the flaw.

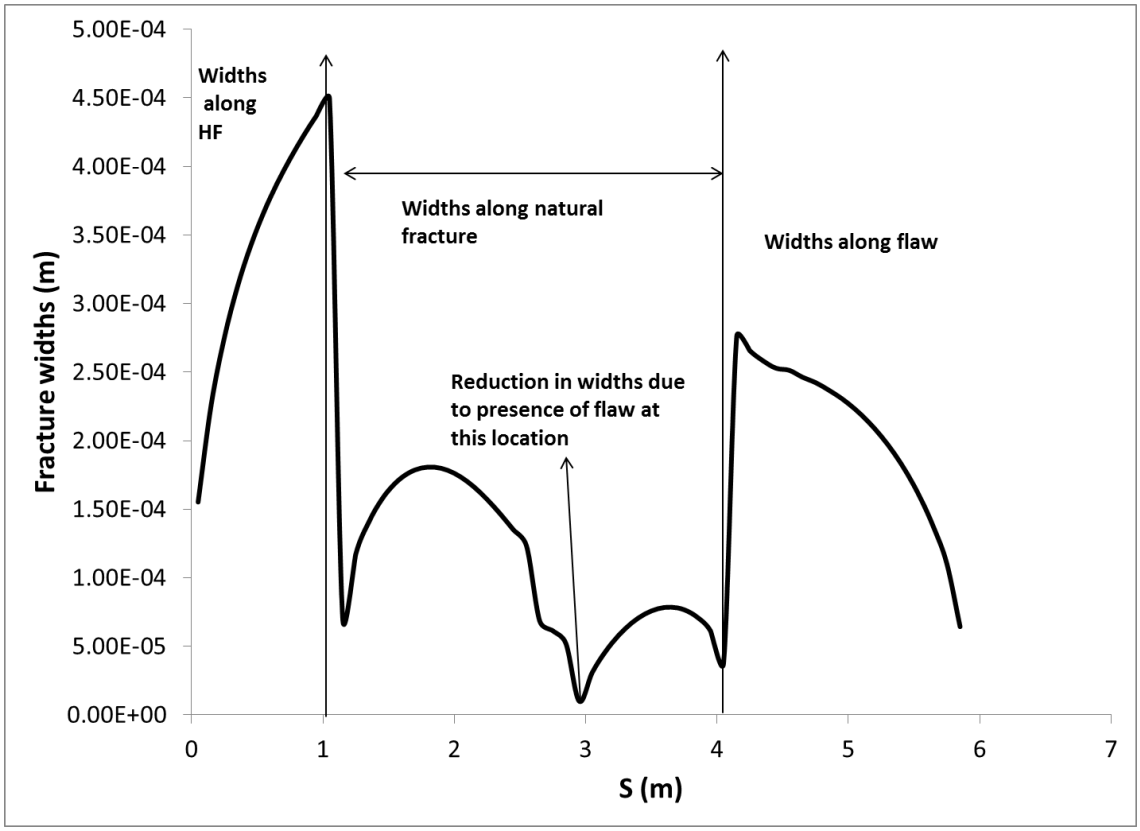

Fig 72. Shows the natural fracture widths at location s=3m (i.e., near the location of flaw) has huge width reduction due to stress shadowing effect.

6.7.1 Effect of flaw Size and location on natural fracture propagation

To study the influence of flaw on the natural fracture propagation after hydraulic fracture intersects natural fracture, the above problem is studied with various flaw sizes and its location on natural fracture. **Table 13** shows the flaw propagation initiation pressures for various lengths of flaw. The location of the flaw is 0.5m from the center of the natural fracture and the remaining properties used in the simulation are shown in **Table 11**. The results from **Table 13** shows that, flaws with smaller initial lengths needs higher pressure to propagate.

Table 13 Results showing the flaw initiation pressures for various flaw lengths

Flaw location=0.5m from the center of natural fracture in the direction of tip 2	
Flaw length in m	Flaw initiation pressure (MPa)
0.3	6.42
0.4	5.68
0.5	5.30

Table 14 Results showing the flaw initiation pressures for various locations of flaw on natural fracture

Flaw length=0.4m	
Flaw location from the center of natural fracture in the direction of tip-2 in m	Flaw initiation pressure (MPa)
0.3	5.72
0.5	5.68
1	5.44

The results from **Table 14** shows the flaw propagation initiation pressure for a flaw length 0.4m located at various locations on the natural fracture. The flaw propagation initiation pressures are increasing for the flaws that are located near to the natural fracture. This is due to the higher pressures at the center of the natural fractures causing huge stress shadowing effect on the flaw, thus it requires very high pressures to open up.

6.7.2 Effect of small flaws on natural fracture propagation

To study the effect of small flaws on the natural fracture propagation, a simulation is carried out by placing a small flaw (0.2m) at various locations on the natural fracture using the parameters in **Table 12**. The results obtained are shown in **Table 15**, it can be seen that if the flaw is too small (in this case 0.2m, tip 3) it will not propagate. The tips of the NF propagate first (Fig. 69). From the data in **Table 15** we can understand that if the flaw is near to tip 2, then tip 3 will propagate first and vice versa. This is because the presence of the flaw near one end of a natural fracture restricts the widths on that section closer to it (see Fig. 72) and thus the other tip will propagate more easily.

Table 15 Shows the ratio K_I/ K_{IC} for all tips at various flaw locations

Location of flaw from the center of NF in the direction of tip-2 in (m)	Size of flaw in (m)	K_I/ K_{IC} Tip-1	K_I/ K_{IC} Tip-2	K_I/ K_{IC} Tip-3
0.3	0.2	1.00	0.99	0.69
0.5	0.2	1.00	0.98	0.7
1	0.2	1.00	0.97	0.8
1.2	0.2	1.00	0.92	0.91

7. SUMMARY AND CONCLUSIONS

7.1 Summary

In this thesis an improvised boundary element based displacement discontinuity method is developed to calculate the stimulated reservoir volume of fracture rock accurately. Special crack tip element and a patch term are added to the existing DD method to calculate the tangential to find the failure potential of the rock much accurately. A fully coupled fluid flow and fracture deformation model has been developed for modeling the interaction between hydraulic and natural fracture. Hydraulic fracture propagation near natural fractures in equilibrium with in-situ stresses and in non-equilibrium with in-situ stresses are modeled. Complex fracture patterns obtained from hydraulic fracture interaction with multiple natural fractures is modeled.

Hydraulic fracture diversion into the inclined natural fractures is also studied. Propagation of natural fracture containing flaws and their interaction with hydraulic fractures is modeled. In addition, sequential and simultaneous injection and propagation of multiple transverse hydraulic fractures is modeled.

7.2 Conclusions

1. The results shows that the tangential stresses calculated on the wall of transverse fractures were underestimated by around 40% at fracture tips when normal DD method is used over the improvised method.

2. The induced shear stresses due to the pressurization of transverse fractures are higher in magnitude at fracture tips, which may cause the rock to fail and induce seismicity.
3. For simulations of hydraulic fracture propagation near natural fractures the results show potentially tortuous hydraulic fracture paths. The sites of facture kinking, intersections, and bends act as chokes and can cause proppant blockages.
4. The injection pressure tends to decrease until the hydraulic fracture intersects the natural fracture. It then increases during the opening and propagation of the natural fracture. This behavior can be seen till the fracture wings completely align with maximum principal stress, then the injection pressure decreases.
5. The magnitude of the injection pressure increase during intersection depends on factors such as injection rate, fluid viscosity, distance between the injection point and natural fracture, the natural fracture stiffness, and the closure stress.
6. After hydraulic fracture intersects an inclined natural fracture, the hydraulic fracture diverts into the natural fracture wing that opens easily and propagates through that end.
7. Simulation results for natural fracture with flaw shows that length and location of a flaw on the natural fracture plays a major role in its opening and propagation. Flaws that are very small in size compared to natural fracture are difficult to open up and propagate, but they still influence the opening of natural fracture and its propagation.

8. Small size flaws on natural fracture needs high pressure to open and to start propagate, as they propagate the pressure needed to keep the propagation decreases.
9. For sequential injection the results show that if the hydraulic fractures are left pressurized, the newer fractures need high injection pressures to start.
10. In the simultaneous injection the center fracture needs a high pressure to open up.
11. The deviation of fractures in the simultaneous injection case is higher than that of sequential injection.
12. In sequential injection a large width reduction occurs in older HFs due to the creation of newer ones, whereas in the simultaneous injection case, this width reduction is small.

NOMENCLATURE

a = Half-length of crack element, m

$A^{ij}_{ss,sn,nn,ns}$ = Boundary influence coefficients for the stresses

D_x = Displacement discontinuity in x-direction, m

DD = Displacement discontinuity

D_y = Displacement discontinuity in y-direction, m

D^i_s = Shear displacement discontinuity at the midpoint of ith element, m

D^i_n = Normal displacement discontinuity at the midpoint of ith element, m

E = Young's modulus, MPa

G = Shear modulus, MPa

hj = Joint filling material thickness, m

HF = Hydraulic Fracture

K_n = Joint normal stiffness, MPa/m

K_s = Joint shear stiffness, MPa/m

K_I = Mode I stress intensity factor, MPa.m$^{1/2}$

K_{IC} = Fracture toughness, MPa.m$^{1/2}$

K_{II} = Mode II stress intensity factor, MPa.m$^{1/2}$

Lh = Fracture half-length, m

NF = Natural fracture

p_f = Pressure inside the fracture, Mpa

Q_0 = Injection rate into hydraulic fracture, bpm

q = Fluid flux, m^2/s

s = Distance along the fracture, m

S_{xx} = Stress in x-direction, MPa

S_{yy} = Stress in y-direction, Mpa

t = Time, sec

T = Distance between injection point and HF-NF intersection point, m

u_x = Displacement in x-direction, m

u_y = Displacement in y-direction, m

w = Fracture width, m

X_s = Total Shear displacement discontinuity of joint, m

X_n = Total normal displacement discontinuity of joint, m

$\mu' = 12\mu$, cP

μ = Dynamic viscosity, cP

$\overset{i}{\sigma}_s$ = Shear stress at the midpoint of ith element, MPa

$\overset{i}{\sigma}_n$ = Normal stress at the midpoint of ith element, MPa

σ_H = Maximum principal stress, MPa

σ_h = Minimum principal stress, MPa

σ_0 = Initial stress, MPa

$\left(\overset{i}{\sigma}_s\right)_0^{\infty}$ = Far-field stresses, MPa

$\left(\overset{i}{\sigma}_s'\right)_0$ = Initial induced stresses, MPa

$\overset{i}{\sigma}_s'$ = Induced stresses, MPa

τ = Shear stress, MPa

β = Slope of shear DD

δ_m = Maximum joint/NF closure, m

δ = Joint/NF closure, m

ξ = Length along the crack tip element, m

Δx = Distance between two elements in finite difference discretization, m

Δt = Time, sec

ω = Relaxation factor in S.O.R method

υ = poisson's ratio

REFERENCES

Batchelor, G.K. 1967. *An Introduction to Fluid Dynamics*. Cambridge, UK: Cambridge University Press, Original edition, ISBN 0521 663962.

Blanton, T.L. 1982. An Experimental Study of Interaction Between Hydraulically Induced and Pre-Existing Fractures. SPE Unconventional Gas Recovery Symposium, Pittsburgh, Pennsylvania, SPE of AIME.

Cooke, M.L. and Underwood, C.A. 2001. Fracture Termination and step-over at Bedding Interfaces due to Frictional slip and Interface opening. *Journal of Structural Geology* 23**,** 223-238.

Crouch, S.L. and Starfield, A.M. 1983. *Boundary Element Methods in Solid Mechanics*: With Applications in Rock Mechanics and Geological Engineering. London: George Allen & Unwin.

Cheng, Y. 2009. Boundary Element Analysis of the Stress Distribution around Multiple Fractures: Implications for the Spacing of Perforation Clusters of Hydraulically Fractured Horizontal Wells. Paper SPE 125769 presented at the Eastern Regional Meeting, Charleston, West Virginia, USA, 23-25 September.

Dobroskok, A. and Ghassemi, A. 2004. Crack Propagation, Coalescence and Re-initiation in Naturally Fractured Rocks. In GRC Trans, 28, 285-288.

Dobroskok, A., Ghassemi, A. and Linkov, A. 2005. Extended Structural Criterion for Numerical Simulation of Crack Propagation and Coalescence under Compressive Loads. *International Journal of Fracture*, 133, 223-246.

Fu, P., Johnson, S.M., Hao, Y. and Carrigan, C. R. 2011. Fully Coupled Geomechanics and Discrete Flow Network Modeling of Hydraulic Fracturing for Geothermal Applications. Thirty-Sixth Workshop on Geothermal Reservoir Engineering, Stanford University, Stanford, California, January 31 - February 2.

Ge, J., and Ghassemi, A. 2007. Pore pressure and stress distributions around an injection-induced fracture. Geothermal Resources Council Transaction.

Koshelev, V. and Ghassemi, A. 2003a. Numerical Modeling of Stress Distribution and Crack Trajectory near a Fault or a Natural Fracture. Soil-Rock America Symp. Boston.

Koshelev, V. and Ghassemi, A. 2003b. Hydraulic Fracture Propagation near a Natural Discontinuity. Twenty-Eight Workshop on Geothermal Reservoir Engineering, Stanford University, Stanford, California.

Lawrence, C. Murdoch and Leonid, N. Germanovich 2006. Analysis of a Deformable Fracture in permeable Material. *International Journal for Numerical and Analytical Methods in Geomechanics,* 30, 529-561.

Nordgren, R.P. 1972. Propagation of a Vertical Hydraulic Fracture. *Society of Petroleum Engineers Journal*, 12, 306-314.

Potluri, N.K., Zhu, D. 2005. The Effect of Natural Fractures on Hydraulic Fracture Propagation. SPE European Formation Damage Conference, Sheveningen, The Netherlands, SPE.

Renshaw, C.E. and Pollard, D.D 1995. An Experimentally Verified Criterion for Propagation across Unbounded Frictional Interfaces in Brittle, Linear Elastic Materials. *International Journal of Rock Mechanics and Mining Science & Geomechanics Abstracts,* 32(3), 237-249.

Stone, T.J. and Babuska, I. 1998. A numerical method with a posteriori error estimation for determining the path taken by a propagating crack. *Computer methods in applied mechanics and engineering*, 160, 245-271.

Thiercelin, M.J. and Makkhyu, E. 2007. Stress Field in the Vicinity of a Natural Fault Activated by the Propagation of an Induced Hydraulic Fracture. U.S. Rock Mechanics Symposium, Vancouver, B.C., Canada, 27-31 May.

Vijayakumar, S., John, H.C. and Reginald, H. 2007. On the Tangential Stress Anomaly in the Displacement Discontinuity Method. *Mechanics Research Communications*, 35(4), 237-245.

Warpinski, N.R. and Teufel, L.W. 1987. Influence of Geologic Discontinuities on Hydraulic Fracture Propagation. *SPE Journal of Petroleum Technology,* 39(2), 209-220.

Warpinski, N.R. and Wolhart, S.L. 2004. Analysis and Prediction of Microseismicity Induced by Hydraulic Fracturin. *SPE Journa of Petroleum Technology,* 9(1), 24-33.

Weng, X., Kresse, O., Cohen, C., Wu, R. and Gu, H., Schlumberger 2011. Modeling of Hydraulic Fracture Network Propagation in a Naturally Fractured Formation. SPE 140253, SPE Hydraulic Fracturing Technology Conference and Exhibition, Woodlands, Texas, USA, 24–26 January.

Wenxu, X. 2010. Numerical Inverstigation of Interaction Between Hydraulic Fractures and Natural Fractures. M.S. thesis, Texas A&M University, College Station, Texas.

Wu, H. and Chudnovsky, A. 2004. A Map Of Fracture Behavior In The Vicinity Of An Interface. Gulf Rocks 2004, the 6th North America Rock Mechanics Symposium (NARMS), Houston, Texas, ARMA.

Yan, X. 2004. A Special Crack Tip Displacement Discontinuity Element. *Mechanics Research Communications*, 31(6), 651-659.

Zhang, X. and Jeffrey R.G. 200. The Role of Friction and Secondary Flaws on Deflection and Re-initiation of Hydraulic Fractures at Orthogonal Pre-Existing Fractures. *Geophysical Journal International,* 166, 1454-1465.

APPENDIX A

A.1 Normal DD element vs. special crack tip element

A.1.1 Crack tip element formulation

Based on the above arguments the special crack tip element is designed. (Fig. 73) The special crack tip element in which u_y the relative normal displacement between the crack surfaces is given by

$$u_y = D_y(\frac{\xi}{a})^{1/2}$$
$$u_x = D_x(\frac{\xi}{a})^{1/2} \quad (23)$$

where 2a is the length of the crack tip element D_y is the displacement discontinuity at the center of this element.

If we consider the arbitrary displacement discontinuity distributions along element length 2a as

$$D_x = D_x(\xi)$$
$$D_y = D_y(\xi) \quad (24)$$

Based on the solution of constant displacement discontinuity given by (S.L.Crouch & A.M.Starfield, 1983) the displacement and stresses at domain point (x, y) due to the differential element (2de) displacement discontinuity can be obtained in differential form as

$$du_x = D_x(\xi)[2(1-\nu)T_3(x,y,\xi,d\xi) - yT_5(x,y,\xi,d\xi)] + D_y(\xi)[-(1-2\nu)T_2(x,y,\xi,d\xi) - yT_4(x,y,\xi,d\xi)]$$

$$du_y = D_x(\xi)[(1-2\nu)T_2(x,y,\xi,d\xi) - yT_4(x,y,\xi,d\xi)] + D_y(\xi)[2(1-\nu)T_3(x,y,\xi,d\xi) - yT_5(x,y,\xi,d\xi)]$$

$$d\sigma_{xx} = 2GD_x(\xi)[2T_4(x,y,\xi,d\xi) + yT_6(x,y,\xi,d\xi)] + 2GD_y(\xi)[-T_5(x,y,\xi,d\xi) + yT_7(x,y,\xi,d\xi)]$$

$$d\sigma_{yy} = 2GD_x(\xi)[-yT_6(x,y,\xi,d\xi)] + 2GD_y(\xi)[-T_5(x,y,\xi,d\xi) - yT_7(x,y,\xi,d\xi)]$$

$$d\sigma_{xy} = 2GD_x(\xi)[-T_5(x,y,\xi,d\xi) + yT_7(x,y,\xi,d\xi)] + 2GD_y(\xi)[-yT_6(x,y,\xi,d\xi)]$$

(25)

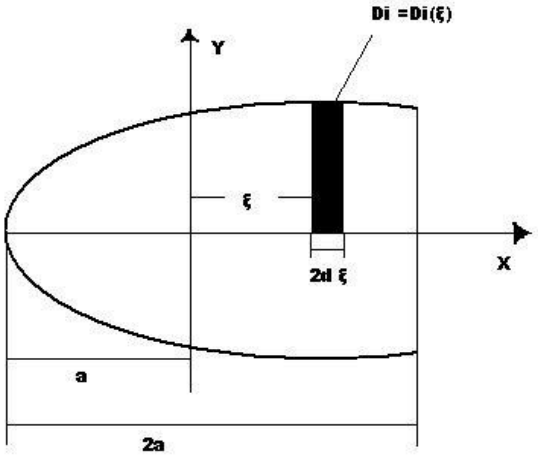

Fig 73. Schematic of the Displacement discontinuity at the left crack tip.

$$
\begin{aligned}
T_2(x,y,\xi,d\xi)/d\xi &= \frac{-1}{4\pi(1-\nu)}\frac{x-\xi}{(x-\xi)^2+y^2} \\
T_3(x,y,\xi,d\xi)/d\xi &= \frac{-1}{4\pi(1-\nu)}\frac{y}{(x-\xi)^2+y^2} \\
T_4(x,y,\xi,d\xi)/d\xi &= \frac{2y}{4\pi(1-\nu)}\frac{x-\xi}{\{(x-\xi)^2+y^2\}^2} \\
T_5(x,y,\xi,d\xi)/d\xi &= \frac{1}{4\pi(1-\nu)}\frac{(x-\xi)^2-y^2}{\{(x-\xi)^2+y^2\}^2} \\
T_6(x,y,\xi,d\xi)/d\xi &= \frac{2}{4\pi(1-\nu)}\{\frac{(x-\xi)^3}{\{(x-\xi)^2+y^2\}^3}-\frac{3(x-\xi)y^2}{\{(x-\xi)^2+y^2\}^3}\} \\
T_7(x,y,\xi,d\xi)/d\xi &= \frac{2y}{4\pi(1-\nu)}\{\frac{3(x-\xi)^2}{\{(x-\xi)^2+y^2\}^3}-\frac{y^2}{\{(x-\xi)^2+y^2\}^3}\}
\end{aligned}
\tag{26}
$$

Since the displacement discontinuity functions chosen are

$$
\begin{aligned}
D_x(\xi) &= D_x\left(\frac{\xi}{a}\right)^{1/2} \\
D_y(\xi) &= D_y\left(\frac{\xi}{a}\right)^{1/2}
\end{aligned}
\tag{27}
$$

where D_x and D_y are the displacement discontinuities at the center of the element. Substituting the displacement discontinuity functions in the above given differential form of stresses and displacements we obtain the integrals to be solved in the form given below

$$
D_j\int_0^{2a}\left(\frac{\xi}{a}\right)^{1/2}T_i(x,y,\xi)d\xi = D_jB_i(x,y),(i=2,...7;\ j=x,y) \tag{28}
$$

The solutions for the above formulation 27 are given in Yan (2004).

After calculating normal and shear displacements from using crack tip elements, the stress intensity factors at fracture tip can be calculated using the following equations

$$K_I = -\frac{\sqrt{2\pi}GD_n}{4(1-\upsilon)\sqrt{a}} \tag{29}$$

$$K_{II} = -\frac{\sqrt{2\pi}GD_s}{4(1-\upsilon)\sqrt{a}} \tag{30}$$

For the boundary stress conditions, Fracture properties and rock properties given in the **Table 2**, the values obtained for using the ordinary elements and special crack tip elements are tabulated below and compared. **Tables 16& 17** show the comparison of normal displacement discontinuity D_n at the center of the element for ordinary and crack tip elements. As discussed above in section the ordinary elements are overestimated the D_n at crack tips, which can be observed from the table that the D_n for ordinary elements is much higher than that obtained for crack tip elements. This difference in D_n is not constant and changing with the number of the elements taken (i.e., the element length). For less number of elements taken the more difference is observed between the values of D_n. The difference between D_n for ordinary and crack tip elements is decreasing with increase in number of elements (deceasing element length). This is because the influence of crack tip is lessening with increasing the number of elements thus adding no significance of crack tip elements to the solution. Hence the accuracy of crack tip element program is improved by choosing much more complex element, but not by increasing the number of elements.

Table 16 Displacement discontinuity $U_y(a)$ at the center x=a of crack tip and the next consecutive element for center crack

Number of elements **N**	Element length(ft) **2a**	Element	$U_y(a)=D(N)$	
			Ordinary elements	Crack tip elements
50	2	Tip element	-2.15E-03	-1.89E-03
		Next element	-2.85E-03	-2.84E-03
100	1	Tip element	-1.59E-03	-1.38E-03
		Next element	-2.24E-03	-2.23E-03
150	0.6667	Tip element	-1.31E-03	-1.14E-03
		Next element	-1.90E-03	-1.88E-03
200	0.5	Tip element	-1.15E-03	-0.991E-03
		Next element	-1.67E-03	-1.65E-03
300	0.3333	Tip element	-0.944E-03	-0.814E-03
		Next element	-1.39E-03	-1.37E-03

For the boundary conditions and fracture properties given in **Table 2**, dividing the fracture into 100 elements, the values obtained for S_{xx} and S_{yy} along the line of center and top fractures are tabulated below. We can see at points very near to fracture tips more accurate values of S_{xx} and S_{yy} are obtained. A difference of 150 psi is observed between the values of S_{xx} and S_{yy} for top crack (**Tables 18& 19**). The difference will increase with decreasing the number of elements, but less number of elements may not give the accurate answer, hence a moderate number of elements should be taken.

Table 17 Displacement discontinuity $U_y(a)$ at the center x=a of crack tip and the next consecutive element for top crack

Number of elements **N**	Element length(ft) **2a**		$U_y(a)=D(N)$	
			Ordinary elements	Crack tip elements
50	2	Tip element	-3.51E-03	-3.03E-03
		Next element	-5.09E-03	-5.03E-03
100	1	Tip element	-2.50E-03	-2.16E-03
		Next element	-3.69E-03	-3.65E-03
150	0.6667	Tip element	-2.05E-03	-1.77E-03
		Next element	-3.04E-03	-3.00E-03
200	0.5	Tip element	-1.78E-03	-1.54E-03
		Next element	-2.65E-03	-2.61E-03
300	0.3333	Tip element	-1.45E-03	-1.26E-03
		Next element	-2.17E-03	-2.14E-03

Table 18 Comparison of the values of S_{xx} and S_{yy} near the center fracture tip in Fig. 7 which are obtained from using ordinary and crack tip elements

	S_{xx}(psi)		S_{yy}(psi)	
Distance from crack tip	Ordinary elements	Special elements	Ordinary elements	Special elements
101	-5232.00	-5299.00	-2975.00	-3036.00
102	-5675.00	-5700.00	-3375.00	-3395.00

Table 18 Continued

	S_{xx}(psi)		S_{yy}(psi)	
Distance from crack tip	Ordinary elements	Special elements	Ordinary elements	Special elements
103	-5834.00	-5846.00	-3494.00	-3503.00
104	-5916.00	-5924.00	-3543.00	-3548.00
105	-5967.00	-5972.00	-3566.00	-3569.00

Table 19 Comparison of the values of S_{xx} and S_{yy} near the Top fracture tip in Fig. 7 which are obtained from using ordinary and crack tip elements

	S_{xx}(psi)		S_{yy}(psi)	
Distance from crack tip	Ordinary elements	Special elements	Ordinary elements	Special elements
101	-4313.00	-4443.00	-2285.00	-2411.00
102	-5065.00	-5117.00	-3017.00	-3065.00
103	-5343.00	-5373.00	-3276.00	-3303.00
104	-5495.00	-5514.00	-3410.00	-3427.00
105	-5593.00	-5607.00	-3493.00	-3504.00

APPENDIX B

This section shows the discretization of fluid flow (Eq. 11) for a uniform 1D grid.

The fluid flux q is given by poiseuille as:

$$q = -\frac{w^3}{\mu'}\frac{\partial p}{\partial x} \tag{31}$$

The continuity equation is

$$\frac{\partial w}{\partial t} + \frac{\partial q}{\partial x} = 0 \tag{32}$$

Substituting Eq. 31 in Eq. 32 we get

$$\frac{\partial w}{\partial t} = \frac{\partial}{\partial x}\left(\frac{w^3}{\mu'}\frac{\partial p}{\partial x}\right) \tag{33}$$

$$\frac{\partial}{\partial x}\left(\frac{w^3}{\mu'}\frac{\partial p}{\partial x}\right)_i = \frac{1}{\mu'}\frac{{w^3}_{i+1/2}\frac{(p_{i+1}-p_i)}{\Delta x} - {w^3}_{i-1/2}\frac{(p_i-p_{i-1})}{\Delta x}}{\Delta x} \tag{34}$$

$$w^3_{i\pm 1/2} = \left(\frac{w_i + w_{i\pm 1}}{2}\right)^3 \tag{35}$$

Substituting Eq. 35 in Eq. 34

$$\frac{\partial w}{\partial t} = \frac{1}{\mu'}\frac{\left(\frac{w_i + w_{i+1}}{2}\right)^3\frac{(p_{i+1}-p_i)}{\Delta x} - \left(\frac{w_i + w_{i-1}}{2}\right)^3\frac{(p_i-p_{i-1})}{\Delta x}}{\Delta x} \tag{36}$$

$$\frac{\partial w}{\partial t} = \frac{1}{\mu'} \frac{\left(w_i + w_{i+1}\right)^3 (p_{i+1} - p_i) - \left(w_i + w_{i-1}\right)^3 (p_i - p_{i-1})}{8\Delta x^2} \tag{37}$$

$$\frac{w_i^{m+1} - w_i^m}{\Delta t} = \frac{1}{\mu'} \frac{\left(w_i + w_{i+1}\right)^3 (p_{i+1} - p_i) - \left(w_i + w_{i-1}\right)^3 (p_i - p_{i-1})}{8\Delta x^2} \tag{38}$$

$$w_i^{m+1} - w_i^m = \frac{\Delta t 8\Delta x^2}{\mu'} \left(w_i + w_{i+1}\right)^3 (p_{i+1} - p_i) - \left(w_i + w_{i-1}\right)^3 (p_i - p_{i-1}) \tag{39}$$

$$\text{Assuming } T_{i\pm1/2} = \frac{\Delta t 8\Delta x^2}{\mu'} \left(w_i + w_{i\pm1}\right)^3 \tag{40}$$

$$w_i^{m+1} - w_i^m = p_{i-1}(T_{i-1/2}) - p_i(T_{i-1/2} + T_{i+1/2}) + p_{i+1}(T_{i+1/2}) \tag{41}$$

The above Eq. 41 gives a set of N linear equation for i=1, N, which can be solved simultaneously for pressures.

APPENDIX C

Flow chart showing fluid flow and fracture deformation coupling:

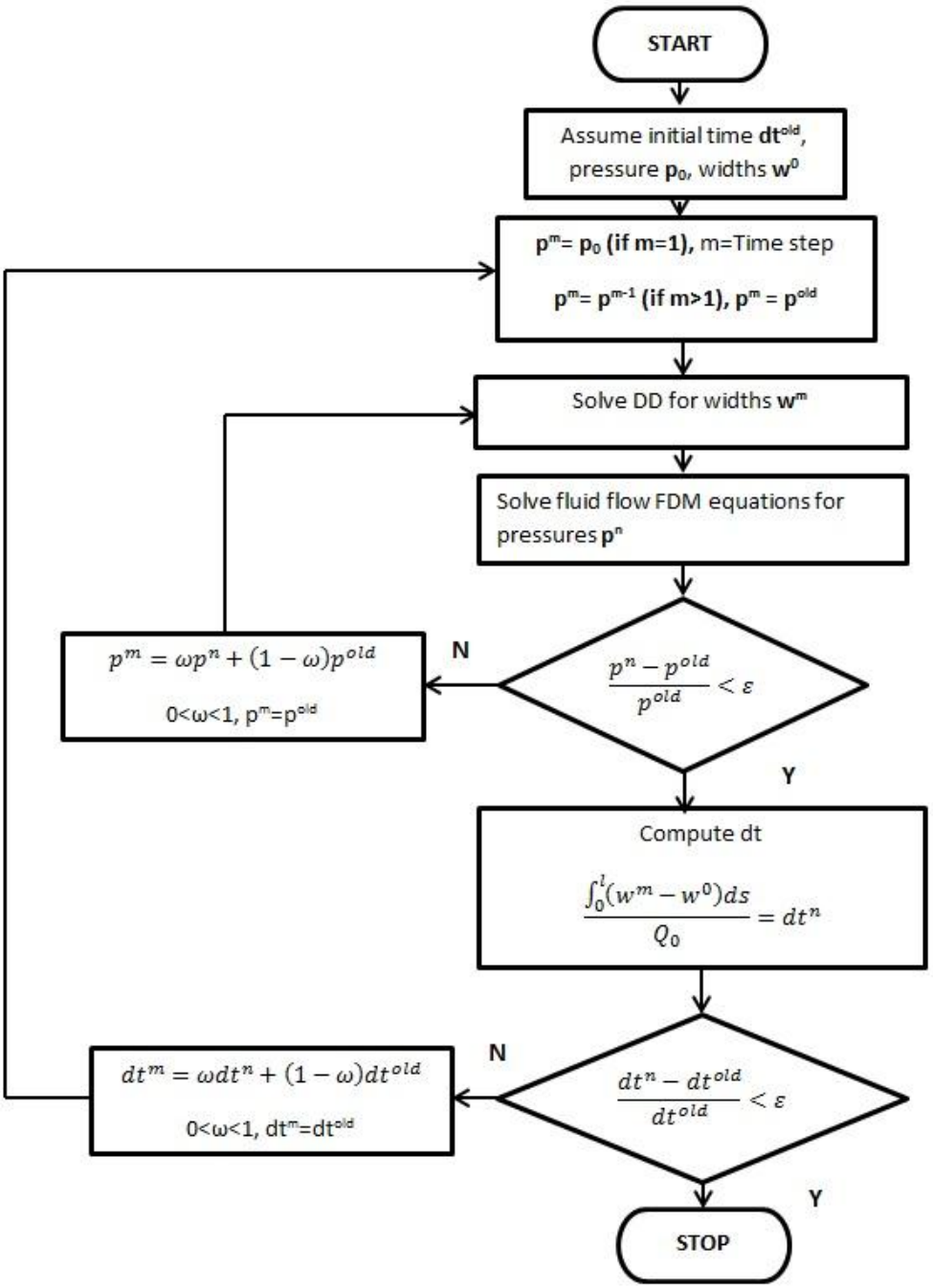

APPENDIX D

Algorithm to find the fracture pressure required for propagation on condition $K_I=K_{IC}$ Lawrence (2006). This algorithm is used to solve for pressure at the fracture tips in section 6.7.

1. Assume a pressure at fracture tip, p1= p_{tip}

2. Calculate K_{I1} using Eq. 29 for tip pressure p1

3. Calculate K_{I2} for tip pressure p2=0.95 *p1

4. Calculate K_{Im} for tip pressure pm, where $pm = p1 + (p2 - p1)\left(\frac{K_{Ic} - K_{I2}}{K_{I2} - K_{I1}}\right)$

5. Calculate error for K_{Im} and K_{Ic}

6. If error is less than tolerance specified then exit, else go to step 7

7. Calculate K_{Im} using p1=p2, p2=pm , $pm = p2 + (p2 - p1)\left(\frac{K_{Ic} - K_{I2}}{K_{I2} - K_{I1}}\right)$

8. Repeat step 7 if necessary until K_{Im} is converged with K_{Ic}

VITA

Name:	Varahanaresh Kumar Sesetty
Address:	Harold Vance Department of Petroleum Engineering, 3116 TAMU, College Station, TX 77843-3116
Email Address:	varahanaresh.sesetty@gmail.com
Education:	B.Tech., Mechanical Engineering, MVGR College of Engg (JNTU)., 2009 M.S., Petroleum Engineering, Texas A&M University, 2012 College Station, Texas